Title
Optomechanical Dynamics in Vertical-Cavity Surface-Emitting Lasers

Author
Gerke, Stephen Adair

Publication Date
2017

Peer reviewed|Thesis/dissertation

Optomechanical Dynamics in Vertical-Cavity Surface-Emitting Lasers

By

Stephen Adair Gerke

A dissertation submitted in partial satisfaction of the

requirements for the degree of

Doctor of Philosophy

in

Engineering – Electrical Engineering and Computer Sciences

in the

Graduate Division

of the

University of California, Berkeley

Committee in charge:

Professor Connie J. Chang-Hasnain, Chair
Professor Eli Yablonovich
Professor Liwei Lin

Summer 2017

Optomechanical Dynamics in Vertical-Cavity Surface-Emitting Lasers

Abstract

Optomechanical Dynamics in Vertical-Cavity Surface-Emitting Lasers

by

Stephen Adair Gerke

Doctor of Philosophy in Electrical Engineering and Computer Sciences

University of California, Berkeley

Professor Connie J. Chang-Hasnain, Chair

Vertical-cavity surface-emitting lasers (VCSELs) have emerged as one of the most numerous and diverse categories of semiconductor laser, serving applications in telecommunications, imaging, ranging, and sensing. Improving the behavior of these devices, while extending them into new application spaces, is currently one of the most active fields of optoelectronics research. Concurrently, improvements in micro-optics, micro-mechanics, and low-noise experimentation have produced a field of cavity optomechanics studying the forces of confined light to excite or cool mechanical systems. This thesis explores the interaction of those fields by observing optomechanical forces acting on the MEMS-supported high-contrast grating (HCG) reflector in VCSELs. The unique properties of the HCG as a lightweight, ultra-high-reflectivity mirror enable optomechanical forces to be more salient in these devices than in typical distributed Bragg reflector (DBR) VCSELs. Through optical, electrical, and microscopy characterization methods, we demonstrate the use of radiation pressure to drive the mirror through current modulation and self-oscillation, notably producing a large amplitude oscillation resulting in broad-spectrum self-swept light. By demonstrating optomechanical effects in a single device, we simplify the traditional cavity optomechanics experiment and open a new design space in which to obtain the ingredients necessary for feedback-based optomechanical damping. Looking to both the applications of passive cavity optomechanics and those of wavelength-swept VCSELs, we highlight applications for these phenomena and design and fabrication changes to further explore and harness optomechanical forces in VCSELs. Additionally, we show the development of the first physics-based compact model of VCSELs, which enables simultaneous design of VCSELs and circuits to enhance VCSELs' performance in communications, ranging, and optomechanics.

Table of contents

List of figures

Acknowledgments

Thank you first and foremost to my advisor, Prof. Chang-Hasnain, for the years of advice and encouragement. Not only does this dissertation apply topics that Prof. Chang-Hasnain pioneered, it is shaped by the spirit she fosters in her group of spontaneity and collaboration. Her curiosity and warmth have inspired and brought together generations of students and staff into a tight-knit, vibrant group. This provided me with both a deep well of expertise to draw upon in the group and many unexpected ideas that would lead us far from our familiar ground.

Naturally, I would next like to acknowledge the generations of CCHG students who played a role in this work. What began as a training in VCSEL testing with my mentor Weijian Yang grew unexpectedly into the first experiments on optomechanics in VCSELs and provided the foundation of this dissertation. Thank you for sharing many long nights in Cory along with the rigor and perseverance you bring to each and every experiment. To James Ferrara, thank you for your pearls of Nanolab wisdom and brightening even the most crushing fabrication failures with your humor. Chris Chase, Devang Parekh, and Frank Rao— thanks for your wisdom in highspeed VCSEL testing, which provided the background for my VCSEL modeling work. Thanks as well to all my mentors within CCHG, including Wilson Ko, Andy Zhu, Tianbo Sun, Linda Li, and all the previous generations of students whom I did not meet but who left years' worth of insightful sticky notes all around our labs.

The impetus to develop a compact model for VCSELs came from our discussions with Nikola Nedovic and William Walker, then at Fujitsu Laboratories of America. Thanks to you both for bridging between our fields and to FLA for their longstanding support of the compact model's development. The vision of NSF's NEEDS center in extending compact modeling to emerging devices, and Profs. Jaijeet Roychowdhury and Mark Lundstrom in particular, helped bring the VCSEL model from a concept to an industrially useful software package. Thank you to Youmin Wang for assistance with LDV measurements and Frank Ogletree of LBNL for your help in the stroboscopic SEM imaging of VCSEL MEMS. I am particularly grateful to John Lawall of NIST for our conversations and collaboration, and I look forward seeing future research from his group on HCG optomechanics. Lastly, I appreciate the broad range of feedback provided during my qualifying exam and dissertation review by Profs. Liwei Lin, Vladimir Stojanovic, and Eli Yablonovitch.

1 Overview and VCSEL Background

1.1 Dissertation Overview

This dissertation draws upon two fields not typically connected—vertical-cavity surface-emitting lasers (VCSELs) and cavity optomechanics. For readers with a background in either or neither field, we begin with an abridged survey of the most relevant results in each, as well the themes and challenges that led these fields to intersect in this present work. In the following chapters, we outline the history of the VCSEL device, the features that enabled it to spread across the wide world of laser applications, and the obstacles in the way of it addressing new problems. In the next chapter, we review the field of cavity optomechanics, which uses the forces of confined light to drive mechanical systems, and extend the classical description theory of this field to include electrically-driven active cavities such as VCSELs to predict what behaviors this physics can produce in lasers. We then develop optical, electrical, and microscopy methods to catch those phenomena in action in VCSELs and show a range of behaviors not previously observed in the device. Through numerical simulation methods, we confirm that these observed behaviors are best explained by radiation-pressure forces and consider the contributions of competing effects. Since the optomechanical behaviors presented in this thesis were all observed in devices not intended for this purpose, we offer VCSELs design and fabrication advances to enhance VCSEL optomechanical effects and bring these effects to bear on real applications. Finally, we report progress in implementing optomechanically-focused VCSELs.

1.2 Overview of VCSEL Device

In the 57 years since the first demonstration of the laser, the basic concept of the laser has been implemented in an incredible array of forms to solve a wide range of problems. Of those categories, none has been produced in as great quantities as the VCSEL. Since its development in 1979 [1], the VCSEL has outcompeted other lasers in a series of application spaces. In its classic form, a VCSEL consists of an electrically-pumped quantum-well active medium in a sandwich configuration between two distributed Bragg reflectors, all grown epitaxially on a III-V semiconductor wafer. Compared to their predecessors, edge-emitting lasers, VCSELs offered a number of advantages, including compact size, single longitudinal-mode operation, and wafer-scale fabrication and testing. The last feature has proven most critical to the rapid expansion and enduring success of the VCSEL. Whereas edge-emitting lasers generally cannot operate until they were individually cleaved from the wafer and polished, VCSELs can be processed and tested at chip or wafer scales, for significantly higher-volume production. Driven by market forces, VCSELs have progressively displaced other light sources in communications, measurement, sensing, and imaging. These applications have been as close to home as the computer mouse and compact-disk drive and as far-fetched as laser spectroscopy on Mars rovers. Expanding VCSELs into new applications or improving their behavior in old applications, while maintaining scalable production and testing, will continue to be a

fruitful area of research for the foreseeable future. In this spirit, this dissertation seeks to uncover new optomechanical behaviors in VCSELs that could address applications in ranging, sensing, and signal processing, while requiring only minimal modifications to existing VCSEL designs and fabrication technologies.

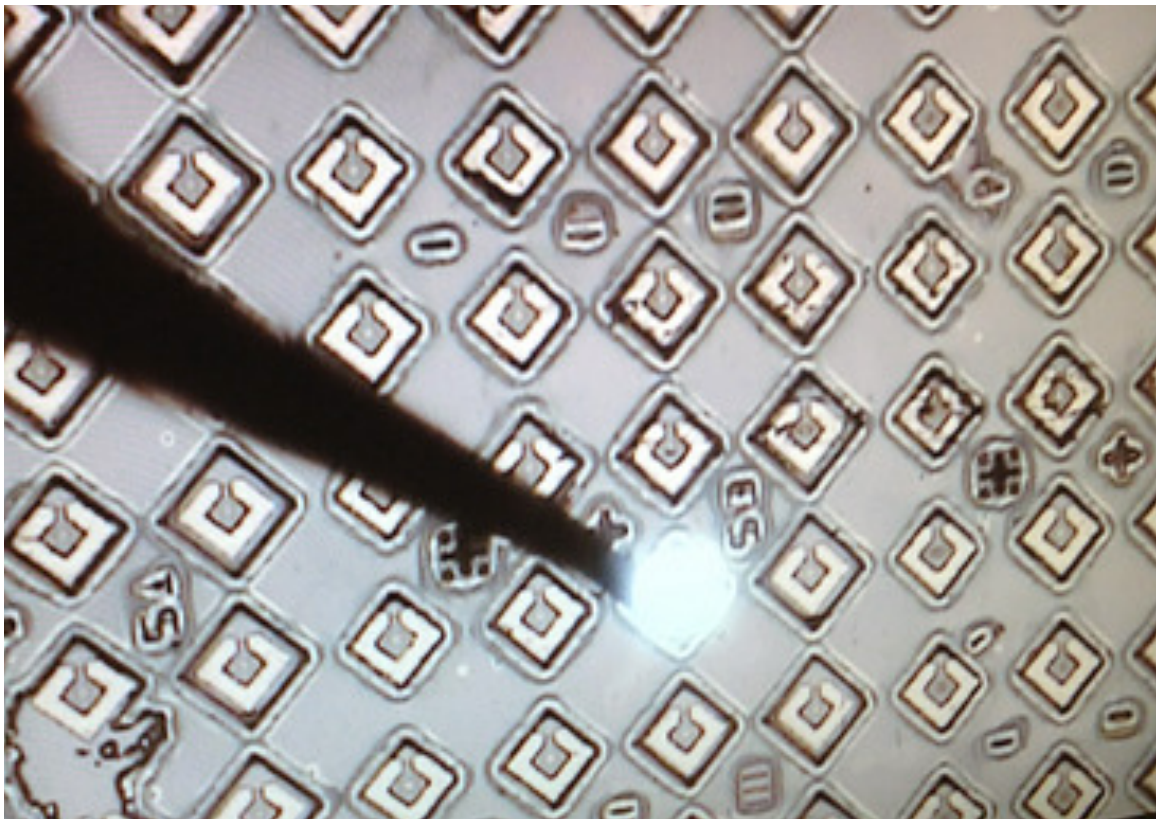

Figure 1.1 VCSELs fabricated at Berkeley under test. Device currently contacted by probe lasing at 850 nm, captured by regular CMOS camera. Illustrates scalability of VCSEL fabrication and testing.

1.3 Mechanical Tunability in VCSELs

Mechanical tunability has been one of the key features added to VCSELs since their original design [2]. Though all VCSEL lasers can change their wavelength thermally under self-heating or external temperature changes, this effect is generally limited to single-digits of nanometers of wavelength shift. Mounting one of the two mirrors of the VCSEL cavity on a micromechanical structure, such as a capacitatively-actuated cantilever, allows VCSELs to tune far more controllably, quickly, and broadly than thermal tuning alone. As in other application domains, mechanical tunability has enabled VCSELs to compete with external-cavity tunable lasers and drive new markets as wavelength-agile transceivers or as broad and fast-swept light sources for ranging and imaging technologies such as optical coherence tomography (OCT). While the figures of

merit for a tuning mechanism vary by application, most seek a large range of motion (few 100s of nanometers), a high mechanical tuning frequency, and critically damped or underdamped motion. Most experiments in this dissertation arose directly from efforts to characterize mechanical tuning dynamics of our group's VCSELs to design frequency-modulated continuous wave (FMCW) light detection and ranging (LiDAR) systems around these VCSELs, and this dissertation will discuss how optomechanical effects in VCSELs can serve those applications.

1.4 High-Contrast Gratings in VCSELs

The most fundamental change in the design of VCSELs has been the push to replace one of the distributed Bragg reflector (DBR) mirrors of the traditional VCSEL structure with high-contrast gratings (HCGs). First theoretically conceived in the group in 2004, HCGs are a domain of subwavelength grating that exhibit exceptionally designable optical transmission properties including high-Q optical resonance and broadband ultra-high-reflectivity[3]. The first proof of the incredible reflectivity of HCGs came through fabricating VCSELs with HCG top mirrors instead of DBRs, implying > 99.9% reflectivity over a 40 nm optical band[4]. In addition to eliminating the time and cost of growing the numerous layers of semiconductor material needed for a top DBR, this work further showed that HCGs provide polarization selectivity and significantly reduced mass, the latter of which provided improved mechanical performance. Since that work, the HCG concept has been extended by our group and others to enable VCSELs at longer wavelengths, at which DBR VCSEL reflectivity suffers due to a lack of refractive index contrast available within the epitaxial materials system [5]. Beyond their initial use as VCSEL mirrors, HCGs have since demonstrated novel behaviors as lenses [6], [7], flexible sources of structural color [8], and numerous other applications [9]. Particularly of relevance to this dissertation, and discussed later, are efforts to characterize the performance of HCGs as optomechanical reflectors, which will be discussed in the following review of cavity optomechanics.

Highly-reflective HCGs in VCSELs are usually fabricated from a < 500 nm thick sheet of semiconductor grown within the epitaxial system. The grating pattern of submicron period is patterned onto the layer with electron-beam or DUV lithography and etched through the layer with dry or wet etching. A sacrificial layer underneath is subsequently removed with wet etching to leave a fully-suspended grating, enabling the high-contrast condition required for high reflectivity. The reflectivity of the 1-D bar pattern of all HCGs discussed in this work is polarization-dependent. Designs optimized to reflect incident light polarized with E-field parallel to the grating bars are referred to as TE reflectors, while designs chosen to reflect light perpendicular to the bars are termed TM reflectors. The fully-released geometry lends itself well to mechanical tuning, which was demonstrated in the first reported HCG VCSEL. The schematic below illustrates DBR-DBR and HCG-DBR VCSELs, showing how both share a fundamental geometry that enables the wafer-scale arrayed fabrication that is the hallmark of the VCSEL's success.

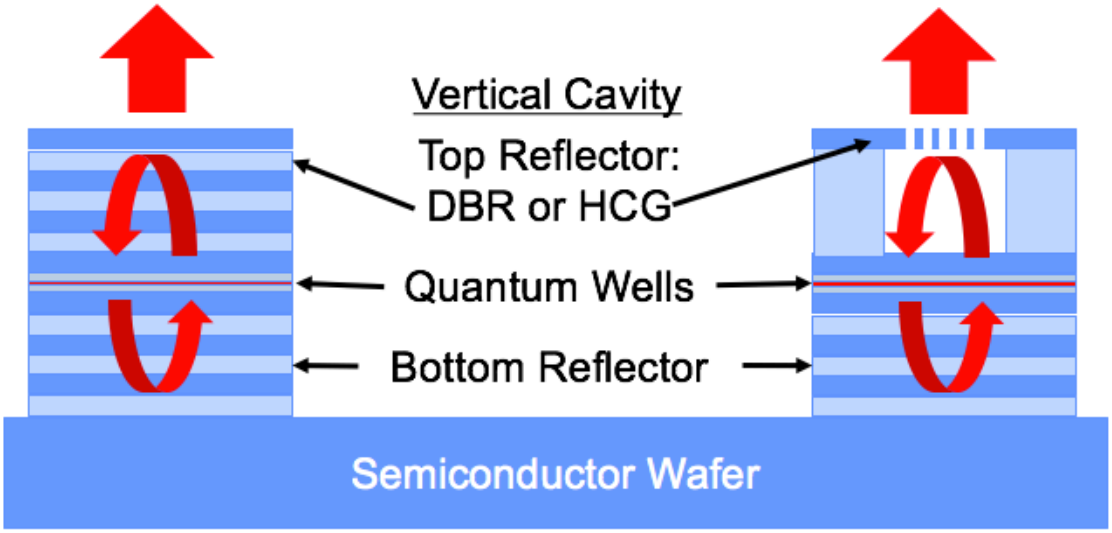

Figure 1.2 Schematic illustrating key similarities and differences of traditional DBR-DBR VCSELs (left) and the HCG-DBR VCSELs used in this research.

2 Cavity Optomechanics: Background and Theory

2.1 Introduction

Light's ability to transfer energy is apparent in many aspects of everyday life and studied throughout history. By comparison, the momentum carried by photons, $p=h\nu/c=h/\lambda$, provides a subtler effect that must be carefully disentangled from competing effects in order to be observed. Technology to construct such physically controlled systems did not exist until the modern era, so the first observations of radiation pressure occurred through astronomy. From 1619, Kepler theorized a force due to the radiation of the sun as an explanation for comet tails' tendency to consistently point away from the sun [10]. As modern mechanics and wave theory came to be applied to astronomy, astronomers in 1903 calculated a deviation in comet's orbits due to the same radiation pressure from the sun's light [11].

Constructing situations in which light could perform mechanical work required both modern developments in mechanics and careful physical analysis. Several themes run throughout the course of efforts to devise optomechanical systems: isolation of the mechanical systems from the environment, miniaturization of mechanical components, and the difficulty of discerning radiation pressure from other light-induced forces. In addition to radiation pressure, light has been observed to produce mechanical work through a variety of thermally-mediated interactions. An example known to many children is the Crooke's radiometer, developed in the 1800s, which consists of a set of windmill-like vanes colored black on one side and white on the other, which spin in the

presence of sunlight. Despite the popular misconception that the device spins due to radiation pressure, the force originates from a difference in air pressure resulting from different temperatures on the black and white sides of the fins. This difficulty in differentiating radiation-pressure forces from thermally-mediated radiation-induced forces occurs in microscale devices as well, as will be noted later in this work in the Analysis chapter. The inclusion of thermally-mediated optical forces, in addition to direct radiation-pressure forces, precludes drawing a concise boundary to the field of optomechanics. As an extreme example, solar-thermal power plants produce mechanical motion in a turbine through the generation of steam by optical absorption, but the optical and mechanical components are sufficiently separated as to provide little insight when studied together. This definition of optomechanical forces—any force exerted by light that does not rely on an intermediary mechanism that could enable decoupling of the system—provides a limit, albeit a generous limit, on the realm of what forces besides radiation pressure can be termed optomechanical.

The forces exerted by light became most prominent when highly-sensitive mechanical apparati were combined with high-finesse optical cavities, in engineered systems both microscopic and macroscopic. In addition to confining light to increase its effective power, optical cavities supported by movable mirrors changed the nature of optical forces from a simple steady-state pressure to a feedback force. As noted by Braginsky in a seminal theoretical work, the delayed response of changes in radiation force to mirror position produces either antidamping or damping [12]. Since this theoretical observation occurred during the infancy of lasers, Braginsky was first able to demonstrate both damping and antidamping in macroscopic microwave cavities [13]. In the decades following that observation, the intersection of the fields of micro-optics and micromechanics provided increasingly sensitive mechanical systems and optical cavities with increasingly high finesse, leading to a fruitful space for both theoretical and experimental exploration. Simultaneously, advances in microwave technology from large-scale cavities to on-chip, cryogenically-cooled LC-resonators provided a complementary technological space in which to implement the same physics as optical-frequency cavity optomechanics. From the first observation of optomechanical damping to recent efforts on ground-state cooling, many of the key advances of cavity optomechanics have come from microwave technologies [14].

While radiation pressure effects provide a useful means to excite or cool vibration in a mechanical structure, it also introduces noise into the position of the mirror in a Fabry-Perot interferometer. A vein of theoretical analysis shows that this effect provides a limit on the accuracy of interferometric measurements of displacements. For interferometric measurement systems in which all sources of noise have been addressed, radiation-pressure feedback effects lead to increasing position measurement noise beyond an optimal value of input laser power. The displacement sensitivity of the interferometer at this input power value is termed the standard quantum limit (SQL). Achieving beyond-SQL displacement sensitivity using squeezed light has been a major thrust of optomechanics research [15].

The first observation of feedback-based radiation pressure effects in optical cavities was performed by Dorsel et al. in 1983[16]. The system consisted of Fabry-Perot cavity of high-reflectivity dielectric mirrors, one of which was suspended by tungsten wires in a gravity-based pendulum. Given the few-Hz mechanical resonance frequency, substantial care was required to isolate environmental sources of vibration in the mirror, which are far greater in the few-Hz regime than the high-kHz through GHz ranges of most MEMS structures. In an evacuated chamber tied to bedrock, and operating at night to minimize vibration, the mirror was sufficiently stable to show multiple optomechanical effects: bistability, spring stiffening, and cooling. Bistability appeared as a hysteresis effect of output power vs. up- and down-scans of input power at constant input wavelength. As the authors note, this bistability results from separate on-resonance and off-resonance solutions to the static equations of motion given the nonlinear spring force of radiation pressure. Likewise, the authors found that in the regime of optical power at which bistability occurred, the mirror's resonance frequency Ω_m, measured from the discrete Fourier transform of output power, was substantially perturbed due to the effective optical spring force. Lastly, the authors noted a regime of optical input power that resulted in the disappearance of the mechanical resonance from the PSD of output power. While they termed this effect "stabilization," it was visibly an instance of optomechanical cooling, the removal of mechanical vibration from the given mode. While these phenomena, and many others, have since been implemented in a variety of macroscale and microscale optical cavities, this first demonstration is notable for its ability to demonstrate optomechanical phenomena in an archetypal system using careful control of macroscopic noise sources.

The years following that experiment saw an expansion of the range of phenomena that theoretically could be achieved using cavity optomechanics. These notably included the production of quantum entanglement between cavity photons and mechanical phonons[17] and feedback cooling of the mechanical mirror [18]. Experimentally, feedback cooling was realized by observing the vibrational modes of fixed mirrors, whose higher mechanical frequency insulated them from ambient vibrational noise more than pendulum-supported mirrors [19].

In parallel with work on macroscopic cavities, a separate vein of research sought to move to micro-optical cavities, which would strengthen optomechanical effects by lowering the effective masses and increasing the confined optical power inside cavities. The first such results relied on photothermal effects, which artificially increase the delayed response of the radiation pressure force and thus the optomechanical damping or antidamping, as will be discussed later. The ability to achieve high mechanical Qf-products, while improving optical Q-factors to compete with passive cavities, have gradually made microscale and nanoscale optomechanics the dominant area in research interest. Fruitful categories of micro-optomechanical devices have been nanotoroidal resonators [20] and photonic crystal nanobeam and zipper cavities [21].

2.2 Selected Theoretical Analysis of Passive Optomechanical Cavities

The field of passive cavity optomechanics has produced far too broad a range of phenomena to recount here, particularly given the excellent review efforts produced within the field [22]. The goal of providing a theoretical analysis of certain passive-cavity optomechanical behaviors is to serve as a backdrop and contrast for theory of active cavities presented later. This primarily concerns classical phenomena in statics, spring stiffening, and feedback-based anti-damping and damping.

Light incident on a highly reflective surface will exert a radiation pressure due to the change in photon momentum at the interface:

$$P_{rad} = \frac{2F_i}{c}\cos^2\theta \tag{2.1}$$

In this equation, F_i represents the incoming energy flux of light (W/m^2) and θ the angle of incidence from the normal. Given that confining light necessarily means changing the momentum of photons, any confined light will exert a pressure on its container according to the above equation. In circular cavities (toroids, spheres, Sagnac interferometers), incidence is far from normal and pressure is provided throughout the course of the cavity wherever a bend in the path occurs. However, in Fabry-Perot and other cavities in which the light normally strikes a discrete mirror, the above can be simplified to describe the total radiation force on the mirror in terms of the cavity circulating power P_c.

$$F_{rad} = \frac{2P_c}{c} \tag{2.2}$$

In the steady state, the aforementioned circulating power in an optical cavity with optical resonance frequencyω_c driven by a laser of optical frequency ω_L can be described by the Lorentzian lineshape of the cavity:

$$P_c = \frac{\kappa_{in}}{(\omega_C - \omega_L)^2 + \left(\frac{\kappa}{2}\right)^2} P_{in} \tag{2.3}$$

where κ_{in} is the field input rate and κ is the total decay rate of field in the cavity due to all sources (absorption, output coupling, and coupling back through input), also corresponding to the Lorentzian linewidth of the cavity. Enabling the cavity to be mechanically tuned through the position of the mirror x (or, more generically, any mechanical mode of the mirror that changes the cavity length), radiation pressure has now become a position-dependent force with a strongly nonlinear dependence on position:

$$F_{rad} = \frac{2\kappa_{in}/c}{\Delta^2 + \left(\frac{\kappa}{2}\right)^2} P_{in} \tag{2.4}$$

Where $\Delta = (\omega_C(x) - \omega_L)$ is the detuning between the input optical frequency and the current position-dependent cavity resonance frequency. For a simple cavity wherein x

represents motion of the whole mirror in the longitudinal direction of the cavity, $\omega_C(x)$ can be simply represented as:

$$\omega_C(x) = \frac{2\pi mc}{L_o + x} \approx \omega_o - \frac{\omega_o x}{L_o} = \omega_o + Gx \tag{2.5}$$

where m represents the longitudinal mode order of the mode originating with length L_o and optical frequency ω_o. While the derivative of cavity optical frequency versus position, *G*, provides an adequate view into the strength of optomechanical coupling in a simple cavity, its meaning is confounded for mechanical systems wherein the position *x* is a generalized coordinate of a complex mechanical motion. In such situations, *x* could be arbitrarily scaled by a constant; for the example of the breathing of a toroidal cavity, *x* could represent the change in radius, or the change in diameter, of the cavity. Accordingly, comparison of optomechanical coupling strength across multiple implementations of cavity optomechanics is conventionally made by normalizing *G* by the zero-point fluctuation amplitude of the given mechanical mode with effective mass m and mechanical frequency Ω_m:

$$g_o = Gx_{zpf} = G\sqrt{\frac{\hbar}{2m\Omega_m}} \tag{2.6}$$

Termed the coupling strength, it quantifies the interaction (in dimensions of frequency) between a single photon and phonon respectively in the optical and mechanical resonators.

The simplified picture presented above illustrates a number of effects that will happen in passive optomechanical cavities. In steady-state, mirror will rest at the position at which the spring force balances the radiation force. The nonlinearity of the radiation force versus position, forming a Lorentzian-shaped F(x), leads to the possibility of bistability for situations in which the laser is detuned to the red of the resting cavity wavelength.

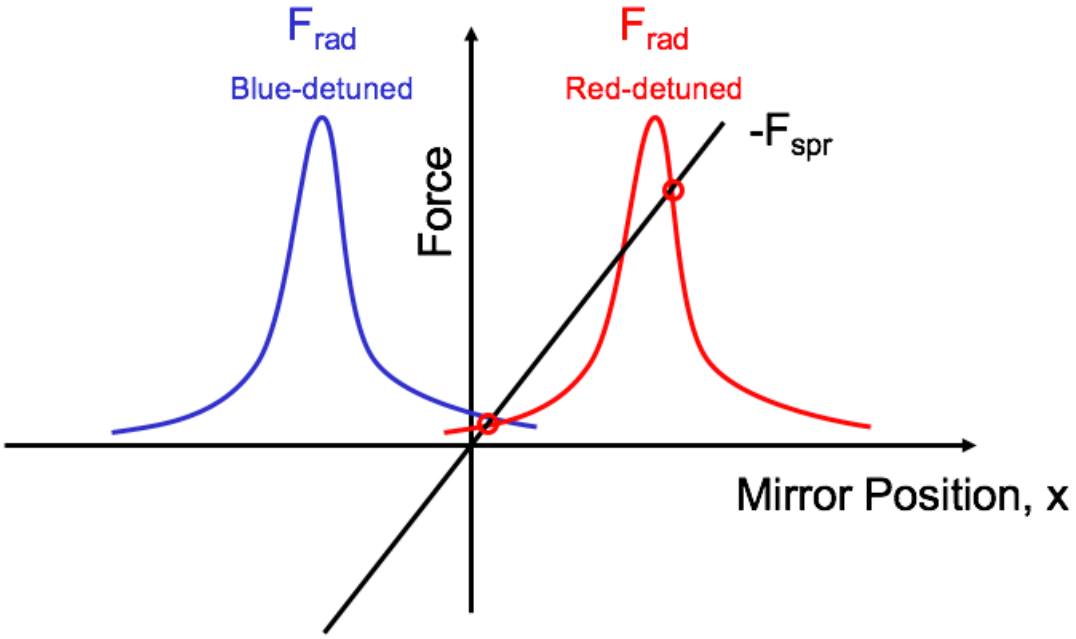

Figure 2.1: Diagram of bistability in optical cavity under red-detuned laser.

At any such stable resting position, the interaction of the linear spring force and the nonlinear radiation pressure "optical spring" force places the laser in a potential well with an effective spring constant differing from that of the mechanical spring constant. This will lead to a change in mechanical resonance frequency versus the input power and wavelength of the laser.

$$k_{eff} = k_{spr} - \frac{dF_{rad}}{dx} \tag{2.7}$$

2.2.1 Feedback-Based Effects

The above quasi-steady-state picture leaves out the majority of interesting optomechanical behavior that originate from the feedback effects found in a dynamic analysis. Intuitively, changes in the mirror position or input power cannot immediately change the resulting circulating power, but rather act over a timescale set by the net cavity decay rate. While the purely position-based, immediately-responding force would be completely conservative, a delayed response adds the ability to do positive or negative work on the mechanical system. Independent of cavity optomechanics, adding a delay term τ to a simple harmonic oscillator with local force gradient $\frac{dF}{dx}$ produces an effective damping:

$$b_{spring} = \frac{dF}{dx} * \tau \tag{2.8}$$

A delayed spring force thus produces antidamping (positive mechanical work), while a delayed anti-spring force ($k_{eff} < 0$) produces added damping. This intuitive picture applies across various domains of optomechanics and to other oscillators as well. This damping acts in addition to the mechanical damping rate b_i, which results from air resistance, internal friction, and anchor loss, to create an effective damping:

$$b_{tot} = b_i + b_{spring} \tag{2.9}$$

In cavity optomechanics, the response of the radiation force to changes in mirror position provides the above delayed spring force and corresponding damping. For the specific case of a Fabry-Perot-like cavity with only radiation-pressure actuation, analysis of the full time-domain dynamical equations of both the passive optical cavity and the damped harmonic oscillator can calculate the optomechanical damping. As derived in Aspelmeyer, the antidamping depends on the key parameters of the optical and mechanical resonator,

$$b_{rad} = n_{cav} g_o^2 \left(\frac{\kappa}{\frac{\kappa^2}{4} + (\Delta + \Omega_m)^2} - \frac{\kappa}{\frac{\kappa^2}{4} + (\Delta - \Omega_m)^2}\right) \tag{2.10}$$

where n_{cav} represents the average circulating photon population and the other parameters are as previously described. Equation 2.10 illustrates many key features of optomechanical damping. Notably, the equation is antisymmetric with respect to laser-cavity detuning Δ, producing a negative b for $\Delta = (\omega_C(x) - \omega_L) > 0$ and positive b for $\Delta < 0$. Those situations correspond, respectively, to antidamping in the blue-detuned case and increased damping in the red-detuned case. The results of both cases are subtle and demand further scrutiny. In the blue-detuned (antidamping) case, increasing optomechanical antidamping will lead to an increasing mechanical Q-factor until the device becomes effectively undamped when $b_{eff} = 0$. At that point, the thermal fluctuations of the mirror will grow into mechanical self-oscillations in an effect analogous to the optical laser threshold. In this regime, the nonlinearity of the underlying equations, which is ignored in the simple antidamping picture, becomes critical to determine the stable self-oscillation amplitude, the phase noise behavior of that oscillation, and the onset of effects such as chaotic motion.

In the red-detuned case, the increased optomechanical damping will not simply act to make a lower mechanical Q-factor. Thermodynamically, damping acts as a means of equilibration. Regular mechanical damping tends to bring the phonon population in the mechanical mode towards the population expected at the temperature of the thermal bath, e.g. the surrounding air or substrate. Input laser light consisting of photons in a single mode is notably not at thermal equilibrium. However, the very low power spectral density of laser noise at mechanical frequencies, compared to that of the mechanical

oscillator at room temperature, allows input light to be approximated as a zero-temperature reservoir. Thus, the optomechanical damping cools the target mechanical mode (reduces the phonon population). Entropy is transferred into the light through the creation of sidebands at $\omega_L \pm \Omega_m$, of which the higher-energy sideband will be larger amplitude. Within the classical domain (i.e. with more than a few phonons occupying the mode), the resulting effective temperature T_c can be approximated based on the intrinsic damping b_i, optomechanical damping b_{om}, and the ambient temperature T_o:

$$T_c \approx \frac{b_i}{b_{om} + b_i} T_o \tag{2.11}$$

which can intuitively be understood as equalizing the flows of heat from the zero-temperature reservoir to the cooled mechanical mode and from the mechanical mode to the ambient environment. Most of the interest in optomechanical cooling in the literature exists in the quantum (few-phonon) regime, wherein the above approximation breaks down due to the need to consider both the laser amplitude noise at the mechanical frequency and the occupation of the optical cavity with photons at the mechanical frequency. However, since optomechanical cooling is not demonstrated for active cavities in this thesis, the classical picture suffices for the remainder of the work shown herein.

While the above analysis has only considered radiation pressure, many key optomechanical results in both self-oscillation and cooling have instead been obtained using photothermal forces. In such systems, absorption of light in the cavity or in one mirror drives thermal expansion, actuating the mechanical mode. Like radiation pressure, photothermal forces are proportional to circulating optical power in the steady state. However, calculation of photothermal forces can be difficult, requiring numerical simulation of the mechanisms of optical absorption, thermal dissipation from the structure, and thermal expansion. Though a general theoretical analysis is not possible here, the delayed-spring picture of optomechanical damping broadly applies to this mechanism as well. Compared to radiation pressure, photothermal forces act with yet another delay term: the optical time constant τ_{th} in which the mechanical structure heats and cools. Even for microscale systems, $\tau_{th} > 1/\kappa$ dominates over the optical cavity response time, providing a means to separately enhance the two ingredients that contribute to $b_{OM} = dF/dx * \tau_{th}$. For this reason, photothermal actuation has produced notable results in both self-oscillation and cooling. Though it may be very counterintuitive that heating a structure with confined light can cool specific mechanical modes in the same structure, this speaks to the low coupling between mechanical modes and the ambient environment even in the same device. This insight—that decoupling the mechanisms of the spring force and delay time can enhance optomechanical damping—features prominently in the analysis of optomechanics in active cavities in this dissertation.

This abridged review of passive optomechanical theory highlights several of the key figures of merit for optomechanical systems that enable comparison between semiconductor nanocavities, superconducting microwave cavities, LIGO-scale

macroscopic interferometers, and the range of other devices in which optomechanical phenomena occur. Within mechanical properties, the comparison between intrinsic mechanical damping b_i and optomechanical damping b_{om} provides both a threshold condition to observe self-oscillation and a classical limit to cooling temperature. While minimizing mechanical losses is a goal across most fields of optomechanics, mechanical structures are typically compared for their product of mechanical quality factor and frequency (Qf product), a metric also used throughout the mechanical resonator field. Given that phonon occupancy at room temperature is proportional to $\hbar\omega_m/k_bT$, the Qf product corresponds the number of periods over which a resonator can be expected to maintain coherence given a normal thermal population of phonons. Additionally, the ratios of g_o/κ and Ω_m/κ prove valuable in obtaining cooling to the quantum (few-phonon) regime.

2.3 HCGs in Passive Cavity Optomechanics

Out of the wide range of passive optical cavities that have been used in optomechanics research, HCG reflectors have already proven to be a fruitful space for development, driven primarily by the efforts of John Lawall and collaborators at the National Institute of Standards and Technology (NIST). By fabricating HCGs from silicon nitride, rather than the III-V semiconductors typically used for VCSEL HCG mirrors, Kemiktarak *et al.* demonstrated gratings with > 99.4% reflectivity at 1575 nm, demonstrated by using the grating as one mirror in a high-finesse (F = 1200) optical cavity in vacuum[23]. Characterizing the RF spectrum of the Pound-Drever-Hall (PDH) error signal revealed diverse, high-Q_m modes in the HCGs. These mode frequencies were found to bear similarities to the eigenfrequencies of a solid sheet, $\omega^2 \propto m^2 + n^2$. Mechanical ring-down measurements confirmed that these diverse mechanical modes showed uniformly high quality factors of 1 x 10^5 to 8 x 10^5 for frequencies ranging from 140 kHz to 300 kHz, demonstrating a high Qf product on the order of 100 GHz. This result provided a demonstration of the high optical and mechanical quality of the SiN-based system. These properties were harnessed to demonstrate optomechanical cooling of multiple such modes, reaching effective temperatures T_{eff} as low as 1 K starting from room temperature, indicating $b_{om}/b_i \approx 300$ [24]. These results, and subsequent collaboration with the Lawall group, proved very important in understanding the mechanism of optomechanics in HCG VCSELs.

2.4 Optomechanical Forces in Lasers in Literature

While the thrust of cavity optomechanics research has broadly focused on passive cavities, optomechanical effects in active cavities have been theoretically and experimentally described in limited cases. Most such works seek to explain certain laser behaviors but do not attempt to develop active cavities as full-fledged branch of cavity optomechanics.

In 2002, Rod Tucker and other researchers then at Agilent experimentally characterized the undesired effects of radiation pressure on MEMS-tunable Fabry-Perot filters designed for telecom [25]. Radiation pressure was noted to produce a shift in the etalon's center

wavelength, leading to noticeable hysteresis in the response of the etalon to a wavelength-swept input from a commercial tunable laser. Further effects noted included MEMS spring stiffening due to changing photon population in the cavity versus input wavelength. While the experimental aspect of that effort did not characterize radiation-pressure effects in MEMS-tunable lasers, it noted theoretically that radiation pressure would produce chirp, a change in laser frequency versus output power. The frequency change due to chirp, $\Delta\nu$, was quantified based on laser parameters as:

$$\Delta\nu = \frac{4\Delta P_{out}(FSR)}{c^2(1-R)k_m} \qquad 2.12$$

In that equation, *FSR* represented the laser's free spectral range, while *R* denoted mirror reflectivity and k_m the spring constant. While the paper did not show this effect occurring in lasers, it predicted that high-finesse, low-spring constant lasers would exhibit unacceptable degrees of chirp.

Five years later, in 2007, Halbritter *et al.* at TU Darmstadt and Two-Chip Photonics AG observed the radiation-pressure chirp mentioned by Tucker *et al.* [26]. Through a detailed theoretical study and experimental analysis of the mechanical tuning dynamics of VCSELs produced by that group, this effort was able to show evidence of a number of mechanical effects including radiation pressure. The devices under test were optically-pumped MEMS-tunable VCSELS operating at 1.6 μm with two DBR mirrors per devices. A two-chip bonding process developed by that group enabled a large initial air gap of 13.2 μm between the top of the epitaxial structure and the bottom of the arm-supported DBR. Experimentally, the device was characterized with the FM discriminator method, in which the modulated light is passed through an optical filter to measure both frequency and amplitude modulation. To compare and identify a range of effects in the laser, the chirp-to-power ratio (CPR) of the laser was plotted in GHz/mW versus modulation frequency over the frequency range of 10 kHz to 2 GHz. The CPR was found to include contributions from three effects that actuated the mirror mechanically: radiation pressure, radiometric pressure, and thermal-induced length extension. These forces are familiar from field of cavity optomechanics, where the latter two would fall into the category of photothermal effects. Using theory following Tucker *et al.*, the radiation pressure CPR was determined to be – 11 GHz/mW. Radiometric pressure, the effect behind the famous Crooke's radiometer mentioned earlier, resulted in this device from the temperature difference between the hotter bottom side of the movable DBR and the cooler top side, which was exposed to significantly less optical power. Through 3-D modeling of the thermal profile of the movable DBR, radiometric chirp was determined to be -4 GHz/mW. Lastly, length extension considered the vertical motion of the DBR due to the thermal expansion of DBR's support arms. Simulations of the thermal profile of the DBR and support arms revealed that an increase of 1 mW of laser power would result in horizontal expansion of 1 nm of the support arms. These opposing horizontal extensions would lift the DBR by 26 nm, equivalently producing -170 GHz/mW. While all three effects would be limited by the mechanical resonance frequency of the device (15 kHz in this case), the latter heating-based effects would also be limited by the relevant thermal time constants,

which were found to be higher than the mechanical time constant and thus irrelevant in this case. The combined prediction of -184 GHz/mW corresponded well with the measured -208 GHz/mW, and the frequency response matched the 15 kHz mechanical resonance frequency. These optically-induced micromechanical (or optomechanical) effects were found to be dominant in magnitude compared to, though out of phase with, the effects of self-heating and carrier concentration, which dominated at frequencies well above the mechanical resonance frequency. Those effects, present even in VCSELs without mechanical tuning, have been extensively studied elsewhere, both previously and since [27].

Contemporaneously with our work, Czerniuk *et al.* demonstrated coupling between the lasing cavity and phonon modes in nontunable, optically-pumped VCSELs. Under pumping from a femtosecond pulsed laser, the temporal profile of the VCSEL's output light showed ringing due to the excitation of phonon modes in the VCSEL. The effect of phonons on the output light was enhanced by layered DBR mirrors acting as phonon reflectors, thus creating a high-finesse phononic resonance. In contrast to the work described herein, this paper did not demonstrate sustained self-oscillation of the mechanical (phononic) mode in question, and thus is analogous to the research on modulation-induced optomechanics here. This work's approach of using phonons within nontunable VCSELs bears advantages in the high frequency of the resulting phonon modes (17 - 40 GHz), which can unlock applications related to highspeed modulation of VCSELs in telecom and, eventually, the generation of near-THz frequencies difficult to produce with electrical means.

Viewed together, these references provide clear indication that both radiation pressure and photothermal effects in laser cavities strong enough to produce effects noticeable in the laser output. However, such effects have, to date, only become visible in niche cases of laser design and characterization: as a contributory effect in the chirp response of a tunable VCSEL and as a response to femtosecond-pulsed pumping in a highspeed, optically-pumped laser. Though these results may be heartening, substantial room exists to develop both the theory and application of optomechanical forces in lasers, particularly VCSELS.

2.5 Theoretical Analysis of Optomechanical Dynamics

2.5.1 Calculation of HCG Reflectivity Spectrum

The reflectivity spectrum of a VCSEL's HCG mirror is one of the critical parameters needed to support tunable lasing, which requires a high reflectivity (typically >99.9% without supporting DBRs) across the entire desired tunable band. However, as discussed in following sections, optomechanical self-oscillation dynamics depend subtly on the reflectivity's magnitude, $R(\lambda)$, and the spectrum derivative, $\frac{dR}{d\lambda}$.

Unfortunately, direct measurements of the reflectivity spectrum of an as-fabricated HCG integrated into a VCSEL have not yet been demonstrated due to the confounding effects of the attached laser cavity. Nonetheless, both rigorous coupled wave analysis (RCWA)

[28] and an array-waveguide mode expansion method developed in our group [29] have shown good performance in predicting HCG reflectivity for laser design and other applications. Despite the lack of direct experimental confirmation, that these analysis methods have been used to design several generations of VCSEL lasers in our group and other groups demonstrate these methods' accuracy in predicting reflectivity spectra, as reflectivity error of > 0.1 percentage points would be a fatal defect in a VCSEL. To parametrize $R(\lambda)$ to enable theoretical analysis of the optomechanical rate equations, we use a quadratic fit of reflectivity around the peak wavelength:

$$R_H(\lambda) = R_{H,p} + R''_H \cdot (\lambda - \lambda_p)^2 \qquad 2.13$$

Previously, we have shown that the quadratic model fits RCWA-calculated reflectivity across the lasing range of the device used in Section 3.7 [30]. The fitting values for that 1550 nm device, as included in Table 2.1, were R''_H of -4.1x10^{12} m^{-2}, and the theoretical peak reflectivity $R_{H,p}$ of unity. It is a distinctive feature of the interference-based origins of reflection in HCG that complete reflectivity is even theoretically possible, analogous to complete interference in an interferometer, whereas DBR reflectivity only approaches unity for infinitely repeated DBR pairs. While efforts in both laser design and visible HCGs have shown RCWA to be an excellent predictor of real HCG reflectivity, this application is the most demanding HCG simulation to date as it depends on the gradient of the reflectivity spectrum. There is some inaccuracy of the RCWA-calculated reflectivity spectrum because RCWA assumes an incoming plane wave, while the real VCSEL mode has a lateral profile of a Gaussian or higher-order shape. Some effort to account for this can be made by treating the input wave as a summation of plane waves at a spread of input angles. Generally, this is not accounted for except in studies of multi-transverse-mode behavior in HCG VCSELs, since the large proton-implant-defined aperture of 1550 nm VCSELs in this chapter limit the angular spread to a full-width-half-maximum of 3~5 degrees. Other effects limiting the applicability of RCWA include sidewall roughness of the grating (on the order of SEM resolution of 10 nm). This could reduce the overall HCG reflectivity and decrease its bandwidth, increasing R''_H and decreasing R_{H_p} in the quadratic fitting above. Accordingly, we claim R''_H to be in a range of -5x10^{12} m^{-2} to -1x10^{13} m^{-2}, and R_{1p} in the range of 99.5%~99.8%. While the exact numbers noted in this analysis apply particularly to the TE-HCG 1550 nm devices used in many experiments herein, the quadratic shape of the reflectivity spectrum applies generally to HCG designs in the near-unity reflectivity regime. Therefore, the quadratic form will be used in the subsequent analytical treatment of radiation pressure effects.

2.5.2 Rate Equation Analysis of VCSEL Dynamics with Radiation Pressure

To begin to describe optomechanical effects in VCSELs, we join together the standard models for the two components: the rate equations for the laser dynamics and a harmonic oscillator model for the mechanical mode. Appearing in a variety of texts and papers in a

range of forms, laser rate equations vary greatly depending on what effects they choose to incorporate. A reasonably complete form, based on Coldren and Corzine [31], is as follows. Term by term, the first equation describes carrier population under the processes of injection; nonradiative, spontaneous, and Auger recombination; and stimulated emission into the lasing mode. The second equation describes cavity photon concentration under stimulated emission, cavity absorption, losses to both mirrors, and spontaneous emission into the lasing mode.

$$\frac{dN}{dt} = \frac{\eta I}{qV_a} - (AN + BN^2 + CN^3) - v_g g_o \frac{S}{1+\varepsilon S}(N - N_{tr}) \quad 2.14$$

$$\frac{dS}{dt} = \Gamma v_g g_o \frac{S}{1+\varepsilon S}(N - N_{tr}) - \left(\alpha_i + \frac{1}{2L} ln \frac{1}{R_1(x)} + \frac{1}{2L} ln \frac{1}{R_2}\right) v_g S + \Gamma \beta B N^2 \quad 2.15$$

Those rate equations describing laser dynamics couple to a damped, linear harmonic oscillator describing the MEMS, driven by electrostatic force and the optomechanical radiation pressure and photothermal forces. The electrostatic force will be discussed in more detail in following sections.

$$m\ddot{x}(t) + b\dot{x}(t) + m\omega_o^2 x(t) = F_E\big(x, V_T(t)\big) + F_{RP}(x,t) + F_{PT}(x,t) \quad 2.16$$

The above rate equations and optomechanical equation depend on a number of material and device parameters to solve for the relationship between device inputs (I_d, V_t), internal variables (N, S, x), and outputs (P, λ). In Table 2.1 we present a parameter set to apply Equations 2.14-2.16 to the 1550 nm VCSELs used in this work.

Table 2.1: Parameters and sources used to describe optomechanics in 1550 nm VCSELs

Symbol	Definition	Typical Values (1550 nm HCG VCSEL)	Source and References
I	Injection current	5~20 mA	Input variable
N	Carrier concentration	~10^{18} /cm^3	Internal variable
S	Photon concentration	~10^{14} /cm^3	Internal variable
N_{tr}	Carrier concentration at transparency condition	10^{17}~10^{18} /cm^3	Value from [31]
A	Shockley-Read-Hall recombination coefficient	5×10^{7} /s	
B	Spontaneous emission coefficient	8×10^{-11} cm^3/s	

C	Auger recombination coefficient	3.5×10^{-30} cm^6/s	
η	Injection current quantum efficiency	0.9~0.95	Value from [31]
g_o	Differential gain	$1\times10^{-16}\sim 3\times10^{-16}$ cm^2	Quantum well design, [31]
ε	Gain suppression ratio	2×10^{-17} cm^3	
β	Rate of the spontaneous emission coupled into laser mode	10^{-4}	
α_i	Intrinsic loss	1~15 /cm	
v_g	Group velocity	$8.5\times10^{7}\sim 1\times10^{8}$ m/s	Transmission-matrix analysis of VCSEL epitaxial structure
V_a	Active region volume	4~25 μm^3	
Γ	Mode confinement factor	0.01~0.04	Transmission-matrix analysis of VCSEL epitaxial structure
L	Effective cavity length	3~4 μm	
R_{Hp}	Top HCG peak reflectivity	>0.99	HCG design and simulation with RCWA
R_H''	Second derivative of top HCG reflectivity to wavelength	$-5\times10^{12}\sim1\times10^{13}/\,m^2$	
R_2	Bottom DBR reflectivity	>0.999	Transmission-matrix analysis of VCSEL epitaxial structure
m	HCG MEMS modal mass	100 ~300 pg	HCG design and FEM simulation
f_o	HCG MEMS mode frequency	0.1~6 MHz	FEM simulation; measurement
Q_m	HCG MEMS modal quality factor	10^3~10^4	Measurement
g_{om}	Optomechanical coupling coefficient	~32.2 GHz·rad/nm	VCSEL epitaxial structure from design; measurement ($d\lambda/dx$)
P_o	Laser output power	0.1~4 mW	Output variable
λ	Laser wavelength	1540 ~ 1580 nm	Output variable

Though they are truly complicated dynamical processes based on the internal state of the laser as described by N, S, and x, optomechanical forces F_{RP} and F_{PT} can be approximated as taking their steady-state values dependent on the mirror position, but with some fixed delay. In the small-signal analysis used to show antidamping and instability, it is possible to break the optomechanical forces in to a static, mirror-dependent component and a delayed-spring antidamping, with different delay values for both optomechanical forces:

$$m\ddot{x}(t) = -\left[b_i + \frac{dF_{RP}}{dx}\cdot\tau_c + \frac{dF_{PT}}{dx}\cdot(\tau_c+\tau_{th})\right]\dot{x}(t) - m\omega_o^2 x(t) + F_{OM}(x) \qquad 2.17$$

The radiation force responds almost instantly to the circulating power (within a cavity circulating time), and can be described based on Equation 2.1 and rate equation parameters in Table 2.1:

$$F_{RP}(\mathrm{t}) = \frac{2\mathrm{P_c}(t)}{c} = \frac{SV_a/\Gamma}{\mathrm{c}L/v_g}\frac{hc}{\lambda} \tag{2.18}$$

It should be noted that the above formula provides an excellent approximation to the fundamental mechanical mode given the assumption of high overlap between the mechanical mode and optical mode. For higher-order mechanical or optical modes, the effective radiation pressure on the mechanical mode should be treated as an overlap integral of the optical radiation pressure and mechanical mode.

$$F_{RP,eff} = \iint P(x,y) z_{mode}(x,y)\,dxdy \tag{2.19}$$

This overlap integral indicates intuitively that certain mechanical modes may be unsuited for driving with wide or higher-order transverse modes. Calculating photothermal force is not as analytically possible because the mechanisms of optical absorption, heat dissipation, and thermal expansion in the structure all require 3-D simulation, which we carry out in Section 4.3 for specific device conditions. However, radiation pressure optomechanics lends itself well to further analysis to understand the threshold condition of optomechanical self-oscillation below.

2.5.3 Derivation of Small-Signal Anti-Damping

As described above, for small-signal displacements the radiation forces can be linearized to a delayed-spring combination of a position-dependent force and fixed delay of the form $\frac{dF}{dx}\cdot\tau(x)$, which adds damping or antidamping to the intrinsic damping b_i of the system. If these terms provide a net damping $b_{eff} < 0$, instability and regenerative oscillation occur. Considering only radiation pressure dynamics, to obtain $\frac{dF_{RP}}{dx}$ and $\tau_c(x)$, we can calculate how the laser behaves dynamically in response to a perturbation of the HCG displacement *x*. This approach follows they well-known derivation of linearized small-signal response of semiconductor lasers to current modulation $I_d(t)$, but instead treats $x(t)$ as the input. Applying sinusoidal inputs to the rate equations in Equations 2.14-2.16 with all input and model variables described as complex phasors:

$$\begin{aligned} x(t) &= x_o + \widetilde{x_1}e^{j\omega t} \\ N(t) &= N_o + \widetilde{N}_1 e^{j\omega t} \\ S(t) &= S_o + \tilde{S}_1 e^{j\omega t} \end{aligned}$$

$$F_{RP}(t) = F_o + \tilde{F}_1 e^{j\omega t} \tag{2.20}$$

Following the notation of Coldren and Corzine, the rate equations with position input linearize to:

$$\begin{bmatrix} \gamma_{NN} & \gamma_{NS} \\ \gamma_{SN} & \gamma_{SS} \end{bmatrix} \begin{bmatrix} \widetilde{N_1} \\ \widetilde{S_1} \end{bmatrix} = \begin{bmatrix} 0 \\ \gamma_x \cdot \widetilde{x_1} \end{bmatrix} \quad 2.21$$

$$\tilde{F}_1 = \frac{2}{\mathrm{c}} \left(\frac{V_a h c}{\Gamma \lambda} \frac{v_g}{2L} \right) \widetilde{S_1} - \frac{1}{\pi c} \left(\frac{S V_a h}{\Gamma} \frac{v_g}{2L} \right) g_{om} \widetilde{x_1} \quad 2.22$$

where

$$\gamma_{NN} = j\omega + A + 2BN + 3CN^2 + v_g g_0 \frac{S}{1+\varepsilon S}$$

$$\gamma_{NS} = -v_g g_0 \frac{S}{(1+\varepsilon S)^2}(N - N_{tr})S + v_g g_0 \frac{1}{1+\varepsilon S}(N - N_{tr})$$

$$\gamma_{SN} = \Gamma v_g g_0 \frac{S}{1+\varepsilon S} + 2BN\Gamma\beta$$

$$\gamma_{SS} = -j\omega - \Gamma v_g g_0 \frac{\varepsilon}{(1+\varepsilon S)^2}(N - N_{tr})S + \Gamma v_g g_0 \frac{1}{1+\varepsilon S}(N - N_{tr}) - \left(\alpha_i - \frac{ln R_1 R_2}{2L} \right) v_g$$

$$\gamma_x = -\frac{1}{2L} \frac{2R_1' \frac{g_{om}\lambda^2}{2\pi c} \left(\frac{x g_{om}\lambda^2}{2\pi c} + \lambda_0 - \lambda_p \right)}{R_{1p} + R_1' \left[\frac{x g_{om}\lambda^2}{2\pi c} + \lambda_0 - \lambda_p \right]^2} v_g S \quad 2.23$$

dN/dx and dS/dx can then be solved with Equation 2.23, and then dF/dx with Equation 2.22. τ_c can be obtained from the phase of the force response:

$$\tau_c = \frac{\phi[\frac{dF}{dx}]}{\omega} \quad 2.24$$

While the above equations become intuitively opaque due to the large number of terms, they do present a closed-form description of the two ingredients, optical spring effect and force response delay, that produce optomechanical damping or anti-damping in VCSELs. As is pursued in the analysis chapter, these formulae provide a sufficient means to evaluate whether self-oscillation will occur in a given situation.

Additionally, the above analysis uses assumptions specific to the simplest case of optomechanical interactions in a VCSEL, particularly that only one mechanical mode present and that this mechanical mode does not involve substantial degradation of HCG reflectivity due to mirror deformation. A more complete analysis would involve a system of harmonic oscillators with a generalized coordinate, and independent contribution to reflectivity change, for each mode.

3 Experimental Observation of Optomechanical Behaviors in VCSELs

3.1 Introduction

In this chapter, we highlight the varied experimental methods used to provide a complete picture of optomechanical behaviors in VCSELs. To give context to the following experimental results, we begin by providing more specifics of the HCG VCSEL designs that showed notable optomechanical effects. Since the novel optomechanical effects also depended on parameters not previously relevant to the operation of VCSELs, such as the derivative of the HCG reflectivity ($\frac{dR}{d\lambda}$) and mechanical quality factor in vacuum, we present literature review, simulations, and experiments for the purpose of determining those parameters. Next, we show optical characterization experiments showing a progression of optomechanical effects: first, effects induced by external modulation illustrating the force of light; second, effects under external modulation showing the feedback nature of that force of light; finally, self-oscillation occurring under DC input conditions. To provide a complete picture of this self-oscillation behavior, we present a unique form of characterization imaging the motion of the MEMS in a scanning electron microscope (SEM) using motion blur and stroboscopic effects to prove the mechanical origin of the wavelength sweep. Having established the mechanism of these effects, we search for special cases of self-oscillation under DC inputs, including a notably large amplitude oscillation of 580 nm (producing 23 nm self-swept light) and multi-mechanical-mode self-oscillation illustrating similarities to mode competition and transitions in lasers.

3.2 Device Properties

The HCG VCSELs that we use in this work to demonstrate optomechanical effects use tuning mechanisms similar to those found in Huang *et al.*, Rao *et al.,* and numerous other works in our group. In all such devices, the HCG can be actuated towards the semiconductor layer by applying a voltage across the airgap. The narrow, arm-like supports that suspend the HCG mirror are designed such that the attractive force of a reasonable voltage (usually < 20 V) between the HCG and the substrate produces sufficient force to lower the HCG to its pull-in limit, shortening the cavity length and blueshifting its wavelength. As is standard in both DBR and HCG VCSEL design, we use the transfer matrix method is used to calculate the cavity resonance wavelength λ as a function of HCG displacement x. While a Fabry-Perot filter provides a linear relationship between wavelength and cavity length, this is notably not the case for compound mirrors such as this, in which only part of the mirror (the HCG) changes position. For the device design used in the following work, at the mirror's resting position (V_t = 0), we can linearize this relationship into what we term the tuning ratio, $d\lambda/dx$ = 0.041, a unitless ratio of wavelength change to physical distance traveled. The cavity optomechanics literature instead expresses this quantity as a shift of the laser's angular frequency per

position, called to the optomechanical coupling coefficient G, which here would equal $d\omega/dx = 32.2$ GHz·rad/nm. In many of the lasers subsequently discussed, the top reflector is a compound mirror of a fixed, few-pair DBR and a movable HCG. Since only a fraction of the optical longitudinal mode is exposed to the HCG, the tuning ratio is substantially lower than that of a Fabry-Perot cavity of comparable cavity length L_{eff} and is not constant with respect to mirror position. Figure 4 of the first paper demonstrating a tunable HCG VCSEL by (Huang *et al.*) illustrates the nonlinear relationship of $\lambda(x)$ calculated by the transfer-matrix method [4].

As is commonly presented in the MEMS literature, the dynamics of the mirror under capacitative actuation can be represented as a linear harmonic oscillator driven by a nonlinear, position-dependent electrostatic force. Due to the rigidity of semiconductor materials used in HCG MEMS, the spring force can be treated as linear and elastic:

$$F_{spring} = -kx = k(d - d_0) \tag{3.1}$$

where d_0 is the resting distance between the i.e. HCG and the substrate and d the current distance. These parallel plates separated by an air gap have a position-dependent capacitance $C(d)$. When applying an actuation voltage V, the energy U_e stored in the capacitor is

$$U_e = \frac{1}{2}CV^2 = \frac{\varepsilon_0 A}{2d}V^2 \tag{3.2}$$

where A is the area of the movable part of the HCG and frame, approximating that the bending arms do not contribute significantly to changing capacitance. The electrostatic force can be found as the derivative of this potential:

$$F_e = \frac{\partial W_e}{\partial d} = -\frac{\varepsilon_0 A}{2d^2}V^2 \tag{3.3}$$

At the steady state condition $\Sigma F = 0 = F_{spring} + F_e$, the position is described by a single nonlinear equation:

$$(d - d_0)d^2 = -\frac{\varepsilon_0 A}{2k}V^2 \tag{3.4}$$

This equation for the classic voltage-dependent position in electrostatic MEMS bears several important insights. For small displacements $d \approx d_o$, the mirror positon $x \propto V^2$, while for sufficiently large voltages, no solution exists, leading to the well-described MEMS pull-in effect. Combining Eq. 3.4 and the position-wavelength relationship calculated from transfer matrix method provides a relationship between tuning voltage V

and lasing wavelength λ that has accurately matched measured $\lambda(V_t)$ data for MEMS-tunable VCSELs in the literature. The accuracy of such fits confirms the linearity of the spring constant even at large 100nm-scale of vertical linear motion for > 10μm-scale HCGs and arms.

This theoretical treatment relies on obtaining values for certain key parameters describing the VCSEL mechanics, notably the classic damped harmonic oscillator parameters *k, m, ω,* and *Q*. Previous efforts in the group to design mechanically-tuned DBR-based Fabry-Perot microfilters had already demonstrated analytical formulas for spring constant based on the geometry of the MEMS supports of the device and mechanical properties, particularly the Young's modulus, of the material of the MEMS supports [32]. That paper presented formulas for the spring constant of a variety of MEMS geometries that have been employed in the group to produce both movable DBR and HCG VCSELs. Unless otherwise noted, the devices in this work follow a "bridge" geometry, wherein the mirror is suspended to the solid mesa of the VCSEL by two or more horizontal arms arranged on two or more faces of the HCG. In such a device, can be analytically described based on the material and geometric parameters of the arms as:

$$k = \frac{16Et^3w}{L^3} \qquad 3.5$$

where *E* represents the Young's modulus of the material, *t* represents the thickness of the arms, *w* the width of one arm, and *L* the arm's length. Other designs that rely on torsion, or that suspend the HCG on a one-sided cantilever, are not used for HCG VCSELs currently because of the unwanted tip of the mirror vs. position in the former case and the large space needed for an attractive "counterweight" in the latter case. The above analytical formula for *k* assumes perfect rigidity of the HCG, a condition that cannot be realistically assumed unless the HCG is surrounded by a sufficiently large frame. To incorporate unwanted effects such as HCG deformation or material nonlinearities, we also simulate the MEMS structures using FEM. Such simulations can use either a uniform force applied across the HCG and bars or mesh the airgap for full electrostatic simulations. For the 1550 nm device used in the large-sweep self-oscillation results of Section 3.7, Equation 3.5 predicts k = 0.2 N/m and COMSOL FEM simulates k = 0.17 N/m, a close agreement indicating substantial spring stiffness provided by the frame.

Statically-tuned VCSELs and filters only required estimation of the spring constant in order to calculate the full position vs. voltage characteristics of the device, as the only other relevant parameters (initial air gap thickness and attractive area) can be well calculated from device geometry. The good agreement between simulated tuning vs. voltage data and measurements in the literature confirms the applicability of this simple theory. To complete the linear harmonic oscillator picture of these structures, the initial work on MEMS HCG VCSELs found that the mass of the HCG could be used as modal mass *m* to give good estimation of the mechanical resonance frequency calculated from optical spectrum vs. voltage modulation responses[4]. Additionally, these initial

experimental results showed that typical HCG MEMS structures in air could range from overdamped (Q < 0.5) to weakly underdamped (Q = 3) for comparable HCG structures with increasingly stiff mechanical supports. This confirmed that arm design broadly did not affect air damping b_a for a given structure, and that modal mass remained close to the HCG mass even for stiff support arms. Accordingly, the Q would change with resonance frequency according to:

$$Q = \frac{m\omega}{b} \tag{3.6}$$

While the above analytical picture was sufficient to design and use these tuning mechanisms for statically-tuned telecom applications, applications that required specific wavelength vs. time profiles, such as swept-source imaging, necessitated more thorough understanding of VCSEL MEMS dynamics. This need led to the use of finite-element method (FEM) to simulate the mirror mechanics in more detail and to experimental efforts to characterize the tuning response of laser in vacuum, where it was known that the mirror's response would be less damped. Such efforts, particularly measurements of the tuning transfer function in vacuum, led directly to the observation of optomechanical effects noted in this work.

Across the range of HCG MEMS designs, eigenfrequency analysis FEM in COMSOL corroborated the assumptions and results of the simple analytical picture used to determine spring constant and modal mass for the fundamental mode. The most critical such assumption was that the HCG and frame remained approximately rigid as the mirror oscillated in the fundamental mode. The analytical formulas noted in Mateus *et al.* required this assumption in order to treat the entire HCG and frame mass as the load of the oscillator, and to model the deformation of the support arms as an s-shaped bend with flat, fixed terminations on both ends.

Additionally, FEM showed numerous eigenfrequencies and corresponding modes that had not previously been noted experimentally. Some such modes included: side-to-side vibration or twisting of the HCG in-plane; asymmetric tipping of the HCG with one set of arms up and the other down; and various modes involving motion of the HCG bars while the frame and support arms remained comparably immobile. The modal shapes of these modes illustrated why they had not been previously visible in experiments. Capacitative actuation relies on change in capacitance per distance of generalized coordinate to actuate a mechanical mode. In-plane horizontal modes and asymmetric (half-up, half-down) modes generate no chance in capacitance, and thus are impervious to electrostatic actuation. Likewise, the average change in position is small for even the bar-only modes. This makes intuitive sense given the orthogonality of separate eigenmodes and the large average position change of the fundamental mode. That certain of these higher-order, bar-only modes are found to be actuated optomechanically in this work represents a major success of VCSEL optomechanics.

While measuring spectral width vs. tuning modulation frequency provided an acceptable way to measure MEMS resonance frequency and damping in air, it was readily evident that optomechanical anti-damping perturbed such measurements in vacuum. An accurate measurement of MEMS frequency response in vacuum could only be performed with the laser cavity off, to avoid such confounding effects. To satisfy this requirement, we used a standard MEMS technique, laser Doppler vibrometry (LDV), to measure unperturbed resonance frequencies and mechanical Q-factors of VCSELs in vacuum. The LDV system used was a Polytec OFV-3001 with an OFV-512 fiber-coupled sensor head, owned by the group of Prof. Ming Wu at UC Berkeley. In this system, light from a HeNe instrumentation laser is focused onto the device under test via a microscope, and the velocity of the object is measured via the Doppler shift in the light reflected off the sample. Since the HCG's of the 1550 nm VCSELs are strongly refractive, and not reflective, at 633 nm, sufficient reflection amplitude to obtain a measurement could only be obtained by focusing the laser spot on the corners of the frame through a 50x Nikon objective.

It was not possible to integrate the system with our existing Lakeshore vacuum stage, but a separate vacuum stage including a mount for TO-can packaged VCSELs was used. As a result, the devices tested in LDV were Bandwith10 packaged 1550 nm VCSELs, and while the HCG design was comparable to that used in the on-chip devices of most subsequent experiments in this dissertation, it was not possible to capture LDV results on the exact same devices. In this vacuum system, the pressure could only be pumped to 300 mTorr, compared to the < 5e-5 Torr pressure in all optomechanics experiments carried out in the Lakeshore vacuum cryostage. Discussion will follow as to whether that perturbs the measured mechanical quality factors. Lastly, the system's OVD-02 velocity decoder could capture motion in the frequency domain from DC to 1.5 MHz, providing a means to analyze the fundamental modes of a range of different device designs, but not the higher-order modes (typically > 2 MHz). Since Brownian motion did not produce enough displacement to overcome the noise floor of the instrument, electrostatic white noise up to 15 MHz was applied to the capacitative actuation mechanism of the MEMS using an Agilent function generator.

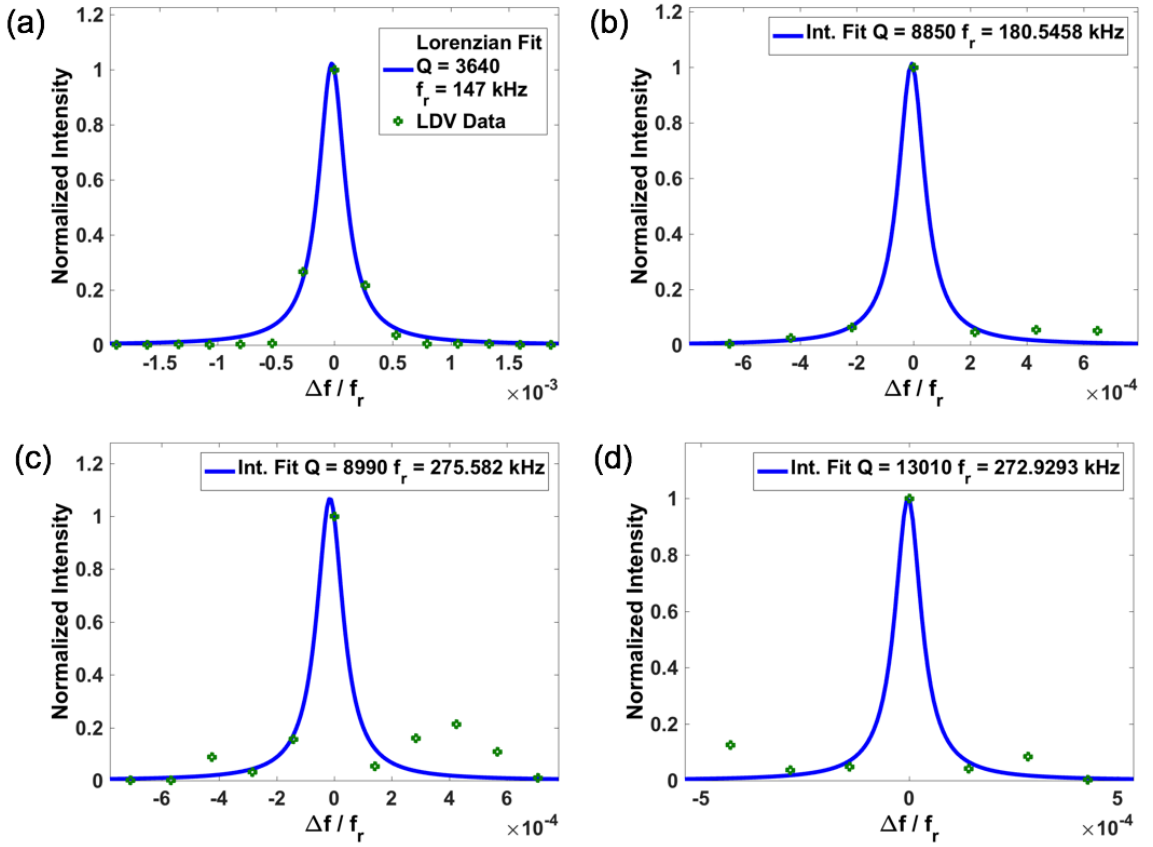

Figure 3.1: LDV results for three HCG VCSELs. Clockwise from top left: device 1; device 2; device 3, bottom left; device 3, top right.

The results revealed the fundamental mode of multiple devices with differing MEMS arm lengths. Fitting with Lorentzian functions to the mechanical intensity (amplitude squared) revealed a large range of quality factors from 3,000 to 10,000, for modes ranging from 146 kHz to 276 kHz. Measurements taken at different corners of the same device showed repeatable resonance frequency measurements to within 3 Hz, but quality factor estimates that could vary by as much as 9000 to 13000. Though the individual data points were far above the instrument's noise floor, the range in quality factor estimates likely arose from the unpredictable coupling of the beam reflected from the HCG. Beyond the non-reproducibility, the trend also broadly showed that higher frequency modes exhibited higher quality factors, though the substantial error bar on the quality factor calculation precluded using regression to compare the exact damping values of these various modes.

Despite the difficulties described above, these measurements serve as an acceptable estimate, and lower bound, on the quality factor of the fundamental mode in the < 5e-5 Torr vacuum at which optomechanical effects occurred. In the simplest possible picture of air damping, ignoring the elastic effects of squeeze-film damping from the substrate < 2 μm below the vibrating HCG, viscous forces from air are inversely proportional to

pressure. In this linear picture, the decreasing air pressure from 760 Torr to 0.3 Torr would result in a quality factor increase from Q ≈ 1 to Q ≈ 2,500, roughly on the order of magnitude with observed quality factors.

By providing a lower bound on the Q in an airless environment, this measurement also provides an upper bound on the damping due to other loss mechanisms, namely thermoelastic damping and anchor loss, two effects that do not depend on air pressure. Since such damping mechanisms add harmonically to the quality factor, the overall quality factor versus pressure can be described as:

$$Q(P)^{-1} = Q_{air}(P)^{-1} + Q_{TE}^{-1} + Q_{anchor}^{-1} \quad 3.7$$

Thermoelastic damping arises in all vibrating solids when internal heat conduction equalizes the temperature between locally expanded and compressed parts of the structure [33]. Anchor loss result from the coupling of phonons from the vibrating structure into the fixed supports. Both are unavoidable damping effects in MEMS, but can be minimized with careful design.

3.3 Modulation-Induced Optomechanical Phenomena

It has long been observed that semiconductor lasers, and particularly VCSELs, change output wavelength under changes in input current (and thus output power), in a behavior typically called chirp. In telecom lasers, chirp is detrimental because the wavelength shift induced by current-modulated data can result in inter-symbol interference through fiber dispersion. However, chirp due to current modulation can be a sufficient tuning mechanism for narrow-band wavelength-swept applications that can tolerate the amplitude modulation that necessarily accompanies chirp-based frequency modulation.

A variety of effects, including self-heating and refractive index change, contribute to chirp, generally producing a redshift versus increased power. While these effects combine indistinguishably under D.C. changes in drive current, the effects can be discerned in the time or frequency domains. Self-heating occurs in typical VCSELs with a delay on the order of 1 μs, determined by the thermal conductivity and heat capacity of the device's geometry and materials. This equates to a MHz-scale lowpass filter effect in the chirp frequency spectrum. By contrast, refractive index change due to change in carrier density is a smaller effect, but responds according to the laser's relaxation frequency, typically GHz for a VCSEL.

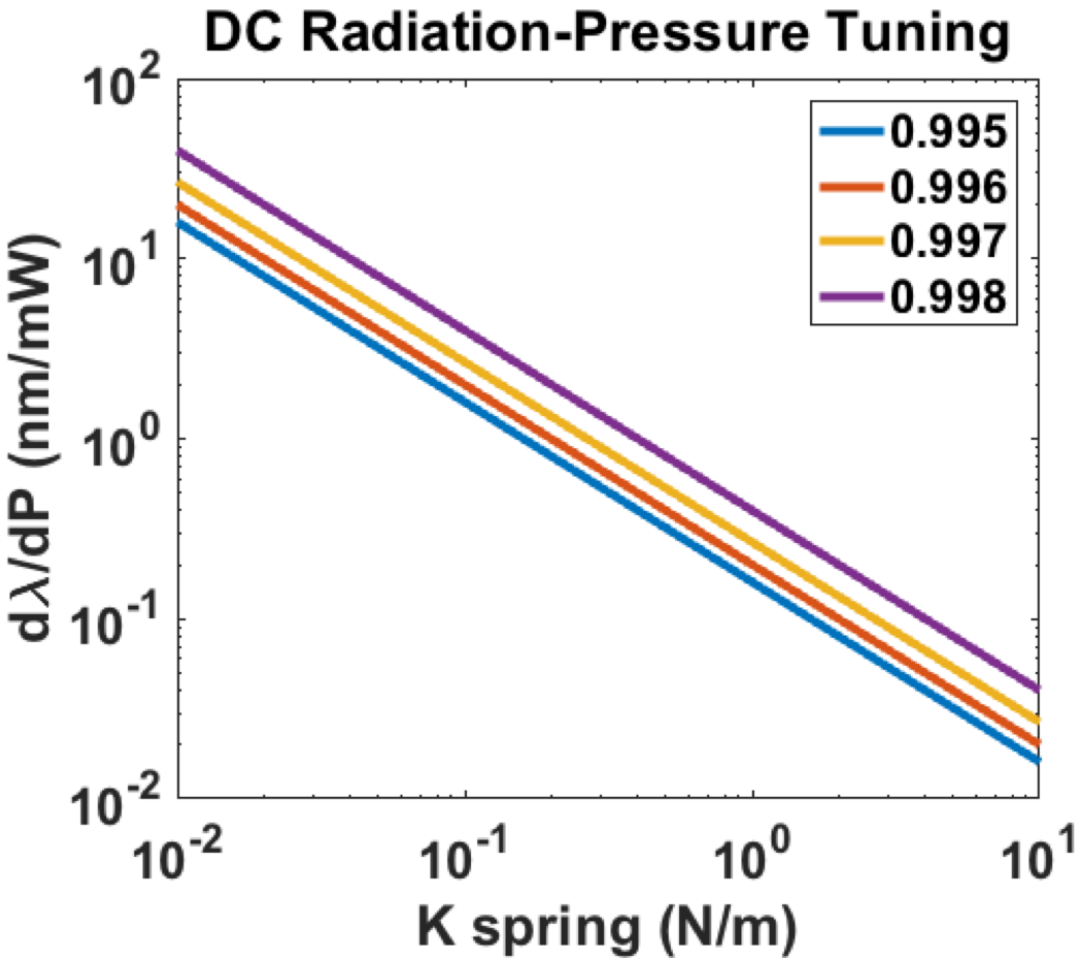

Figure 3.2: Calculation of radiation-pressure-induced laser chirp versus mirror spring constant at various typical top-mirror reflectivites.

In tunable HCG VCSELs, the radiation pressure force would produce a contribution to the chirp mechanisms even at DC. For typical values of mirror reflectivity and spring constant, this effect would be significantly smaller than the other effects, but it can be discerned in the frequency response of chirp. Furthermore, for MEMS modes with quality factor > 0.5, the chirp response due to radiation pressure can be enhanced above the DC value. Previously, experiments by Halbritter et al. used chirp frequency response measurements to identify light-induced forces on the laser mirror as one of the effects contributing to chirp in a tunable VCSEL with a MEMS-tunable DBR mirror. [26]In that device, thermal actuation of the MEMS driven by absorption of light in the DBR proved to be the largest contributor to chirp, while radiation pressure was noted to be approximately an order of magnitude smaller. Though radiation pressure and photothermal actuation could not be discerned in that work, they together dominated thermal effects occurring in the active region.

To more clearly discern the optomechanical contribution to chirp in modulated HCG VCSELs, we measured the frequency response of the chirp of modulated VCSELs both at

room pressure and at 2e-5 Torr, noting substantial changes. Static bias current and tuning voltage were applied with Keithley 2401 source meters, while modulation was applied to either the tuning voltage or drive current using an Agilent E3385 function generator and a bias-tee. Light was captured into an SMF-28 fiber mounted inside the Lakeshore vacuum chamber, and optical spectra were recorded on an Ando AQ-6317 optical spectrum analyzer. The devices under test were ~1080 nm HCG VCSELS in the GaAs-based material system designed and fabricated in the Chang-Hasnain group by Linda Li and Kevin Cook. The frequency range measured is substantially less than the relaxation oscillation frequency of the laser, so the rolloff effects due to laser dynamics can be neglected.

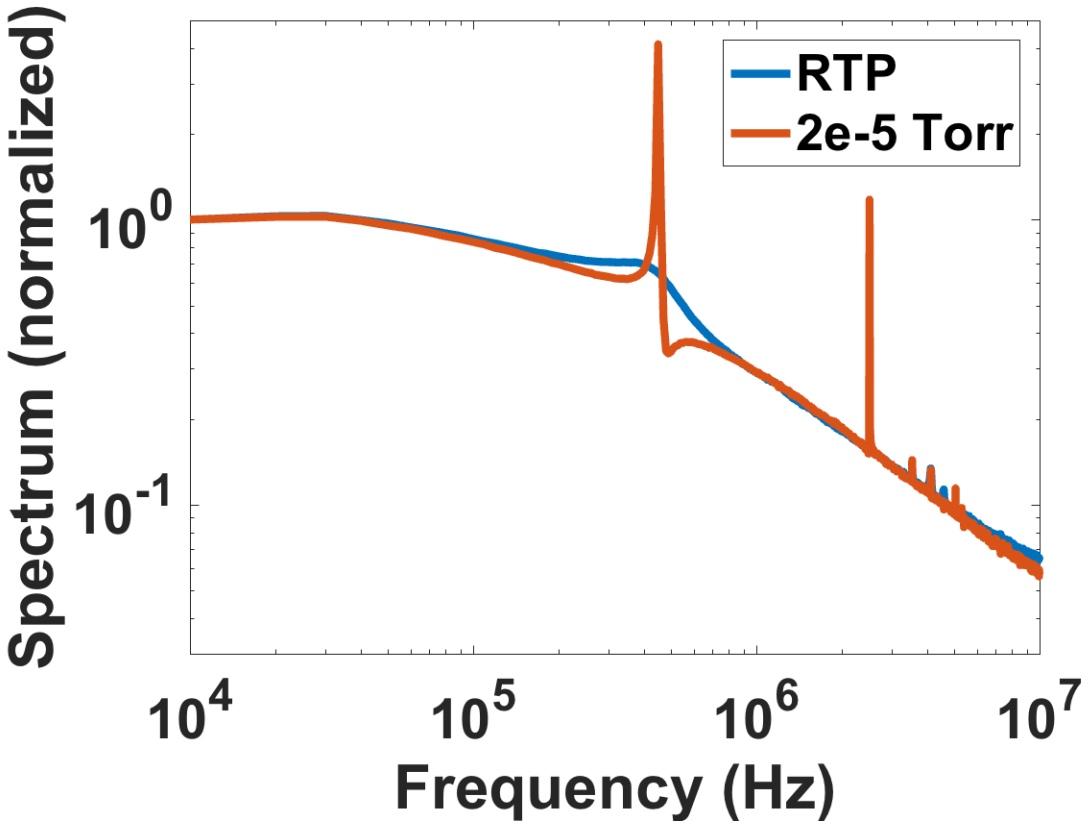

Figure 3.3: Spectral width of VCSEL under drive current modulation vs. frequency, at room pressure and 2e-5 Torr vacuum. Shows notable features of actuation of mechanical modes in both conditions. Decreased linewidth of 450 kHz feature in vacuum further confirms mechanical origin of the effect.

While the room-pressure chirp frequency response reveals subtle indications of radiation-pressure actuation of the HCG mechanical modes, the comparison between the transfer functions of at room pressure and 2e-5 most clearly reveals the effects of radiation-pressure coupling. Out of the effects that contribute to chirp in a VCSEL, self-heating effects would be expected show little change versus air pressure, as the heat outflow of a

VCSEL is overwhelmingly through the lower DBR and substrate and only negligibly through the air.

The common features of the room-pressure and 2e-5 Torr chirp frequency response plots reveal the intrinsic self-heating tuning of the laser. This itself is an object of ongoing research and is notable here for taking a form proportional to $f^{-0.75}$, rather than a one-pole frequency response. The features that deviate from that are notable spikes in the frequency response at certain frequencies. These spikes are best explained as mechanical actuation.

To further corroborate that the observed effect is mechanical excitation of various mechanical modes, we performed finite-element method (FEM) analysis of the HCG-MEMS structure using COMSOL Multiphysics to reveal a diverse variety of mechanical eigenmodes. Many of the eigenfrequencies calculated for the given structure under test match mechanical modes found using finite-element analysis. To the extent that frequencies differ, this can be explained due to residual PMMA e-beam resist found on the grating after processing, which alters the mechanical modes of the HCG but not the optical properties. A fine scan of spectrum vs. frequency revealed the high-order modes at 3.55 MHz and 4.13 MHz in greater detail. Like the fundamental mode, these modes also decrease noticeably in linewidth (increased effective Q_m) in vacuum. The closeness of these modes reflects the drum-like mechanical modes spacing noted previously in small, freestanding HCGs.

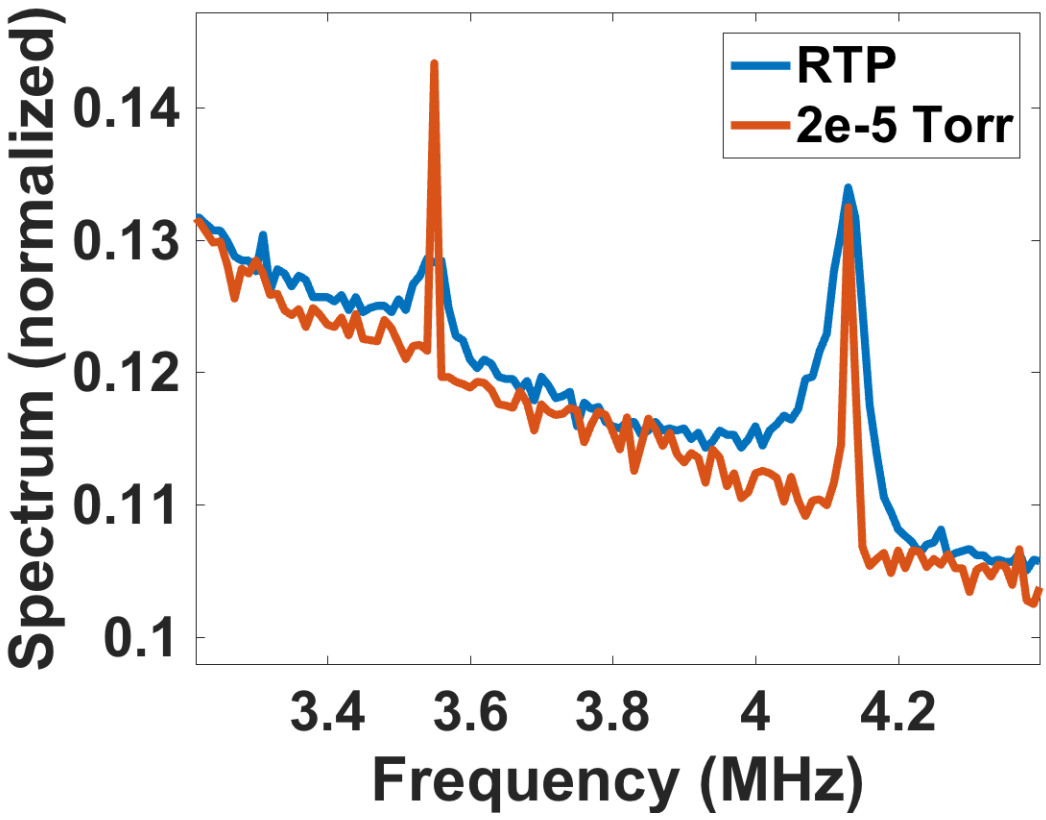

Figure 3.4 Fine scan spectrum vs. drive current (I_d) modulation frequency showing two distinct high-order modes with decreasing linewidth from air to vacuum.

For comparison, a frequency response of electrostatic tuning was captured for the same device at room pressure and at 2e-5 Torr. This showed mechanical modes at similar frequencies and quality factors to those noted in the current modulation for most modes. However, certain modes were notably absent in tuning modulation, indicating that those modes were actuated more efficiently by radiation pressure than electrostatics. Qualitatively, the FEM-derived mode shapes explain the difficulty of actuating higher-order mechanical modes with capacitative actuation. Since electrostatic actuation force results from a change in capacitance with respect to the generalized position coordinate of the mode being actuated, the dC/dx of the higher-order modes is reduced given that parts of the mirror are moving in opposing directions. By contrast, the ability of the mode to be excited by radiation pressure drive results from the overlap integral of the comparably small mode spot and the mechanical mode.

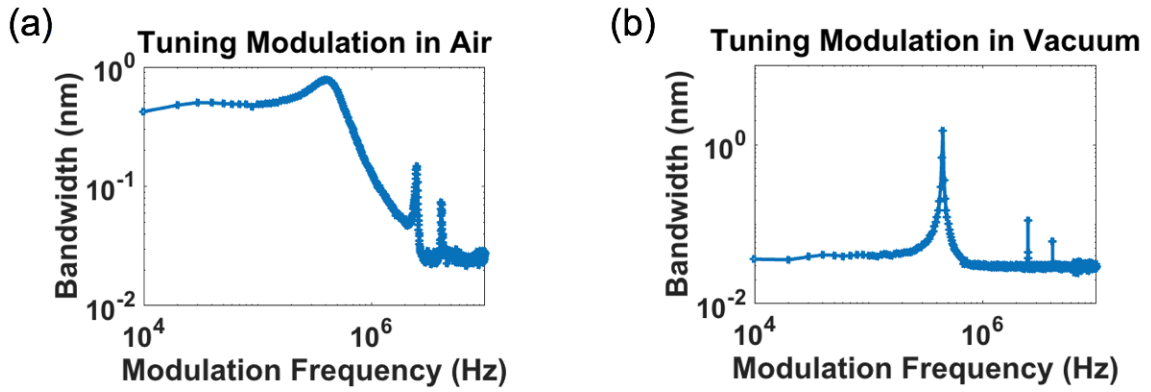

Figure 3.5: Spectral width of VCSEL vs. MEMS tuning voltage V_t modulation frequency (a) in air and (b) in 2e-5 Torr vacuum. Each condition illustrates actuation of both fundamental mode (450 kHz) and higher-order modes (2.5 MHz, 4.1 MHz). A notable increase in effective mechanical quality factor is seen for the fundamental mode.

At the peak frequency of Figure 3.3, the spectrum of the laser shows 10 nm of wavelength swept range using only current modulation. As the decaying power of the spectrum on the short-wavelength side indicates, the laser is mechanically tuning into the regime where decaying mirror reflectivity and quantum well gain increase lasing the lasing threshold to beyond the chosen DC bias current. This illustrates the ability of radiation pressure to produce broad-swept two-terminal laser devices that do not need electrostatic actuation.

3.4 Optomechanical Feedback under Modulation

In the previous section's results, optomechanical forces are observed to actuate multiple mechanical modes of the HCG under direct current modulation, a straightforward result of the power-dependent force of radiation pressure. For large-signal tuning modulation

sweeps in vacuum, we further observed that the resulting transfer function (bandwidth vs. frequency) deviated significantly from the expected second-order lowpass response expected for underdamped harmonic oscillators. Notably, the frequency response in vacuum showed a flat-top shape and hysteresis between increasing-frequency and decreasing-frequency sweeps. Hysteresis cannot be described by linear time invariant (LTI) models of a system, illustrating that a memory effect was occurring in the VCSELs.

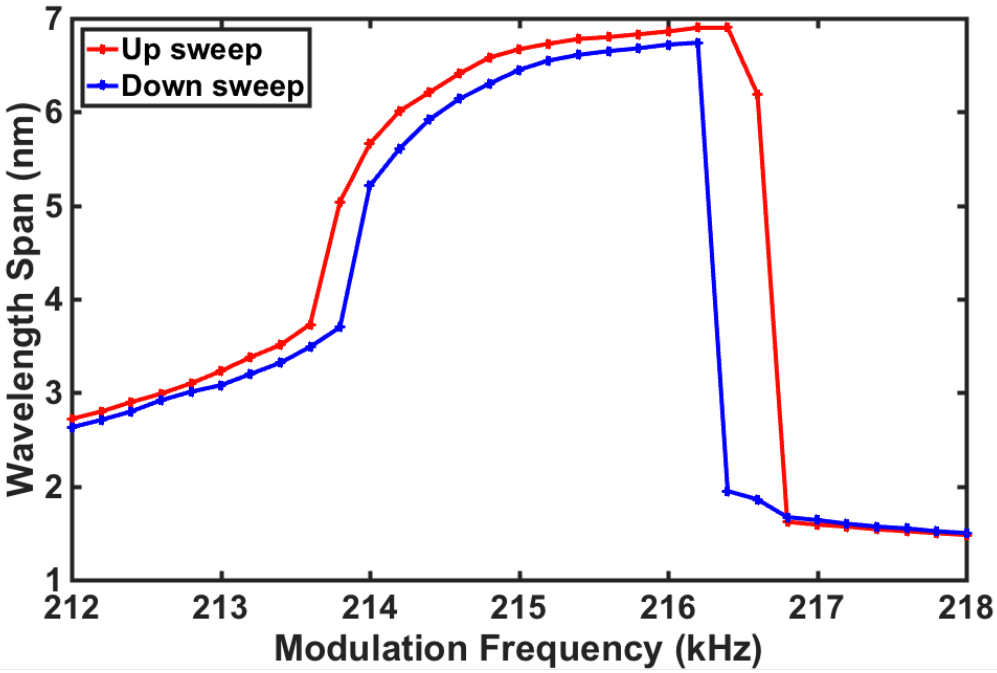

Figure 3.6: Wavelength span vs. V_t modulation frequency for up and down frequency sweep showing hysteresis and non-Lorentzian frequency response.

As shown in Figure 3.6, the frequency response shows notable hysteresis and a shape significantly different from the standard second-order lowpass shape of an underdamped harmonic oscillator. On the contrary, the frequency response reveals two distinct states of large-oscillation and small-oscillation, and a latching effect between the two. This surprising result had some parallels in both the mechanical and optomechanical literature. Such hysteresis occurs due to mechanical spring loosening in purely mechanical system, wherein the large oscillation amplitude changes the effective spring constant k_{eff} and moves the effective resonance frequency ω_m depending on oscillation amplitude $x_0 \sin(\omega_{mod} t)$. Such hysteresis is also a notable effect of optomechanical antidamping near the self-oscillation threshold [34]. In optomechanical cavities, latching appears when modulation enables the mirror to achieve a cycle in which the net optomechanical work is positive, even if the optomechanical antidamping at steady-state is insufficient to cause instability.

Without the ability to turn off the laser light and directly measure the mirror oscillation amplitude *in situ*, this data alone could not differentiate whether the hysteresis effect was

due to purely mechanical effects or optomechanical effects. Nonetheless, it strongly suggested that further VCSEL testing in vacuum could reveal optomechanical self-oscillation. Accordingly, we developed the characterization methods described in Section 3.5 to capture evidence of self-oscillation.

3.5 Overview of Optical Characterization Methods for Self-Oscillation

3.5.1 Introduction and Motivation

While the previously discussed results demonstrated the action of radiation pressure on the HCG mirror under I_d or V_t modulation, they did not touch upon self-oscillation phenomena that occur under steady-state conditions, without external modulation, and produce a range of changes in the light output. Accordingly, characterizing that light output provided the first view into the self-oscillation behavior occurring in the device. In the following sections, we will overview those optical characterization methods, then present the results of specific experiments showing self-oscillation in multiple mechanical modes, leading towards the observation of large-sweep self-oscillation in the fundamental mode.

3.5.2 Static Spectrum Characterization

In all forms of vacuum testing, a chip of lasers under test was subjected to vacuum conditions down to 2e-5 Torr in the Lakeshore cryogenic stage. Light was captured into a probe-mounted SMF-28 fiber built into the Lakeshore stage, and output light measured with an OZ Optics POM-300-IR handheld power meter or characterized using an Ando AQ-6317 spectrum analyzer. DC current and tuning voltage were applied with Keithley 2400-series SMUs.

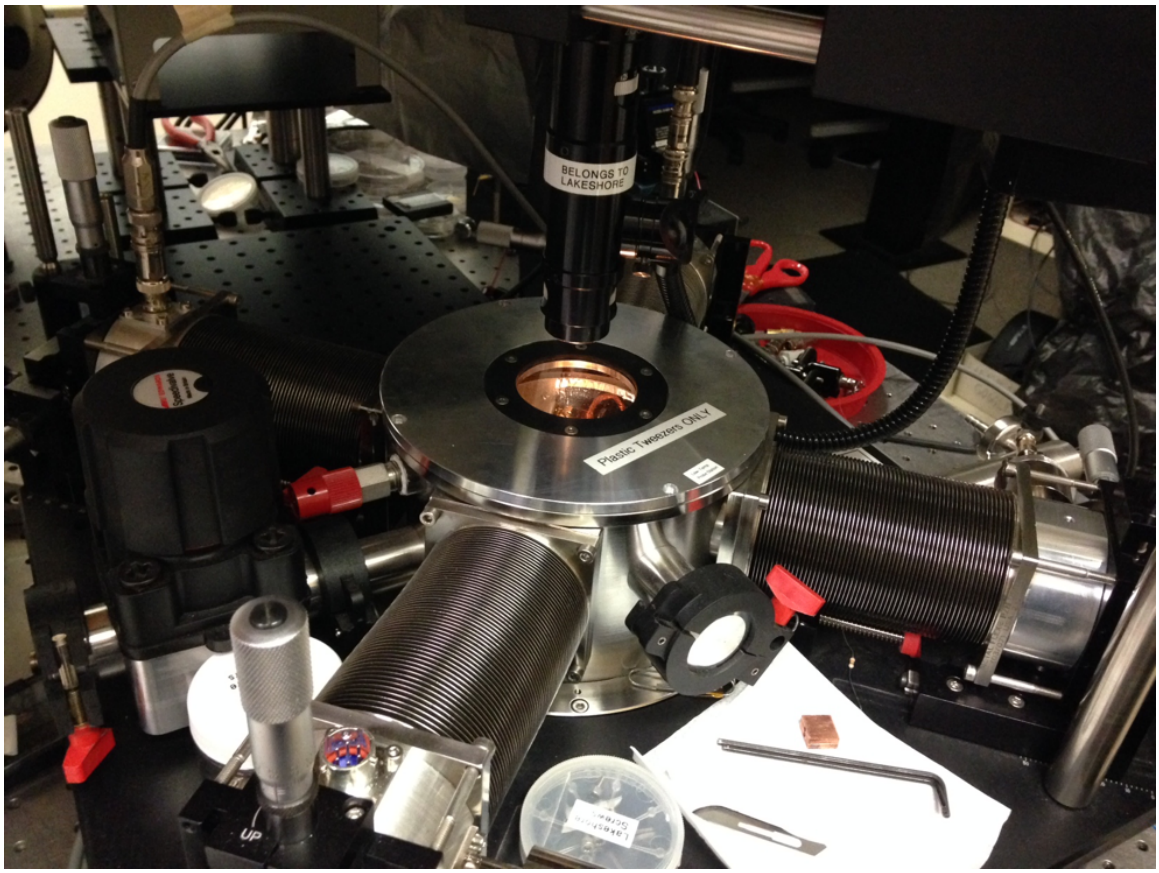

Figure 3.7: Lakeshore vacuum and cryogenic probe station at Cory Hall, UC Berkeley

Under steady-state (DC) input current and tuning voltage conditions in vacuum, certain devices exhibited spectra fundamentally unlike any seen from a steady-stated-driven VCSEL before. While HCG-tunable VCSELs normally produce single- or few-mode light with sub-picometer (< 100 MHz) linewidths, far smaller than the Angstrom-scale wavelength resolution of commercial spectrum analyzers, HCG VCSELs at high vacuum showed spontaneous spectral broadening to nanometer-scale bandwidths. At varying DC input conditions of drive current and tuning voltage, both the qualitative shape of the output optical spectrum and the optical bandwidth of the output light changed, including conditions at which the spectrum returned to its unbroadened state. This gave early indication that the broadening was due to a reversible, non-damaging change in laser state. Furthermore, the lack of drop in total output power laser likewise indicated that the device remained in a comparable lasing condition during its broadened and unbroadened states. These observations invited further characterization of the time and RF frequency phenomena involved.

3.5.3 Amplitude characterization, time-domain and RF spectrum

Measuring the amplitude of the light in time-domain with a packaged, biased, high-speed photodetector (Thorlabs DET01CFC) monitored by an Agilent 500 MHz oscilloscope revealed self-amplitude modulation notably corresponding to the mechanical frequency of the laser's MEMS structure. This self-amplitude modulation strongly suggested that

the laser spectrum was broadened due to time-domain wavelength sweeping synchronously with the self-amplitude sweep, thus necessitating a means to characterize the optical spectrum with time resolution.

Time-Resolved Spectrum Analysis

To capture a full spectrum versus time, we exploited the repetitive nature of the self-amplitude and self-wavelength modulated light to construct optical spectrograms using what we termed time-resolved spectrum analysis (TRSA). In this technique, laser light is passed through a fiber-based monochromator (HP OSA in monochromator mode), captured by a DET01CFC photodetector, and recorded by a 500 MHz Agilent oscilloscope. To trigger the oscilloscope, a separate path of light is split off using a 90:10 fiber splitter and captured in an equivalent detector. To overcome the quantization limits of the oscilloscope while maintaining time synchronization between the two signals, both electrical signals were amplified using a Comlinear CLC-100 DC-500 MHz amplifier with 20 dB gain. By changing the center wavelength of the HP OSA monochromator after each captured trace and synchronizing multiple electrical traces using the time-invariant amplitude signal, we were able to compile optical spectrograms of the wavelength-modulated light. In separate later work, we have also used this technique to capture intentionally wavelength-swept light by synchronizing the oscilloscope from the modulation signal.

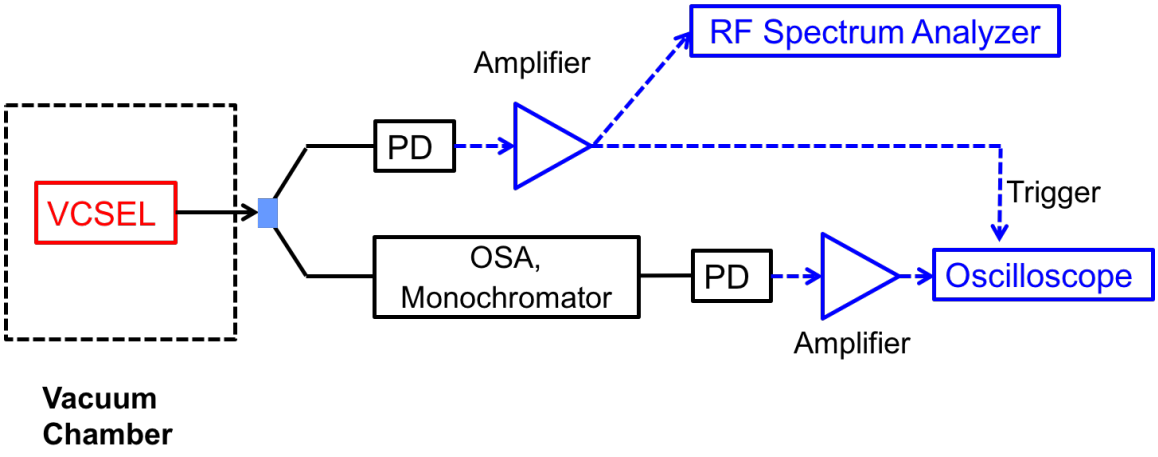

Figure 3.8: Schematic of Time-Resolved Spectrum Analysis (TRSA) characterization system, shown with optional RF spectrum analysis

3.6 Multi-Method Characterization of Self-Oscillation

Self-oscillation initially presented in VCSELs as a spontaneous broadening of the VCSEL emission linewidth from < 0.01 nm to > 1 nm when lasing in vacuum. Such behavior was immediately interesting but of unclear origin, so to obtain the clearest possible picture of optomechanical self-oscillation in vacuum, we simultaneously performed optical spectrum, time domain amplitude, and RF-domain spectrum for a self-

oscillating VCSEL. A tunable TM-HCG, lasing near 1570 nm, was characterized in 3e-5 Torr vacuum at room temperature in the following experiments.

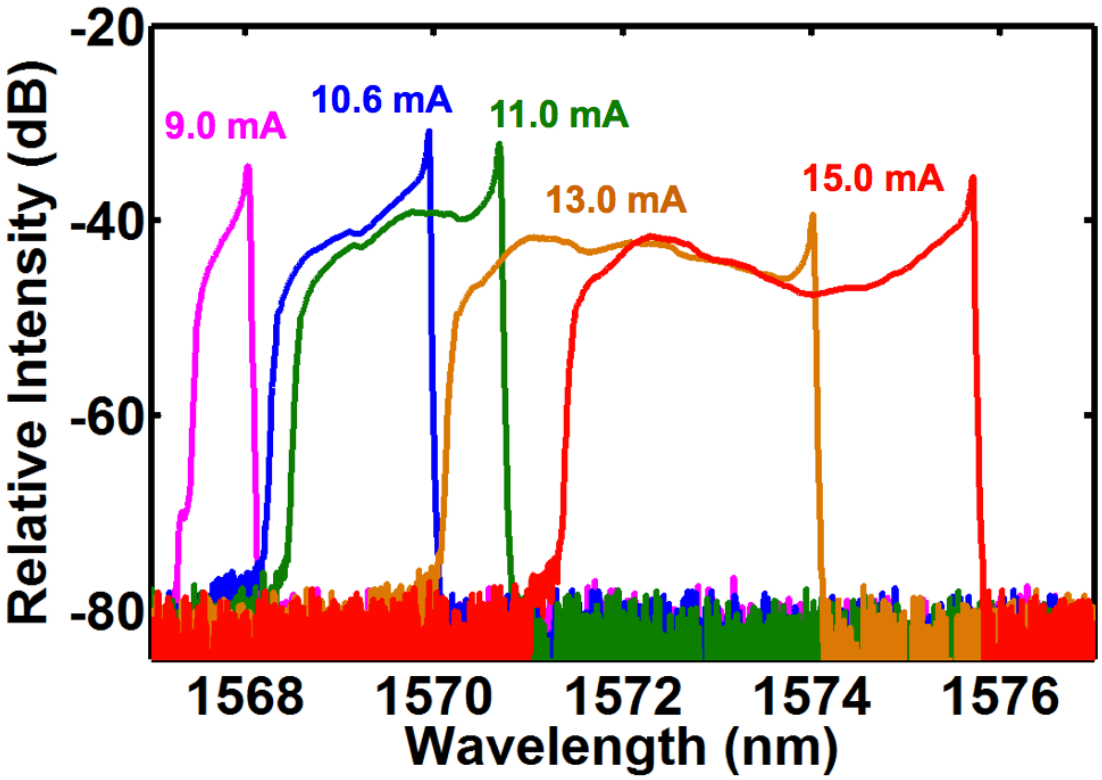

Figure 3.9: VCSEL optical spectra at varying currents showing spectral broadening due to self-oscillation.

Above its lasing threshold, the laser exhibited a broadened spectrum with a distinctive red-peaked shape. With increasing current, this spectral shape both redshifted, as expected by self-heating, and broadened.

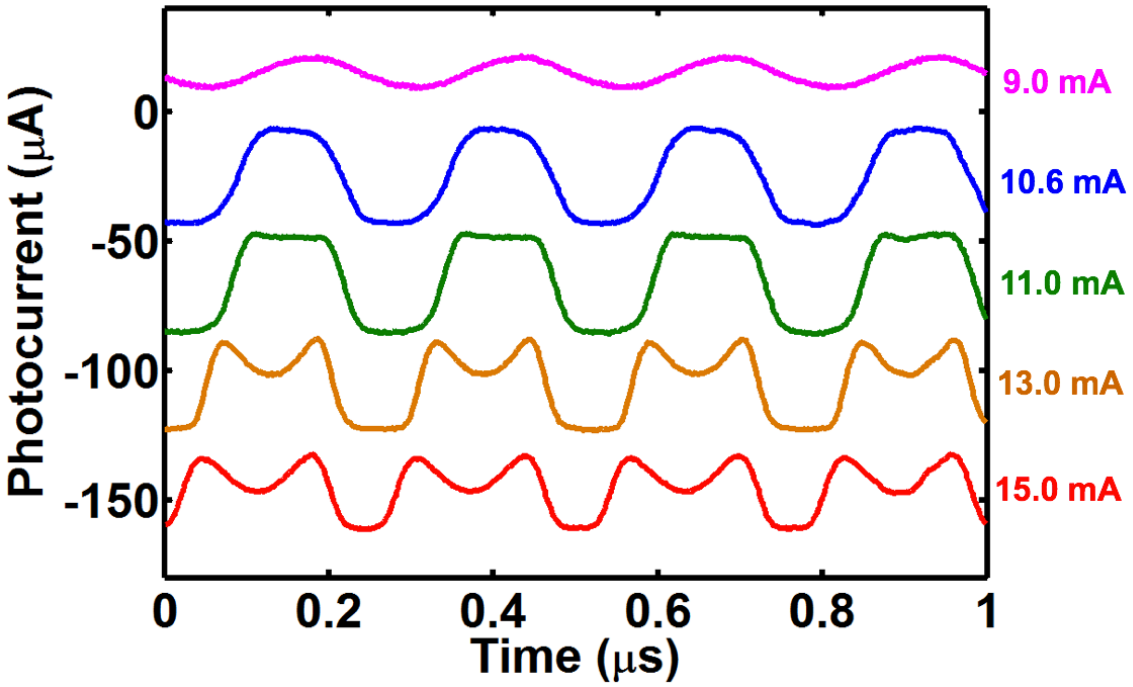

Figure 3.10: Time-domain optical power for same values of drive current used in spectrum characterization above

Time-domain amplitude data noted a somewhat constant fundamental frequency around 3.8 MHz for the self-oscillation behavior, but the changing envelope shape of the amplitude vs. time provided insight into the spectra. For the lowest-current spectrum (9 mA), the high-power phase of the oscillation clearly coincides with the high-power (blue) side of the spectrum. With increasing current, the amplitude vs. time creates a flat-top in the high-power (blue) side, but as the spectrum tends towards a two-peaked (typical sinusoidal) shape, the blue-side power is seen to drop off vs. time.

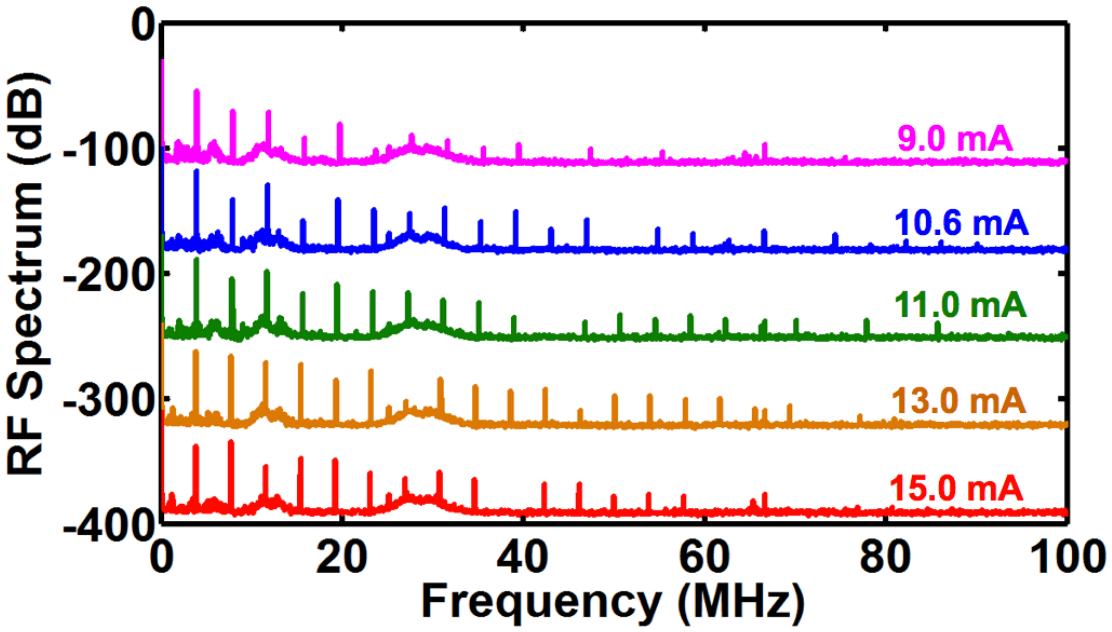

Figure 3.11: Staggered RF spectra of optical power at various drive currents

To corroborate the oscilloscope measurement with more frequency-domain precision and better noise sensitivity, we also obtained RF spectra of the light at the same current values. These broadband (100 MHz), mid-resolution (1 kHz RBW) spectra corroborated the 3.9 MHz center frequency of the oscillation at all current values, indicating that the mechanical mode in question did not experience substantial spring-stiffening due to increasing optical power circulating in the cavity. Likewise corroborating the oscilloscope data, increasing current values showed higher powers in the second harmonic (approximately 8 MHz), owing to the increased double-bump time-domain profile. Lastly, the RF spectra noted the power in high-frequency components, noticeable out to 85 MHz.

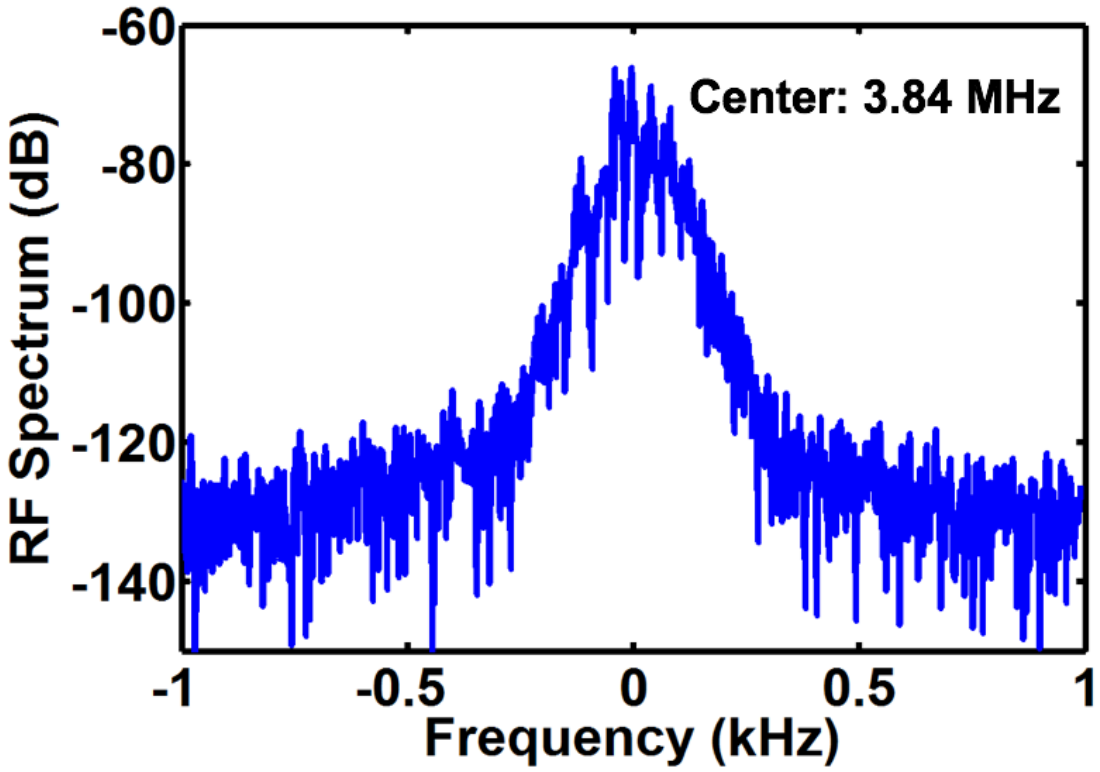

Figure 3.12: Zoomed-in RF spectrum of first peak, centered at 3.84 MHz, under I_d = 15 mA. Resolution and video bandwidth 3 Hz.

High-resolution RF spectrum at I_d = 15 mA, captured with a 3 Hz RBW, show an RF linewidth of 120 Hz. Since the signal offset by 1 kHz is observed to be at the experiment noise floor, the single-sideband phase noise performance can only bounded as > -60 dBc/Hz at 10 kHz offset, requiring higher capture efficiency or lower-noise photodetector to provide this important metric. Lastly, time-resolved spectrum analysis at 15 mA connect the spectra and time-domain data. TRSA data confirms that the laser turns itself off at the blue side of the sweep but remains on at the red side, leading to the noticeably pointed spectrum on the red side. The comparatively lower power of the laser in around 1575 nm matches well with optical spectra recorded for the same device in and condition in Figure 3.9.

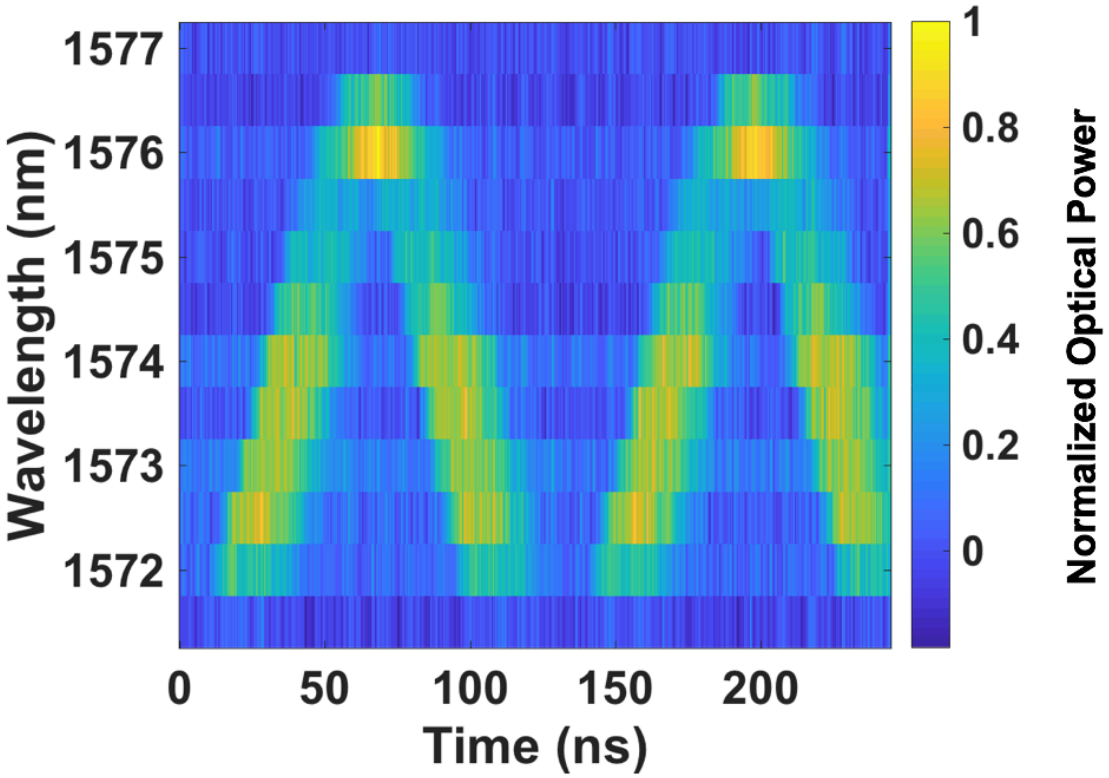

Figure 3.13: Spectrogram of self-oscillation obtained by time-resolved spectrum analysis (TRSA). Shows two periods of self-oscillation sweep.

Altogether, these data begin to paint the picture of the kind of mechanical mode responsible for this self-oscillation. In addition to its frequency of 3.8 MHz, the mechanical mode appears to have a large change in reflectivity versus wavelength and an asymmetrical effect on reflectivity vs position. Both the high frequency and degradation of reflectivity indicate a mode that involves substantial deformation of the HCG.

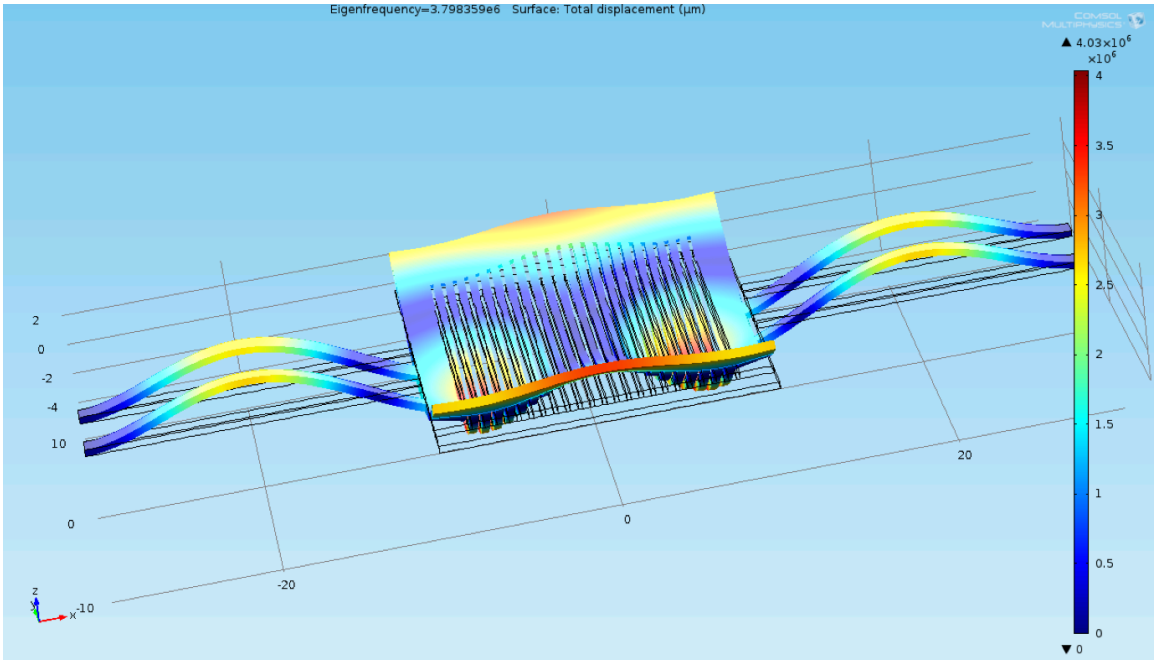

Figure 3.14: Eigenmode of as-fabricated MEMS HCG for device used in all experiments in Section 3.6, obtained using COMSOL finite-element method, for 3.8 MHz.

To better understand the physical shape of the mode, we applied finite-element analysis using COMSOL Multiphysics to the as-designed HCG structure for the specific device. Disregarding damping mechanisms, COMSOL identified a possible mode at 3.8 MHz that bore the necessary qualitative features to be a candidate mode. As shown in Figure 3.14, this mode included substantial deformation of both the HCG frame/bar and the supporting bridge, whereas most other modes are predominantly bridge-modes or bar-modes. This hybrid nature explains the intermediate frequency of this mode, between the 100 KHz – 800 KHz range of the fundamental (bridge) mode in most HCG VCSELs and the >5 MHz frequency scale of the bar modes. Secondly, the existence of a vibrational antinode at the center of the HCG confirms that vertical radiation pressure from the optical mode could actuate this mechanical mode. Lastly, as discussed elsewhere, the convexity of the mirror when deformed down (blue) by this mode would damage lateral confinement of the mode, introducing scattering losses and contributing to the blue-side turnoff of the laser during self-oscillation.

3.7 Characterization of Large-Sweep Optomechanical Self-Oscillation

3.7.1 Search for Large-Sweep Conditions

Achieving a large self-wavelength modulation with VCSEL optomechanics would both provide substantial physical insight into the mechanism and unlock numerous practical applications for the technique, as discussed later. Given the substantial degradation of mirror quality vs. position seen in higher-order modes that deform the bars, maximizing wavelength swept range requires exciting the fundamental, bridge-only mode.

Accordingly, a substantial search was undertaken to identify the devices and experimental conditions that produce self-oscillation in their fundamental mode. Unfortunately, self-oscillation in higher-order modes was found to occur in a far greater set of devices and experimental conditions than in the fundamental mode. Intuitively, this is supported by the very high dR/dx of these modes, which leads to correspondingly higher optomechanical anti-damping than in the fundamental modes.

While fundamental-mode self-oscillation has been observed in TM-HCG 1550 nm, TE-HCG 1550 nm, 850 nm, and 1060 nm devices, the largest self-oscillation sweeps were observed in various TE-HCG 1550 nm devices. In many such TE devices, oscillation in either the fundamental or a higher-order mode were observed depending on I_d and V_t, but one such device was observed that produced only fundamental-mode self-oscillation across a wide range of I_d and V_t conditions. Characterizing both optical spectrum and RF spectrum across this sweep both revealed a very large wavelength sweep and substantial insight into the mechanism of self-oscillation.

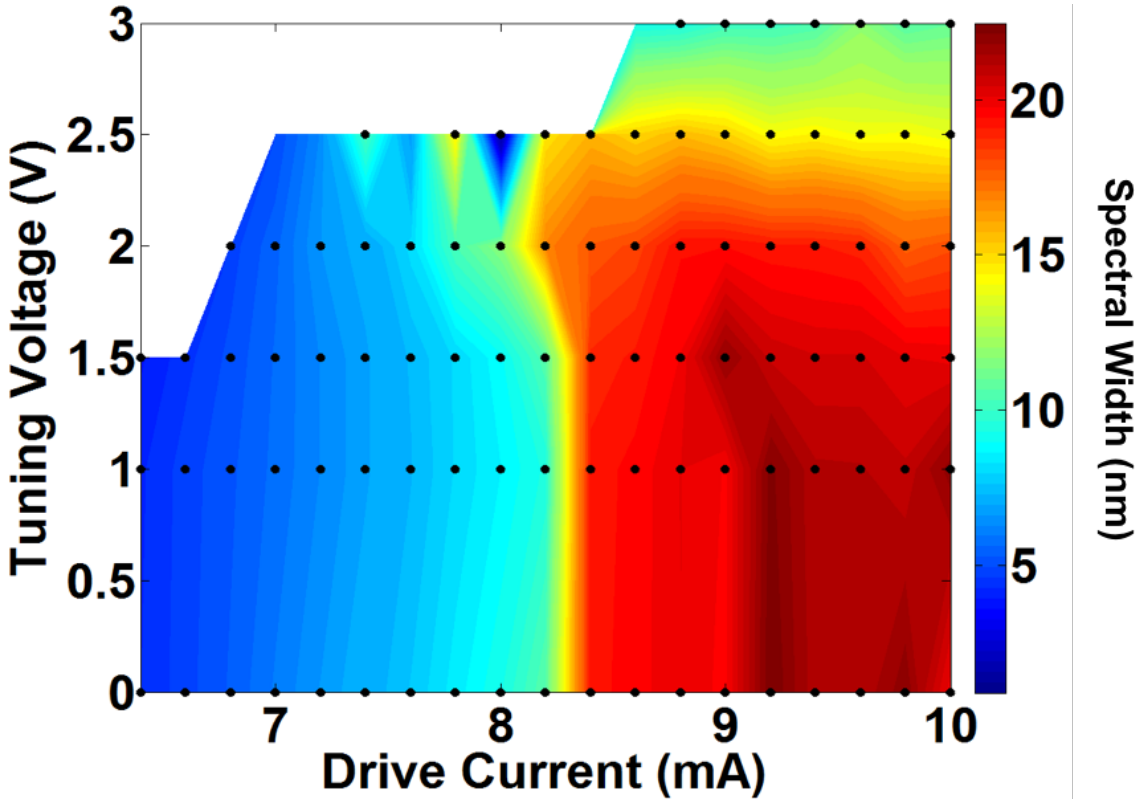

Figure 3.15: Self-oscillation spectrum width vs. DC drive current and tuning voltage conditions for VCSEL in 2e-5 Torr vacuum.

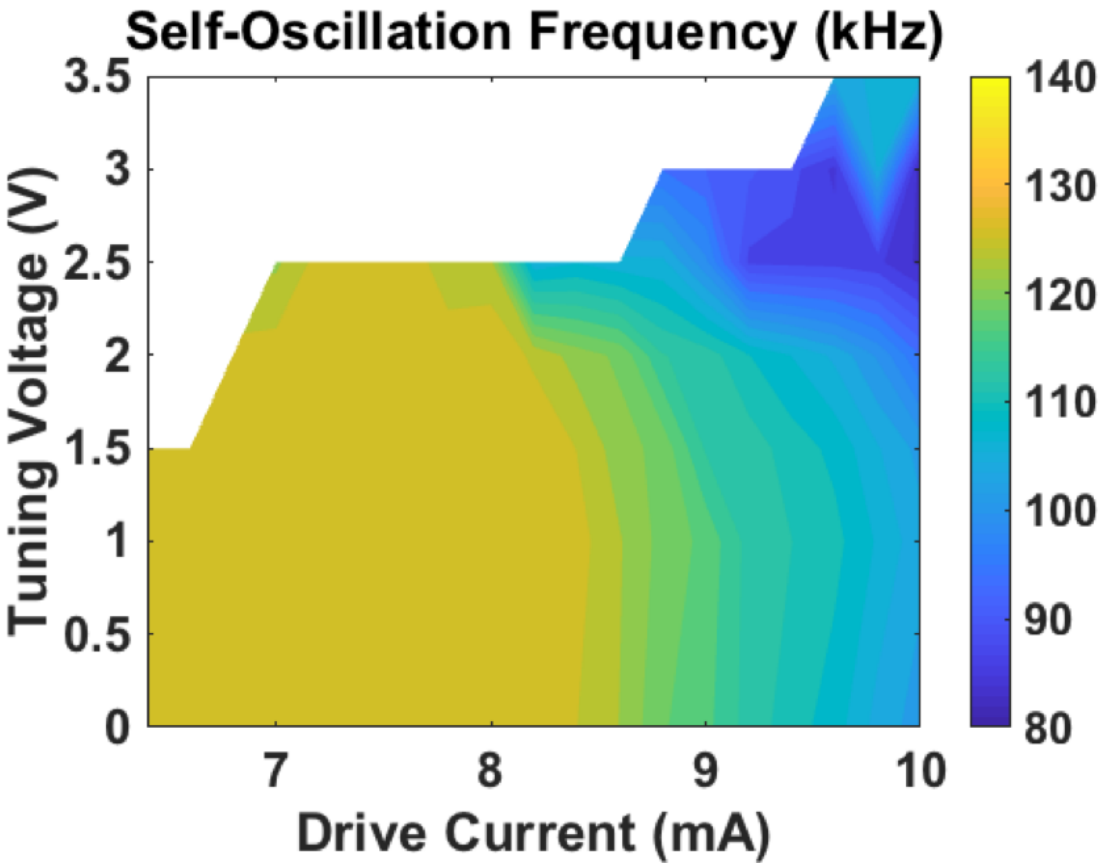

Figure 3.16: Fundamental frequency of self-oscillation derived from RF spectrum, versus tuning voltage and current, in comparable conditions to Figure 3.15

Spectral broadening due to self-oscillation was observed immediately above the device's lasing threshold of 6.3 mA, and sustained up to 10 mA. Due to the combined effects of both thermal tuning and mechanical tuning, the laser emission is most redshifted in the lower-right corner of the chart (low V_t and high I_d and most blueshifted in the upper-left corner of the graph. Accordingly, the device is observed to produce the widest wavelength sweep of >20 nm in the reddest condition, and to cease self-oscillating (though lasing is still observed) in the bluest conditions. Simultaneously, RF spectrum analysis shows clearly that the device is self-oscillating in its fundamental mode, with a frequency around 126 kHz for most low-drive-current conditions. With increasing drive current and tuning voltage, the self-oscillation frequency notably drops as low as 81 kHz. The smooth transition, and the fact that the frequency only decreases, clearly indicate that the fundamental mechanical mode is self-oscillating in all conditions. This dataset can therefore be used to analyze the conditions needed to produce large-sweep self-oscillation of the fundamental mode. Furthermore, this large wavelength sweep provided the first indication of the technological applications of VCSEL self-oscillation in ranging and imaging[35].

As discussed later, predicting the final stable amplitude of self-oscillation is a complex nonlinear problem, but it intuitively relates to the range of positions over which there is

locally more anti-damping than damping. RCWA simulations revealed the peak reflectivity for this laser's HCG design to be around 1550 nm and to follow a parabolic profile for the high-reflectivity regime. This confirms that redshifting the laser away from 1550 nm provides increased optomechanical gain due to increased radiation pressure gradient, dF/dx, and that blueshifting the laser compresses swept range by bumping against the peak-reflectivity limit, past which the mirror experiences added optomechanical damping. It is important to note again here that redshifting from peak reflectivity produces optomechanical anti-damping and blueshifting produces damping, which is reversed from passive cavity optomechanics.

3.7.2 Time-Resolved Spectrum Analysis of Largest Oscillation Amplitude

Very large-amplitude self-oscillation was repeatably observed in multiple TM-1550 nm devices with designs similar to those in the previous section on multi-method characterization. After searching comparable devices, the largest wavelength-swept range observed due to self-oscillation was found to be 23.25 nm, observed in the Lakeshore stage at room temperature and a pressure of 2e-5 Torr. Static and time-resolved spectra of this condition provided further insight into the mechanism of large-swept oscillation, which will be discussed in detail in the analysis section.

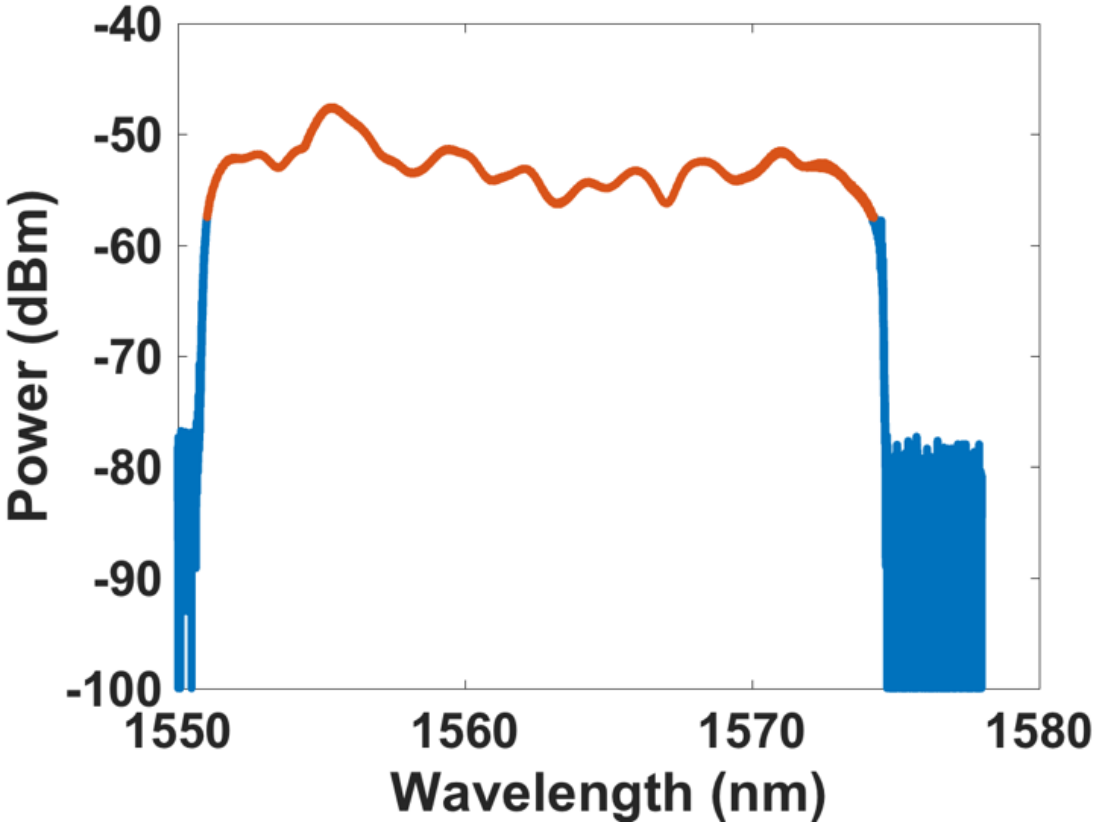

Figure 3.17: Static spectrum of hero self-oscillation, showing 23.25 nm range with < 10 dB ripple, shown in orange.

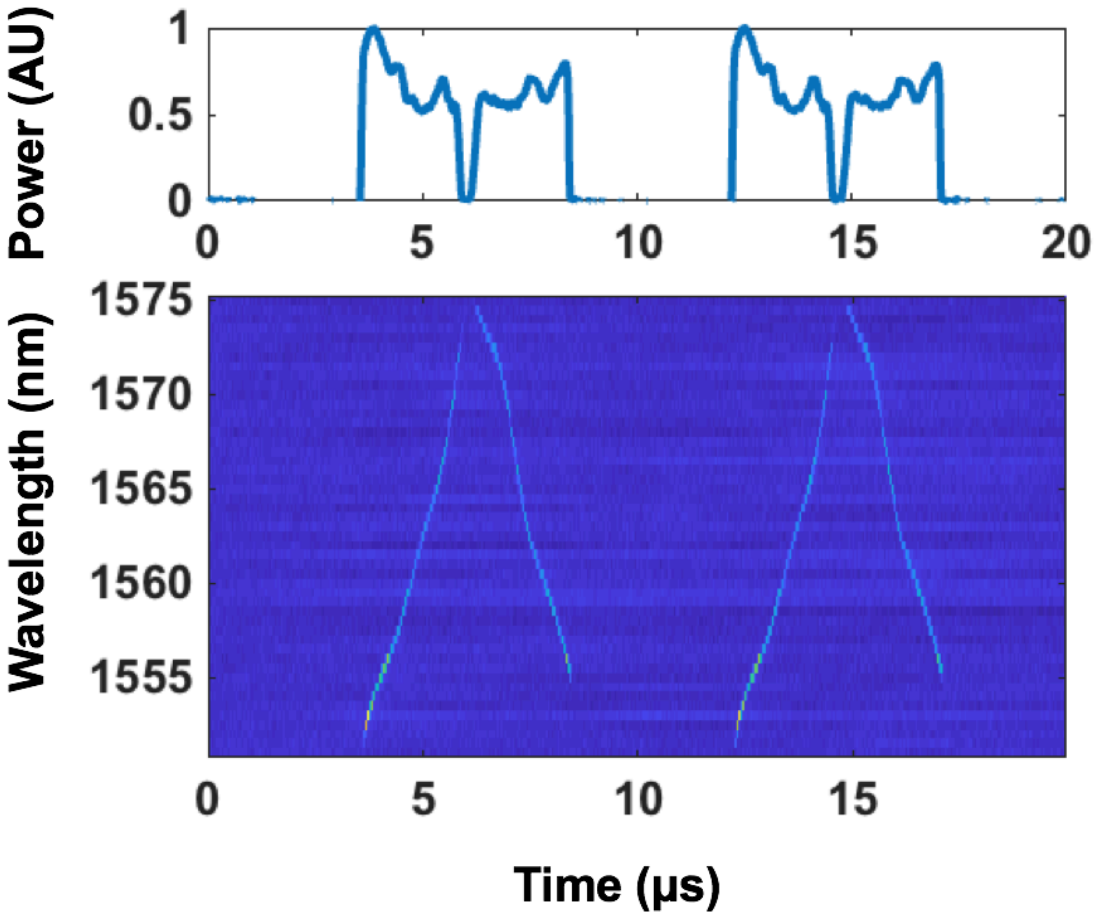

Figure 3.18: Spectrogram of 23.25 nm self-oscillation obtained through TRSA with accompanying optical power vs. time (normalized) used for synchronization.

The static spectrum reveals an impressive 23.25 nm swept range over which the power spectrum exhibits ripples of < 10 dB, as highlighted orange in the spectrum. This ability to sweep throughout the full lasing range of the VCSEL necessitated further characterization by time-resolved spectrum analysis, as shown in Figure 3.18. Using the measurement technique described previously, TRSA traces were taken over a wavelength range of 1551 nm to 1575 nm in 0.5 nm increments using a monochromator passband of 0.5 nm. Over the course of the hour required to capture this data, the overall amplitude vs. time trace remained constant, confirming the impressive stability of the self-oscillation and allowing the data to form a single detailed spectrogram to supplement previously recorded static spectra. At both the red and blue ends of the spectrum, the laser is observed to turn itself off, for a substantially larger duration of time on the blue side. This corroborates the flat-topped static spectrum, which would typically display peaks at the red and blue sides if the laser remained lasing throughout the sweep. Secondly, the 8 μsec repetition rate of the pattern confirms self-oscillation in the 125-kHz fundamental mode. Likewise, the fairly constant sweep rate $d\lambda/dt$ observed in the triangle-wave-like spectrogram helps further explain the uniformity of the spectrum, which lacks the curved-

top distortion evident in a more sinusoidal $\lambda(t)$. Furthermore, the spectrogram reveals subtle differences between the up and down sweep of the laser, particularly in that the laser turns of on the down-sweep a higher wavelength than that at which it turns on. This feature provides important qualitative insight into the mechanism for providing positive work on the mechanical mode throughout the whole cycle. Since laser power correlates with upwards force, a higher laser power on the upswing than the downswing indicates that radiation pressure performs more positive work on the mirror in the upswing than it does in the downswing.

3.8 Oscillation of Multiple Mechanical Modes

While the MEMS fundamental mode enables large-sweep self-oscillation, higher-order modes provide the richest space in which to explore varied self-oscillation behavior. As noted by Kemiktarak *et al.* and FEM simulations including Figure 3.14, HCGs have multiple mechanical modes with mode profiles and frequencies analogous to the drum-like modes of a similarly-shaped solid plate[23]. While these higher-order modes are poorly actuated by electrostatics (and only observed electrostatically for the first time in this work), the high $\frac{\partial R}{\partial x}$ of these modes make higher-order self-oscillation more readily observed in most VCSELs than in the fundamental mode. In certain instances, self-oscillation was able to be controllably initiated in different mechanical modes for different DC input conditions. This effect is the mechanical analogue to mode competition and mode transitions in multi-optical-mode lasers. Below, we show different mechanical modes of the HCG of a 1550 nm TM-VCSEL oscillation at I_d = 12.6 mA and 13 mA.

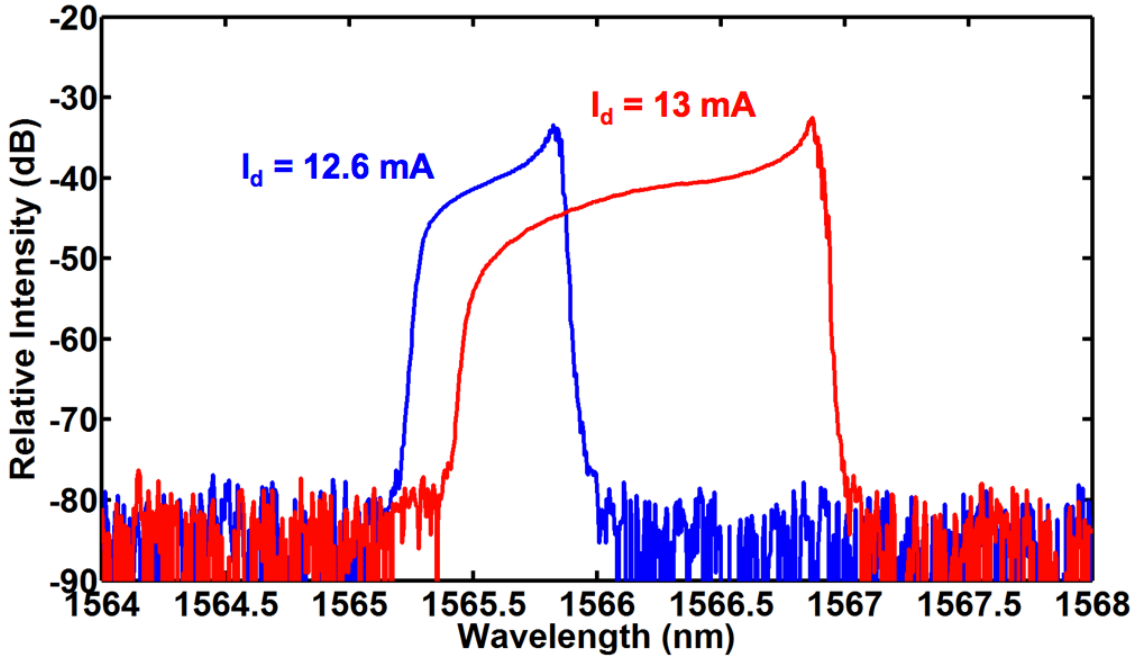

Figure 3.19: Self-oscillation spectra of the same device at two current conditions with different mechanical modes self-oscillating.

Optical spectra between the two modes showed a qualitative similarity with each other and with many other higher-order modes, notably an asymmetrical spectrum with greatly decreasing optical power on the short-wavelength (blue) end of the spectrum. As described elsewhere in the thesis, this commonality is consistent with an explanation that a convex HCG mirror breaks cavity lateral confinement by reflecting the beam into an expanding pattern, similar to the cavity instability found in macroscopic lasers with flat or convex mirrors.

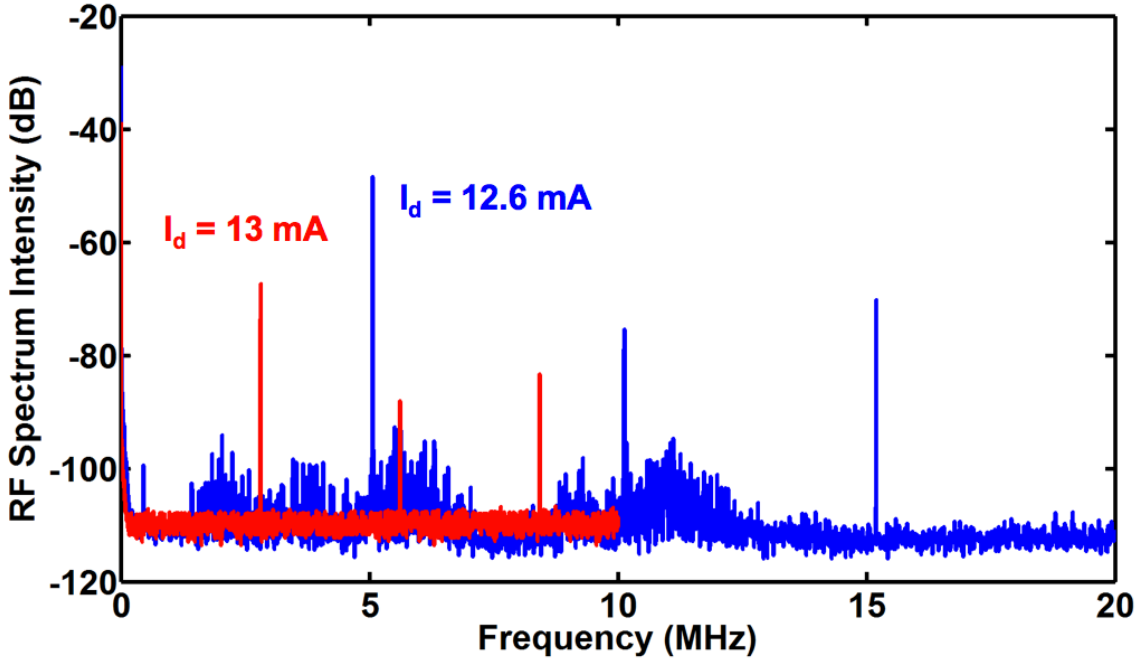

Figure 3.20: RF spectra of self-oscillation of two modes at 2.81 MHz and 5.06 MHz

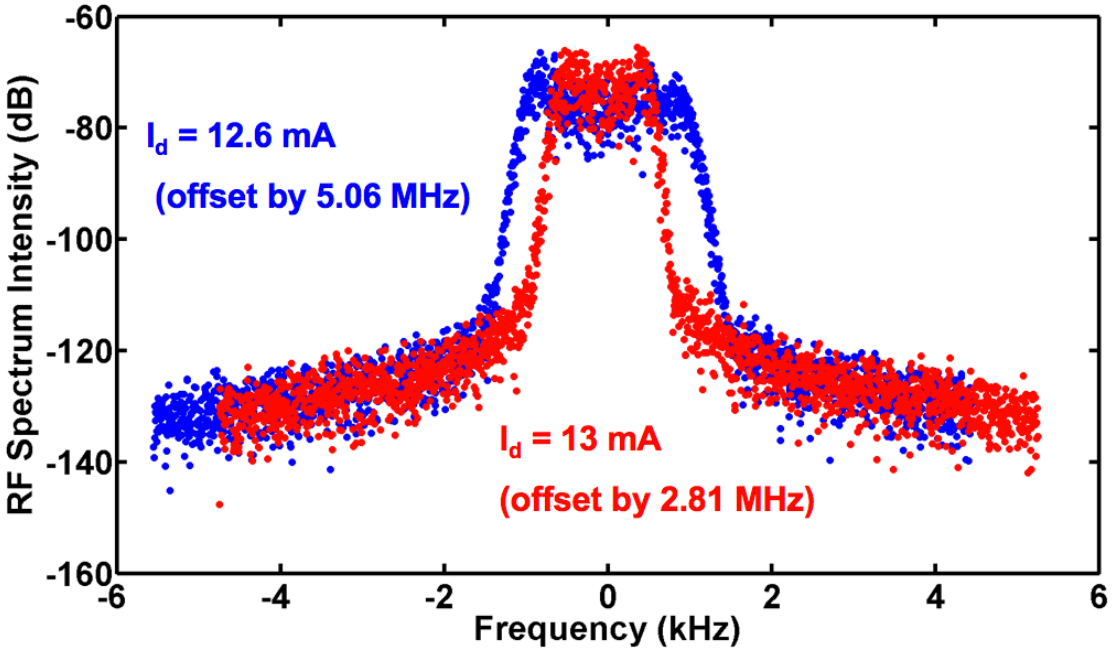

Figure 3.21: Zoomed RF spectra of self-oscillation of two mechanical modes, showing linewidths of 1.1 kHz and 1.7 kHz for 2.81 MHz and 5.06 MHz, respectively.

RF spectra of light amplitude reveal that these two mechanical modes show substantial differences in fundamental frequency, of 2.81 MHz and 5.06 MHz. Nonetheless, there is qualitative similarity in the presence of a significantly smaller second-order harmonic, due to the red-blue asymmetry of the spectrum, and in the Lorentzian lineshape of the self-oscillation spectra. The linewidths of 1.1 kHz and 1.7 kHz for 2.81 MHz and 5.06 MHz, respectively, indicate effective quality factors under damping of 2500 and 2976, respectively. For self-oscillation in a passive cavity with a low-noise laser, the self-oscillation linewidth scales with the ratio of phonon population to thermal phonon population in an analogue to the Schawlow-Townes linewidth of masers,

$$\delta\nu = \frac{b_i(2n_{th}+1)}{n_{osc}} \qquad 3.8$$

where n_{osc} and n_{th} are the phonon populations during self-oscillation and at rest under thermal equilibrium, respectively[22]. While we cannot measure the intrinsic damping b_i for these modes due to limitations of available LDV equipment, Figure 3.3 shows a linewidth of >50 kHz for a 4 MHz mode under non-oscillating conditions, indicating a substantial enhancement. Whether or not this is consistent with the optomechanical Schawlow-Townes-like linewidth, or whether the VCSEL's substantial amplitude noise at these mechanical frequencies drives excess noise through radiation pressure, would require direct measurement of the mechanical quality factor as well as simulation of the modes' spring constants in order to calculate n_{osc} from measured oscillation amplitude, given $\frac{1}{2}k_{eff}x_{rms}^2 = n_{osc}\hbar\omega_m$. Nonetheless, this qualitatively demonstrates the above-threshold linewidth narrowing characteristic of both lasing and mechanical self-

oscillation, and highlights the possibilities of using high-Q, large n_{osc} optomechanical oscillators to produce low-phase-noise signals.

3.9 Scanning Electron Microscopy Characterization

To further confirm and gain insight into the mechanism of optomechanical self-oscillation in VCSELs, we sought a method to directly visualize the motion of the HCG MEMS during self-oscillation, in contrast to the indirect methods of characterizing the effects of self-oscillation on the VCSEL's output light or electrical characteristics. The goals of such measurement would be to measure mirror position, ideally resolved over time or over position across the mirror While LDV measurements could accomplish this goal with time resolution, limitations on vacuum strength in our LDV system precluded self-oscillation measurements comparable to those in our Lakeshore stage. White-light interferometry could resolve vertical displacements on the order of those in self-oscillation, but lacks time resolution or sufficient x-y resolution, as well as lacking vacuum capability at Berkeley.

Compared to those methods, scanning-electron microscopy (SEM) stood out as a tool offering fine resolution laterally and vertically (when imaged at an angle) and high vacuum capability. To observe self-oscillation under SEM required electrically contacting the laser while imaging it under SEM. Fortunately, such a feature is possible in electron microscopes configured for electron-beam-induced current (EBIC) measurements, a common tool to measure electrical conductivity in semiconductor microdevices. With the help of Dr. Frank Ogletree at Lawrence Berkeley National Laboratory, we were able to mount the device in an EBIC-equipped Zeiss Supra 55VP SEM and apply drive current. At conditions matching those at which we had observed self-oscillation in the same devices in the Lakeshore, we noticed blurring indicating vertical up-down movement of the device's bars.

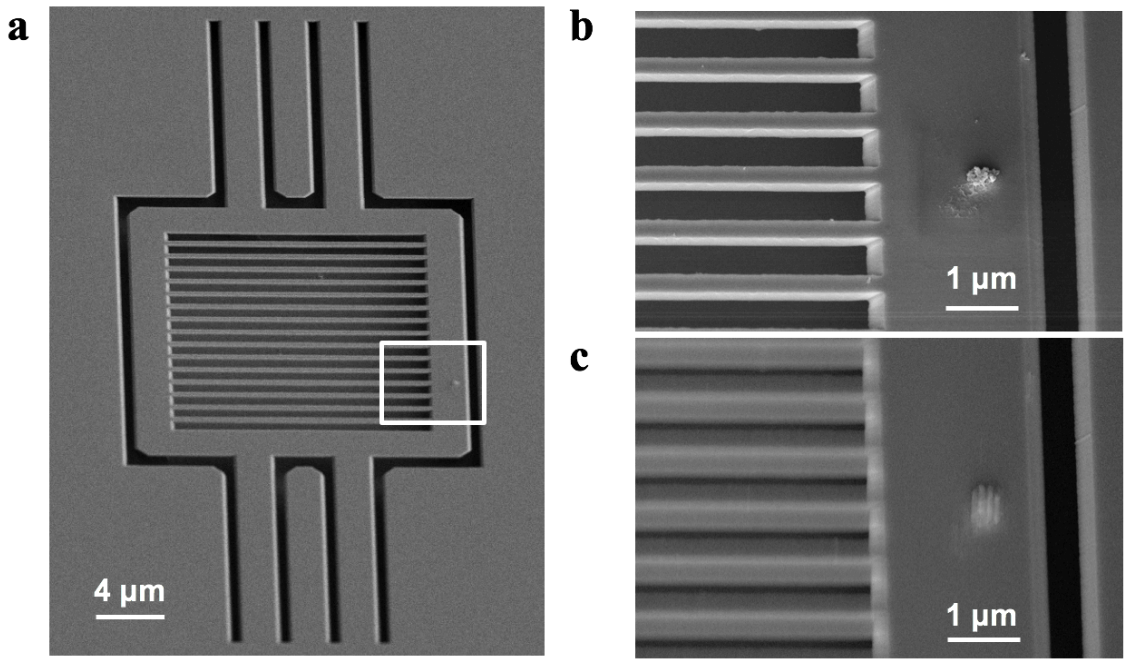

Figure 3.22: SEM characterization of self-oscillating HCG. (a) Entire device, drive current off. (b) Grating bars, frame, dirt on frame, and substrate, current off. (c) Same view, with current on, showing vertical blurring of bars and frame but not substrate.

Because identical microscopy conditions were used in both measurements, taken sequentially, we can conclude that the observed blurring is not a microscopy artifact. Further detailed analysis of the images corroborates this conclusion, as the defects on the fixed, nonmoving substrate are seen to be equally sharp in both photos. Likewise, the speck of unstripped photoresist on the HCG frame is visibly blurred only vertically but not horizontally, further corroborating vertical-only motion.

While this measurement confirmed that the HCG is indeed oscillating vertically throughout the whole HCG bars and frame, this does not fulfill the second goal mentioned previously: providing time- or frequency-domain data on the motion of the MEMS during self-oscillation. At a fastest per-pixel dwell time of 100 ns (plus scan time), the SEM can provide only 80 data points per 8 µs oscillation of a typical MEMS fundamental mode and only 1-5 per period of higher-order modes. Even at such fast scan rates, the motion of the MEMS during the period would introduce stroboscopic effects into the image, making complete time-domain measurement impossible. However, such stroboscopic effects provide a means to indirectly capture periodic time-domain motion happening far faster than the scan rate. Analogous to the effects that produce the appearance of reverse-spinning wheels and bending propeller blades in video and television, the horizontal raster scan introduced a somewhat sinusoidal, periodic deviation into the moving grating bars. As the periodic artifact varied from scan to scan, averaging could not be used for this technique, which therefore relied on the very strong signal strength of the SEM's in-lens detector.

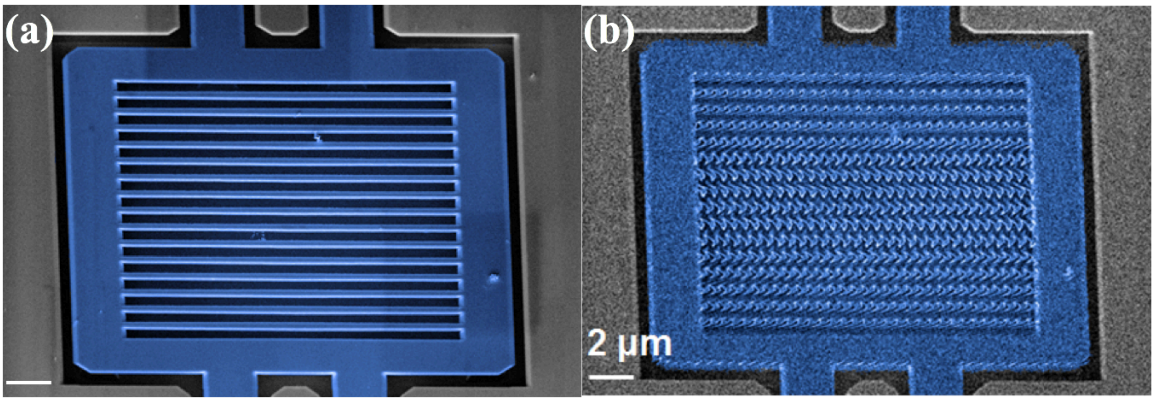

Figure 3.23: Stroboscopic capture of MEMS self-oscillation. (a) Laser off, I_d = 0 mA. Magnification 4.12 kX, working distance 6.6 mm, pressure 1.2e-5 Torr (b) Laser on, I_d = 13 mA, sweep time at fastest possible value 377 msec.

As shown in Figure 3.23, this stroboscopic artifact in the grating bars could be reliably controlled by turning the laser current above and below the self-oscillation threshold, indicating that the periodic motion. The known frame capture time of 377 msec for a pixel count of 1024 x 768 yields a pixel capture time of 480 ns, including pixel-to-pixel scan time. Manually measuring the horizontal period of this oscillation in pixels yielded an average of 17 pixels, equating to a frequency of 122 kHz. Furthermore, using the 45^o tilt angle of the view onto the HCG bars, the vertical motion is calculated to be 600 nm, confirming the results from time-resolved spectrum analysis.

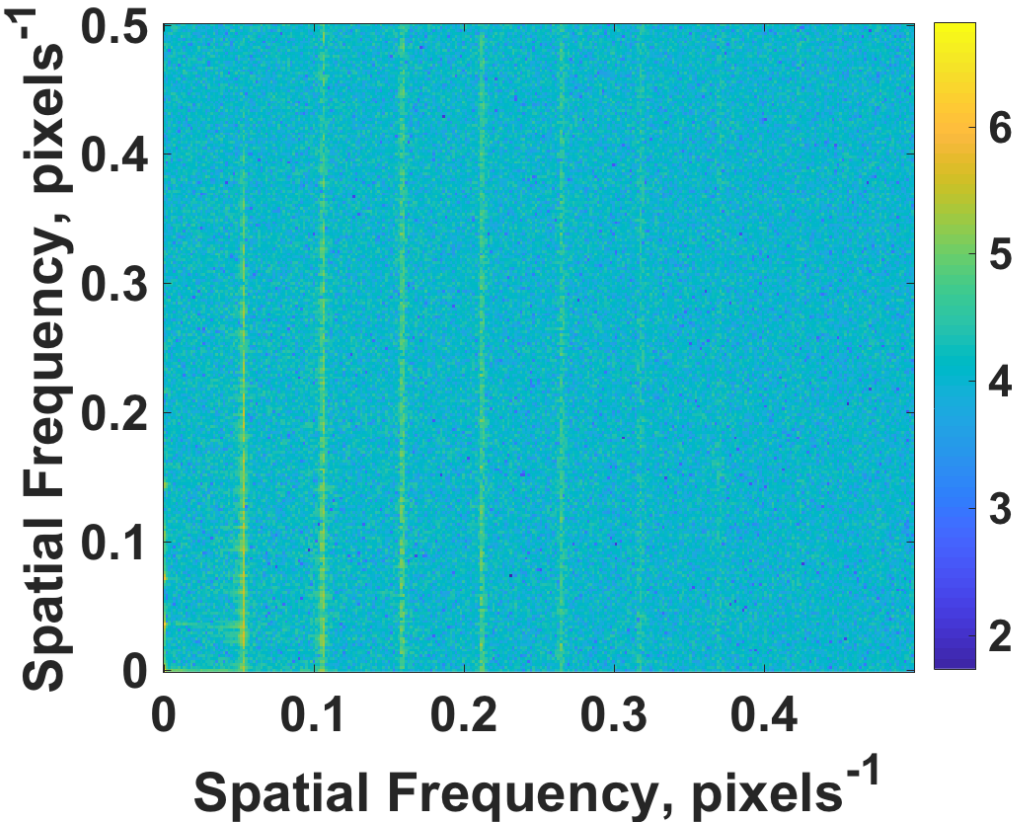

Figure 3.24: Spatial 2D-DFT in (x,y) of area with HCG bars in Figure 3.23. Vertical stripes here correspond to periodic features in the x-direction, resulting from self-oscillation stroboscopic distortion

Instead of manually counting pixels, the period of oscillation can be determined more accurately from the 2D discrete Fourier transform (2D-DFT) of the image. The 2D-DFT of Figure 3.23, shown in Figure 3.24, reveals a peak for spatial frequencies in the x-direction of 0.053/pixel, corresponding to a period of 18.6 pixels for the 1024-pixel width of the above image. With the 480 nsec scan rate, this gives a period of 8.93 μs or frequency of 112 kHz, slightly lower than that extracted manually. Altogether, both methods of data processing confirm a periodic motion comparable to that extracted from time-resolved spectrum analysis in Section 3.7. This provides a unique view into the behavior of optomechanical phenomena, and is enabled by the large-scale self-oscillation amplitude of the device. Further work in data processing could extract the time-domain mode shape through edge detection and fitting the resulting stroboscopic artefact to models of the distortion.

3.10 Time-Domain Electrical Characterization and Self-Voltage Modulation

3.10.1 Self-Voltage Modulation Theory

In addition to frequency- and amplitude-modulating the output light of the VCSEL, optomechanical self-oscillation simultaneously changes the internal electrical dynamics of the VCSEL. Whether by electrostatically-induced actuation, optomechanical self-oscillation, or an any other external force, changes in mirror position inevitably change the optical Q-factor of the lasing optical cavity. At constant DC laser bias current I_d, sufficiently large changes in optical Q-factor produce both amplitude modulation of output light and also self-modulation of the laser's voltage, V_d. Thus, purely-electrical characterization of a VCSEL

As is noted in multiple standard texts in the field, a laser shows a noticeable kink in its I-V characteristic upon reaching threshold [31]. Since the laser gain, carrier concentration, and diode voltage clamp at threshold to the values of g_{th}, N_{th}, and V_{th}, the laser diode's voltage deviates from the classic Shockley diode equation above laser threshold. With the diode voltage clamped, the laser above-threshold can simply be modeled as a passive network of its shunt and series resistances. This results in a discontinuity of the dI/dV characteristic of the laser at threshold, notably producing a drop of $\frac{nk_bT}{q}$ in the $I * \frac{dI}{dV}$ characteristic. Consequently, at a fixed bias current, changes in the optical cavity change the laser diode voltage by changing I_{th}. At a fixed current, using the piecewise clamping approximation provided by Coldren, we can derive the change in diode voltage between a lasing condition and non-lasing condition:

$$\Delta V(I) = V_L(I) - V_{NL}(I) = \frac{nk_bT}{q} \ln\left(\frac{I}{I_{th}}\right) \qquad 3.9$$

For lasers undergoing self-modulation of power and wavelength, this analysis notes that there will be a corresponding self-modulation of laser voltage, which we term self-voltage modulation.

While recent research by the Chang-Hasnain group has shown the clamping approximation to fail due to self-heating for large bias currents above threshold, it is sufficient for the present analysis in the above-threshold but pre-rolloff regime [36].

3.10.2 Self-Voltage Modulation Experiment

To electrically measure self-oscillation, we mounted a VCSEL chip in the Lakeshore vacuum chamber under comparable conditions to the time-resolved wavelength experiment. Light was captured from the VCSEL into a fiber and measured in a high-speed DET01CFC photodetector. The drive current was applied to the laser through the DC connector of a Picosecond bias-T. An Agilent 500 MHz oscilloscope measured both the voltage of the laser and the voltage of the photodetector through the AC ports of their respective bias-tees. The tuning contact of the laser was shorted to its drive contact to avoid spurious electromagnetic actuation. Altogether, the oscilloscope data thus provided

a live time-domain view of the joint self-voltage and self-amplitude modulation of the VCSEL.

As expected, when the laser was biased into a range of conditions wherein self-oscillation had previously been observed, we observed self-modulation of the laser's power and voltage simultaneously, in clear synchronization.

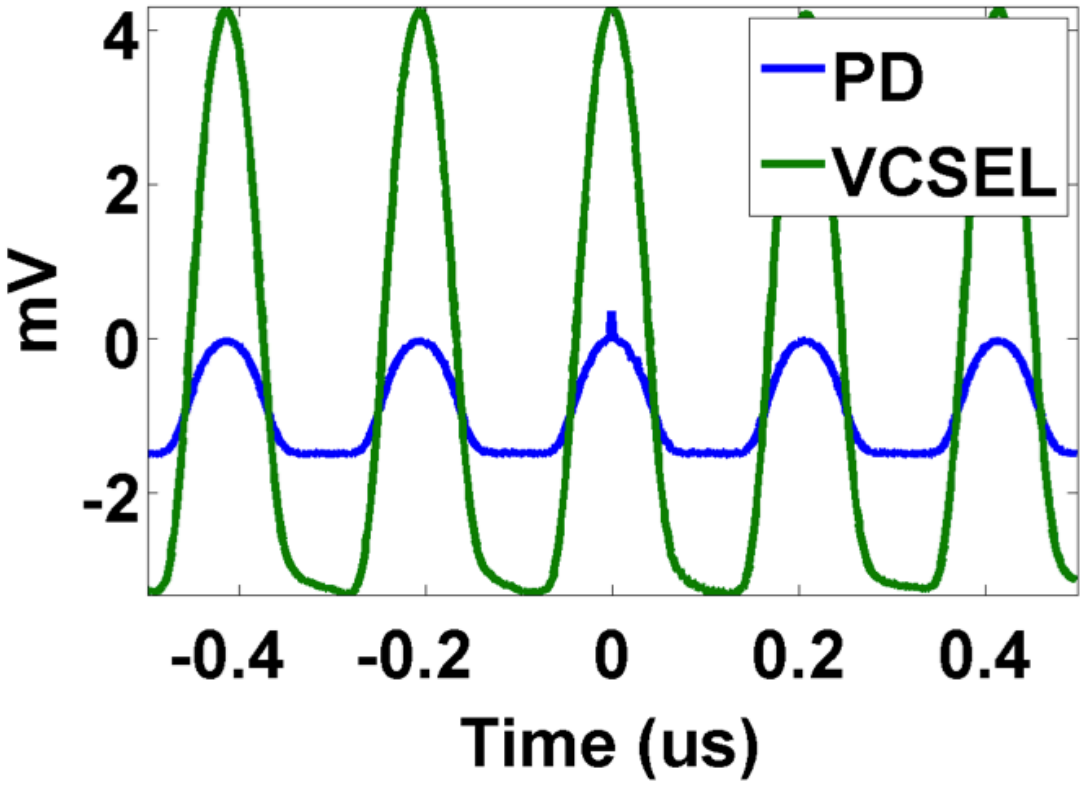

Figure 3.25: VCSEL self-modulated voltage (green) and photodetector-measured output power (blue) under self-oscillation. Photodetector signal includes unmeasurable optical losses and is intended as an arbitrary-units representation of time-domain optical power in synchronization with VCSEL self-voltage modulation.

The frequency of the self-modulation clearly indicates the 5 MHz higher-order mode characterized by time-resolved wavelength spectroscopy and other methods for the same family of devices. Given that the laser under this condition was self-modulating from a fully on to fully off state, we can apply Equation 3.8 to confirm the amplitude. For the drive current of 11.5 mA, lasing threshold of lookup 9mA, and ideality factor of 2, this gives a 10 mV peak-peak voltage self-modulation amplitude, compared to the 8 mV noted in Figure 3.25: VCSEL self-modulated voltage (green) and photodetector-measured output power (blue) under self-oscillation. Photodetector signal includes unmeasurable optical losses and is intended as an arbitrary-units representation of time-domain optical power in synchronization with VCSEL self-voltage modulation..

3.10.3 Applications of Self-Voltage Modulation

Self-voltage modulation provides another window into self-oscillation for both characterization and systems purposes. Within the realm of characterization, it simplifies the hunt for new self-oscillation phenomena in VCSELs by relieving the need to optically couple the device. VCSELs can simply be probed with DC current and the time-domain

In a systems domain, self-voltage modulation allows a system using an optomechanical VCSEL to track self-oscillation without the need to locally split off and measure output light using a k-clock or similar device. This greatly simplifies the use of optomechanical VCSELs in wavelength-swept imaging, where the wavelength of a swept source (even an intentionally-swept, not self-swept, source) is typically tracked by k-clocking. Measuring the time-domain sweep could also enable feedback through the laser drive current or tuning voltage to reduce noise in the oscillator or lock the oscillation to a separate frequency source. Theoretically, self-modulated voltage could also enable optomechanical VCSELs to be used as all-electrical clocks or sensors driven from DC current, particularly given high-Q MEMS. While the clocking application would likely compete poorly on metrics of cost, SWAP, and phase noise with existing ring oscillators and crystal oscillators, optomechanical VCSELs could provide advantages in sensing applications by detecting small changes of adsorbed mass to the HCG MEMS, such as bacteria or particulate from the atmosphere.

4 Analysis of Self-Oscillation Phenomena

4.1 Overview

In this section, we apply the theoretical description of cavity optomechanics provided in the Theory section to the experimental data on self-oscillation, to both confirm and provide insight into this mechanism. After illustrating that radiation-pressure optomechanics can explain these self-oscillation behaviors, we use finite-element simulation and theoretical analysis to rule out the only other plausible mechanism, photothermal optomechanical actuation. Lastly, we will apply the model presented to illustrate the potential advantages that active cavities, particularly HCG-tunable VCSELs, can bring to the field of cavity optomechanics.

4.2 Threshold confirmation for large-sweep TE-HCG 1550-nm VCSEL

The exceptional behavior of the 1550 nm TE-HCG device that demonstrated large-sweep self-oscillation, together with the substantial body data available regarding the device, serves to make this device the best candidate for extensive analysis. As we reported in Scientific Reports in 2015, we use corresponding information from LDV, finite-element analysis, and time-resolved spectrum analysis to implement the rate-equation model described earlier to corroborate the device's large-swept self-oscillation behavior [30]. Confirming the large-amplitude oscillation behavior will take two parts: small-signal analysis to confirm that the radiation pressure will lead to self-oscillation in the specified device, and nonlinear large-signal analysis to confirm that radiation pressure can sustain self-oscillation of the amplitude observed. The former goal will be addressed in this section, and the latter in the following.

As previously discussed in the section "Theoretical Analysis of Optomechanical Dynamics," optomechanical self-oscillation begins in any device when optomechanical anti-damping, b_{OM}, overcomes intrinsic damping b. In this small-signal linearized picture, anti-damping can be described as originating from two ingredients, the force gradient $\frac{dF_{OM}}{dx}$ and delay $\tau_c(x)$. This can be intuitively seen though phasor analysis, wherein the out-of-phase component of the optical spring force cancels, or adds to, intrinsic damping. In the fully general picture, the optomechanical force can include radiation pressure, photothermal forces, and radiometric forces.

To determine if radiation pressure antidamping can counteract mechanical damping value and lead to instability, we insert TE 1550 nm device parameters into the analytical formulas for the small-signal response of radiation pressure force to fundamental mode mirror position, as derived in Section 2.5. Figure 4.1 plots a typical frequency response of $|\frac{dF_{RP}}{dx}|$ and τ_c for an HCG VCSEL at a typical current value and mirror position. They show a transfer function with a resonance frequency at 860 MHz. For the fundamental oscillation mode (set at 125 kHz), $|\frac{dF_{RP}}{dx}|$, τ_c, and $|\frac{dF_{RP}}{dx}| \cdot \tau_c$ are calculated for each mirror displacement x, shown in Fig. 5d-e.

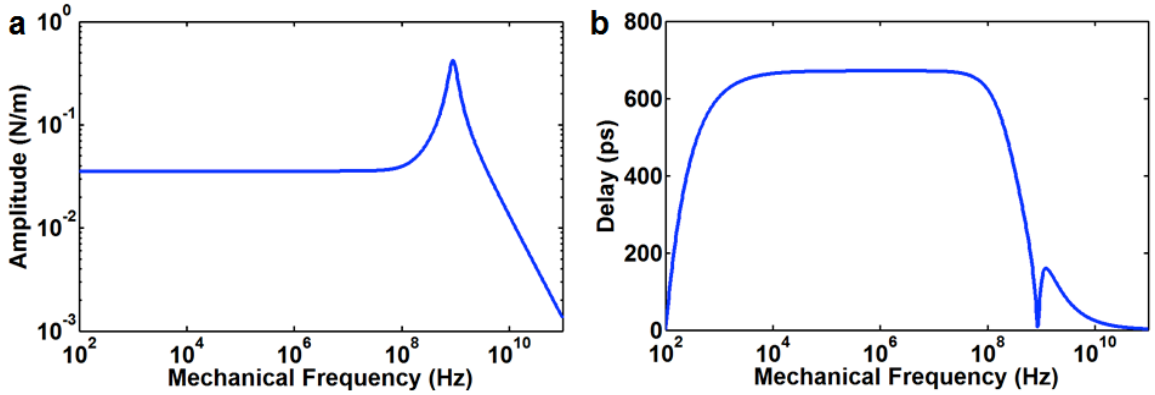

Figure 4.1: As calculated from the rate equations treating mirror position x as input, $F_{OM}(x)$, frequency response of (a) force gradient dF/dx and (b) delay time as defined in Equation 2.24.

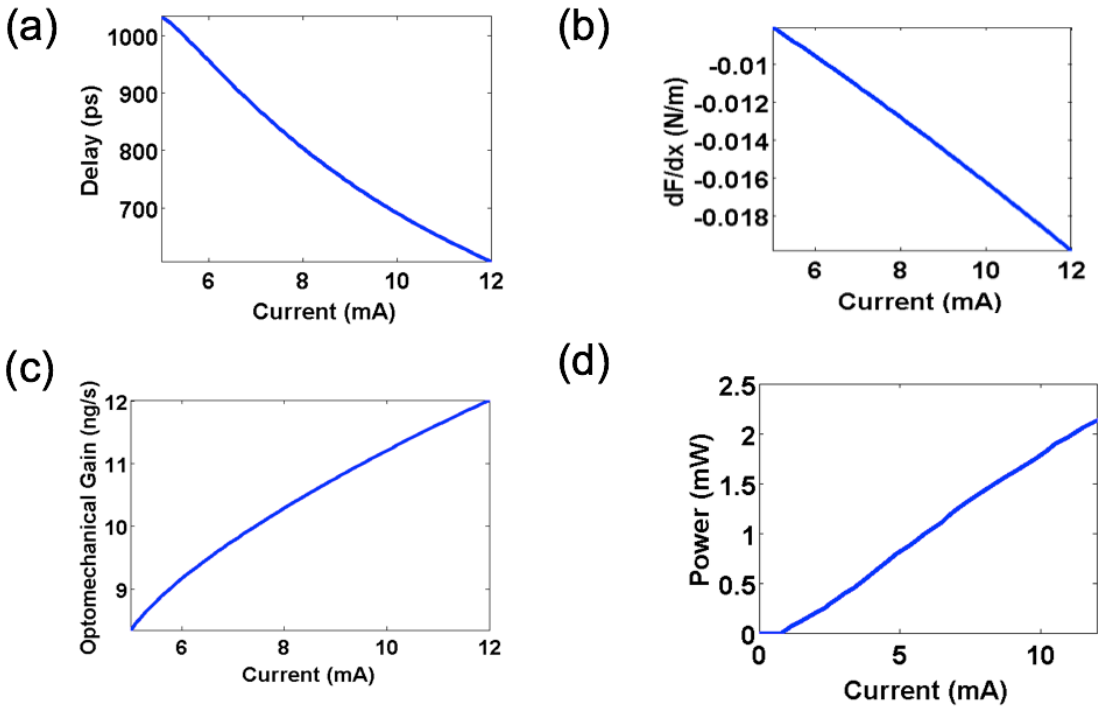

Figure 4.2: Small-signal picture of optomechanical antidamping calculated from rate equation-calculated response of laser force to mirror position, $F_{OM}(x)$, vs. DC drive current (a) delay (ps), (b) optical force gradient dF/dx (c) optomechanical antidamping b_{om}. (d) experimental optical power vs. current (L-I) data for a 1.55µm HCG VCSEL, corroborating model parameters.

Given the degree to which full-device simulations must rely on microscopic parameters unique to each device, the above can only be taken as a representative example of the optomechanical antidamping that can be provided by a TE-HCG 1550 nm device with

parameters comparable to those used in the large-sweep experiments. At I_d = 10 mA, at which the largest self-oscillation was shown to occur in Figure 3.15, the device exhibits 11 ng/s of optomechanical antidamping. For the devices that showed large-sweep behavior, the 130 pg mirror and 125 kHz resonance frequency would equate that value of antidamping to a mechanical Q-factor of 9,280. This value lies on the upper end of the reasonable range of mode Q-factors that can be expected for TE HCG fundamental modes. Thus, while this analysis confirms that radiation pressure is the dominant source of antidamping in producing large-sweep self-oscillation, further analysis and experiments can determine whether this discrepancy can be addressed by measuring more accurate values for device parameters used in the above analysis, or whether the discrepancy is best addressed by considering secondary forces that could also provide antidamping. Accordingly, in Section 4.3 we apply simulations to quantify the extent to which photothermal effects contribute to the optomechanical forces in HCG VCSELs.

4.3 Evaluation of Photothermal Contributions to Antidamping

As described previously, calculating photothermal forces directly and analytically is not possible as it was for radiation pressure due to the complicated serious of effects that occur in photothermal actuation. In fact, it is a great simplification to treat photothermal effects as a force at all; rather, optically-induced expansion produces extremely large forces which deform the resting position of the MEMS, rather than applying a force that is counteracted by the MEMS. Accordingly, we take a multi-step approach of calculating optical absorption, simulating self-heating in space and time domain, and determining thermal distortion as a 3-D effect. Due to the numerous internal parameters and several simulation steps involved in this calculation, the resulting calculation cannot directly give a reliable quantity for the photothermally-induced contribution to anti-damping b_{PT}. Nonetheless, by taking a "best-case" approach of this calculation by estimating maximum photothermal effects in each step of the calculation, we can put an upper bound on photothermal effects and show that they are both qualitatively and quantitatively a minor contributing effect to the observed optomechanical behaviors.

Across all HCG VCSELs, the HCG material and doping (if any) are chosen to minimize optical absorption in the HCG. For the 1550-1570 nm VCSELs used in most optomechanics experiments, the photon energy of 0.8 Ev is well below the bandgap of the HCG material, InP. The only optical absorption mechanism in the HCG is free carrier absorption, which has been measured to be 44 cm^{-1} for p-InP at the p = 3e18 cm^{-3} doping level of the HCG. The HCG is doped primarily to facilitate electrical conductivity for capacitative actuation and to provide a diode effect limiting drain current across the capacitative MEMS. At an output power of 1.7 mW, the circulating cavity power is ~850 mW using a top mirror reflectivity of 99.8%. The HCG does not absorb in a way comparable to a thin sheet of equivalent material, but rather confines light disproportionately in the high or low-index regions depending on the exact mode interference pattern for the input wavelength. This is best illustrated and calculated using the array-waveguide method developed by our group. For the 1550 nm TE-HCG design, such calculations give a transverse confinement factor of 32%, giving a resulting

absorbed power of 440 μW in the HCG for a VCSEL as described with parameters from Table 2.1.

Next, we use finite-element method (FEM) thermal time transient modeling to determine the photothermal force response time, and steady-state calculations to determine the magnitude and distribution of temperature change due to a 440 μW-scale heating in the HCG bars, as determined from the optical absorption. With standard values for InP thermal conductivity and heat capacity, a test heat source of 2 μW in the HCG bars representing absorption, and the supports fixed at ambient temperature, time-domain results shown in Figure 4.3 fit well to an exponential time-domain model with a thermal time constant of 19 μs, corresponding to a frequency of 53 kHz that is significantly lower than the range of self-oscillation frequencies observed in 1550 nm devices (120 kHz - 5 MHz). These linear time-domain dynamics, confirmed by the exponential temperature vs. time fitting, would produce a one-pole lowpass effect further weakening photothermal effects for the observed frequencies, as will be analytically discussed below.

In addition to the time-domain effects, we use FEM steady-state thermal modeling to show the 3D distribution of temperature and physical warping of the MEMS structure due to photothermal effects, with a 440 μW heat source applied on the bottom of the bars, and modeling thermal expansion of the InP. The 2D slice of the distribution of temperature along the surface of the MEMS structure, confirming the 135 K warming due to 440 μW found above, and showing that the temperature change in the MEMS support arms is significantly smaller (< 80 K). Using this temperature profile to simulate thermal expansion, as shown in Figure 4.4, gives a maximum vertical displacement of Δz_{PT} = 384 pm, which we back-calculate to an equivalent "force" of F_{PT} = 2.2 nN. The amplitude induced by sinusoidal light at the mechanical resonance frequency ω_o, as is produced in self-oscillation, can be related to the static displacement[37]:

$$z_{PT}(\omega_o) = Q_m \frac{\omega_o \tau}{1 + (\omega_o \tau)^2} \frac{z_{PT,DC}}{P_{DC}} P(\omega_o) \qquad 4.1$$

With the static thermal displacement of 384 pm, and for complete on-off modulation of light power $P(\omega_o)$ = 1 mW, this results in a displacement oscillation amplitude $x_{PT}(\omega_o)$ = 90 nm. Thus, given the available device parameters, the photothermal force accounts for a significant portion of the energy transfer from light into the mechanical mode, but cannot account for the observed self-oscillation amplitude (~600 nm) without radiation-pressure forces as well.

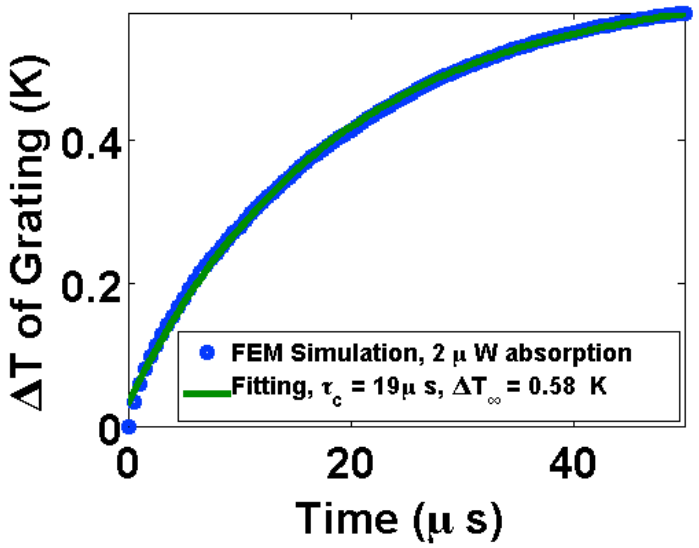

Figure 4.3: Time-domain step response of HCG temperature to heating source in the bars, calculated with FEM for as-fabricated HCG structure.

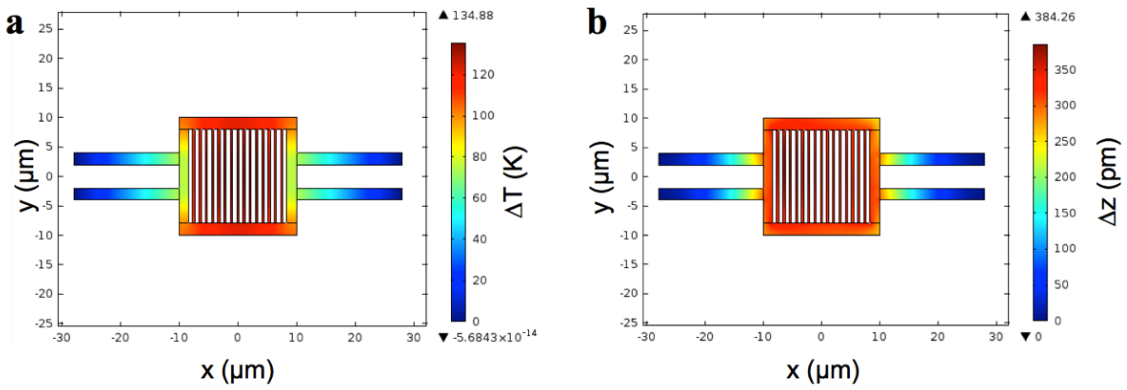

Figure 4.4 FEM simulations of (a) temperature profile and (b) distortion profile in the HCG with a heat source representing optical absorption. For total heat source power of 440 μW, a maximum ΔT = 135 K and Δz = 384 pm.

Additionally, the 3-D simulations of z-displacement provide an even stronger argument against the role of photothermal effects in the observed optomechanical phenomena. As Figure 4.4 shows, the vertical displacement Δz results from lateral expansion of the mirror and frame causing buckling in the arms to relax the lateral strain. Such buckling is fundamentally symmetric, and acts in whichever direction relaxes the strain. For a mirror already pulled down under DC electrostatic tuning voltage V_t, lateral expansion in the mirror would be relaxed by further downwards motion of the mirror. Accordingly, increasing laser power would correlate with downwards motion of the MEMS, opposite of the effect of radiation pressure. Such an effect is not observed in any of the time-resolved spectrum analysis (TRSA) data in this work, which uniformly show upward motion of the mirror correlating with times of higher laser power.

Altogether, these analyses show that the contribution of radiation pressure to the observed optomechanical self-oscillation is far larger than that of photothermal effects, which are neglected in subsequent analysis. Nonetheless, the possibility exists to use photothermal actuation to produce qualitatively different optomechanical effects from those observed, given significantly lower-frequency MEMS with higher optical absorption or better thermal isolation, e.g. HCGs supported by MEMS arms of SiN, diamond, or another thermal insulator. If such a system could be implemented with a sufficient $\frac{d\lambda}{dP}$ from photothermal effects, this could be used to counteract the VCSEL's self-heating chirp.

4.4 Analysis of Amplitude-Stable Oscillation via Radiation Pressure

Inducing mechanical instability through anti-damping is only the first step towards self-oscillation behaviors, whether in optomechanical cavities, in lasers, or in electrical oscillators. Instability causes the intrinsic thermal motion of the oscillator to grow in amplitude over time, adding energy into the vibrating mode. With increasing amplitude, the input work per cycle increases, as does the damping work per cycle, until some amplitude at which the additional work gained from increasing amplitude is more than negated by the additional work lost to damping. The result is a spring-like effect maintaining a constant stable amplitude.

While an example VCSEL is well-described by the coupled rate equations and simple harmonic oscillator equations used in the previous section, to simulate the full process of the oscillation growing from thermal noise using an ODE solver would be fruitless. Not only would this require computing several thousand periods worth of oscillation (tens of thousands of steps at a reasonable step time), but accumulating numerical errors over the long computation would degrade the results and possibly lead to nonphysical "blowup" effects. For a significantly simplified calculation method, we assume a sinusoidal periodic motion of the HCG at the resonance frequency, and apply the previously derived laser rate equations as a response to mirror position to calculate the work done on the MEMS structure by radiation pressure throughout a cycle. Such an ansatz is recommended for passive-cavity optomechanical self-oscillation when the mechanical and optical decay times are much longer than an optical period, as is the case here[22]. For passive cavities, the Fouier coefficients of the periodic evolution of the photon population*, n(t)*, and all other time varying parameters, can be analytically derived.

The equivalent analysis is substantially more complex for active cavities, it is necessary to evaluate the rate equations as an ODE with position x(t) as the time-domain input, calculating photon density S(t), carrier concentration N(t), and thus optomechanical force F(t). At 4000 points throughout the mechanical oscillation, the laser rate equations are evaluated fully to give the radiation pressure force on the mirror. Integrating the dot product of this force and the mirror's velocity determines the work per cycle of optomechanical forces on the mirror. Likewise, integrating the mechanical damping power provides the damping work per cycle, which for a sinusoidal path of amplitude x_o can be determined analytically:

$$W_{cyc} = b\omega^2 x_o^2/2 \qquad 4.2$$

Using a mechanical Q of 6,000 and other parameters as used in previous simulations of 1550 nm TE HCG devices, we find that sinusoidal oscillations would experience greater positive work from radiation pressure than negative work from damping until an amplitude of 580 nm. Above this amplitude, the damping consistently removes more energy per cycle than radiation pressure is able to provide, meaning that 580 nm would be the stable oscillation amplitude for the conditions used.

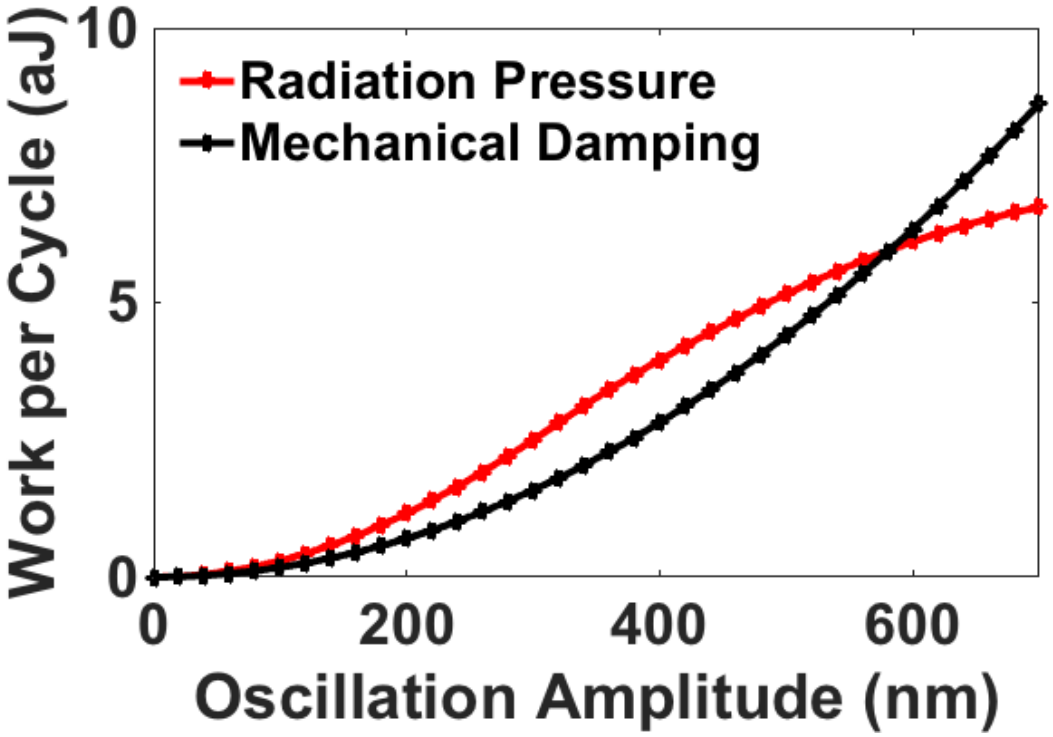

Figure 4.5: Work per cycle due to mechanical damping and radiation pressure vs. amplitude of sinusoidal motion, illustrating the mechanism for amplitude growth from thermal motion to 580 nm stable self-oscillation.

Given that the results of TRSA characterization point to a position vs. time trace resembling between a triangle wave and sinewave, the sinewave approximation is reasonable, but not a complete picture confirming large-amplitude stable oscillation. To simulate the full nonlinear ODE in the time domain, methods such as shooting could be applied, though even this would require forcing the known periodic time of oscillation. In any case, that even simple modeling can recreate the noteworthy large-amplitude stable self-oscillation helps confirm that radiation pressure is the source of the work needed to sustain oscillation. While not a direct calculation of this simulation, the above figure also calls to attention the total power transferred to the device: 6 aJ/cycle in an 8 μs cycle, or about 0.75 nW of mechanical power out of a total 30 mW electrical power driving the VCSEL.

4.5 Comparison of Active and Passive Optomechanical Dynamics

The radiation-pressure-based theory for optomechanical self-oscillation behaviors points to various advantages in the dynamics of active cavities, compared to passive cavities, that enable the large-amplitude self-oscillation. While the main advantage of electrically-pumped active optomechanics—the simplicity of the experiment integrated into one device and the applications that system can unlock—does not require any modeling to verify, modeling can provide insight into how the different dynamics of active cavities can be exploited for further results. Rather than fully compare the time-domain nonlinear dynamics of both active and passive cavities, we instead focus on a comparison of the phenomena and parameters that contribute to radiation-pressure antidamping in both systems.

For a passive optomechanical cavity of coupling constant g_o, optical decay rate κ, mechanical frequency Ω_m, and detuning between input laser and cavity resonance Δ, the optomechanical damping can be expressed following Aspelmeyer [22]:

$$\Gamma_{om} = n_{cav} g_o^2 \left(\frac{\kappa}{\frac{\kappa^2}{4} + (\Delta + \Omega_m)^2} - \frac{\kappa}{\frac{\kappa^2}{4} + (\Delta - \Omega_m)^2} \right) \tag{4.3}$$

As a function of detuning, $\Gamma_{om}(\Delta) = b_{om}/m_{eff}$ is antisymmetric, producing antidamping or damping equally depending on detuning. This expression relates to the relative amplitude of the red-detuned and blue-detuned sidebands of the laser, modulated by the mechanical frequency, being shaped by the lineshape of the cavity. In the resolved-sideband regime, $\Omega_m >> \kappa$, this expression finds the maximum positive or negative optomechanical damping.

$$\max\left(|\Gamma_{om}|\right) = 4 n_{cav} g_o^2 / \kappa \tag{4.4}$$

occurring when the laser is detuned such that either sideband lands on the resonance peak of the passive cavity. In the opposite extreme case where $\Omega_m << \kappa$, termed the Doppler regime, the damping is even more severely limited to $6\sqrt{3}\, n_{cav} \Omega_m g_o^2 / \kappa^2$, which would be far smaller. In either case, the ingredients to maximize antidamping or damping are clear: high cavity power, strong optomechanical coupling coefficient g_o, low cavity decay κ, and high mechanical frequency. Taken together, these desired parameter changes all picture a high-finesse passive cavity with extremely sensitive mechanical coupling, which would detune the cavity on or off the laser in a minimum amount of distance (normalized to the mode's zero-point distance). In addition to be challenging to fabricate, high-finesse cavities, these conditions also restrict the range of positions over which the mechanical system experiences anti-damping, thus limiting large-amplitude oscillation.

In the delayed spring picture of optomechanical interaction, optomechanical anti-damping arises from the retarded component of the optomechanical spring force. In a passive cavity, the two ingredients necessary—force gradient and delay—both originate from the optical finesse. By contrast, in active cavity optomechanics, the two factors originate from separate sources. The delay originates from laser relaxation oscillations, while the force gradient originates from the mirror spectrum or mirror degradation, which can be both independent of the cavity linewidth and decay rate. This decoupling enables a wider design space in which to find parameters in active cavities that can lead to large antidamping, and decouples the tight tradeoffs involved in designing passive optomechanical cavities.

5 Harnessing Optomechanics in VCSELs: Design and Fabrication

5.1 Introduction

Optomechanical behaviors in VCSELs present a platform to study optomechanical dynamics, a source of wavelength-modulated or amplitude-modulated light, and an integrated means to actuate various MEMS modes. However, given that current generation HCG VCSELs were not designed for optomechanical behavior, and that the design figures of merit (FOMs) for maximizing optomechanical interaction can be contradictory to the requirements of other VCSEL applications, we present design advances and new experiments to lead toward those applications.

The applications available to active-cavity optomechanics span both the ranging and spectroscopy applications of swept-source light as well as many of the applications foreseen for passive cavity optomechanics. In addition to the interesting physics of manipulating mechanical systems within the quantum regime, cavity optomechanics has also promised applications within measurement, sensing, frequency generation, and optical signal processing[38]. Optomechanical cooling enables micro-optical mechanical sensors to avoid thermal noise, providing high-sensitivity and high-bandwidth accelerometers in one key example [39]. While cooling is not demonstrated or theoretically suggested in this work, optomechanical excitation also provides advantages over electrically-actuated systems in sensors and frequency sources. Since electrical actuation mechanisms add noise and mechanical losses to micromechanical systems, optomechanical excitation allows low phase-noise oscillation. Resonator designs enabled by optomechanical excitation have shown low phase-noise signal generation in both pure optomechanical [40] and in hybrid capacitative and optomechanical excitation [41]. While the metrics of phase noise (dBc at 10 kHz offset) and SWAP are not currently competitive with crystal oscillators, OMOs provide a more promising pathway forward to GHz oscillators by developing high-frequency, high-Q_m MEMS structures.

5.2 Modulated Light: Applications and FOMs

Whether by self-oscillation or induced-oscillation, optomechanical VCSELs provide unique patterns of modulated light produced by a simple, chip-integrated source. Wavelength-swept light is currently an active area of research with applications in imaging/ranging and spectroscopy. Wavelength-swept ranging and imaging can be treated together because of the fundamental similarities between frequency-modulated continuous-wave LIDAR and swept-source optical coherence tomography. In both modalities, wavelength-swept light returning from the object is interfered with currently-produced light, and the resulting RF beat pattern gives an indication of the optical

distance traveled by the light to the target. Both suffer from Fourier-imposed limits of resolution δz that based on the maximum wavelength sweep $\Delta\lambda$:

$$\delta z = \frac{2\ln(2)\lambda_o^2}{\pi\Delta\lambda} \quad 5.1$$

while the maximum range Δz can be related to the ability to sample wavelength, which is limited by the instantaneous laser linewidth $\delta\lambda$:

$$\Delta z = \frac{\lambda_o^2}{4\delta\lambda} \quad 5.2$$

Thus, the number of resolvable axial points $\Delta z/\delta z$ corresponds to the ratio between laser tuning range and laser instantaneous linewidth, a metric that can readily be compared across different categories of swept laser light.

Within this dissertation and in much of this group's research, the term "tunable" is only applied to VCSEL devices that have a mechanical tuning system in addition to the intrinsic self-heating-based current tuning present in all semiconductor diode lasers. Outside of VCSELs, such independent tuning mechanism can also consist of index-tuned DBR reflectors in in-plane waveguide edge-emitting lasers. However, real-world tunable laser systems frequently use two-terminal lasers tuned only through current tuning in applications where system simplicity is more important than total wavelength sweep. [42]. Accordingly, using optomechanical VCSELs as two-terminal wavelength-swept sources, in either the induced optomechanics or self-oscillation regimes, can address low-cost, portable wavelength-swept applications in ranging and spectroscopy.

In one such experimental result, a current-tuned VCSEL operating at a wavelength of 2365 nm is tuned across a 3 nm range to detect the absorption lines of CO and CH_4 in that region, with the goal of early detection of fire in the atmosphere. The current-tuned VCSEL is scanned with a slow 10 Hz plus a faster dithering signal of 6 kHz. For noise performance, the spectrum is measured in the second derivative by locking to the second RF harmonic (12 kHz) of the high-frequency modulation. This enables fast, high-sensitivity measurement of the spectrum, with a particular ability to resolve spectrally narrow but small-amplitude changes in the transmission induced by the added trace gas absorption lines. Optomechanical VCSELs can readily produce either the 3 nm scan at a faster rate, or contribute a far higher-frequency dithering signal. Either of such changes could reduce acquisition time or improve SNR by avoiding $1/f$ noise. A much faster acquisition, given sufficient SNR, could even lead to a beam-scanned system to develop maps of target substances. Since a key FOM for tunable laser spectroscopy is the temporal stability of the sweep, measured via Allan deviation, such measurements could be fruitful to be carried out for VCSELs as well. While the ESA and TRSA measurements qualitatively confirmed frequency stability of optomechanical oscillations over time, a full Allan deviation measurement across a range of timescales could reveal the suitability of optomechanical dynamics for this application.

5.3 MEMS actuation

Designing new structures for VCSEL optomechanical behaviors requires developing new means to achieve greater optical force gradient $\frac{dF_{RP}}{dx}$ via mirror spectrum or mirror degradation, respectively $\frac{dR}{d\lambda}$ or $\frac{dR}{dx}|_{\lambda}$. Fortunately, our group has a large body of HCG theory research, both published and unpublished, from which designs can be drawn. As indicated by RCWA and HCG-mode analysis, certain reflective HCG designs can switch to highly transmissive when half the grating bars are removed. The initial motivation for such design was low-power, high-on-off-ratio optical switches, but such grating designs possess sufficient reflectivity to be used as VCSEL mirrors. Performing a sweep of FDTD simulations calculating HCG reflectivity as half the bars in one such design was displaced vertically revealed that a narrow resonance occurred and gradually blueshifted versus displacement.

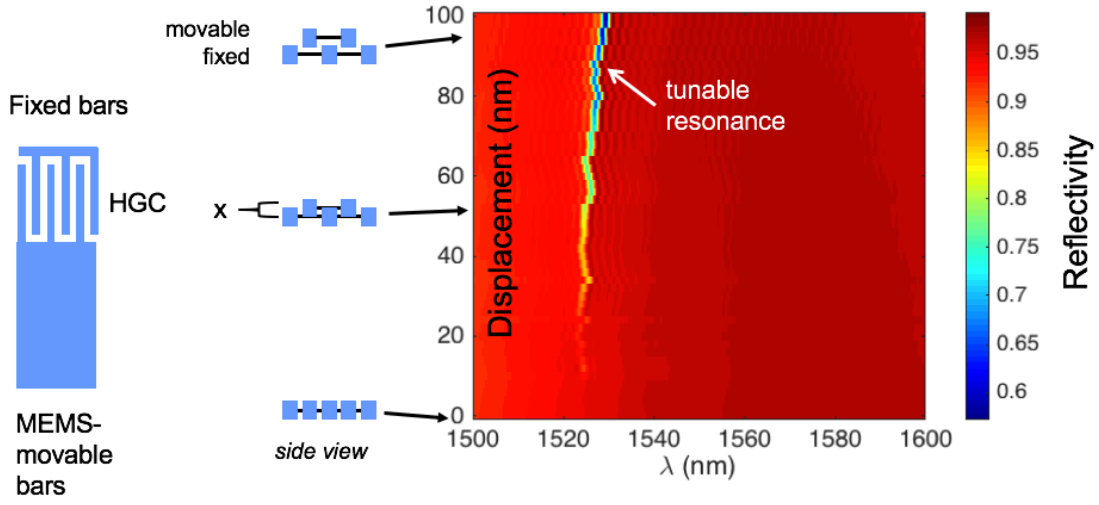

Figure 5.1: Split-grating concept and FDTD simulated reflectivity spectrum vs. displacement of half of the bars

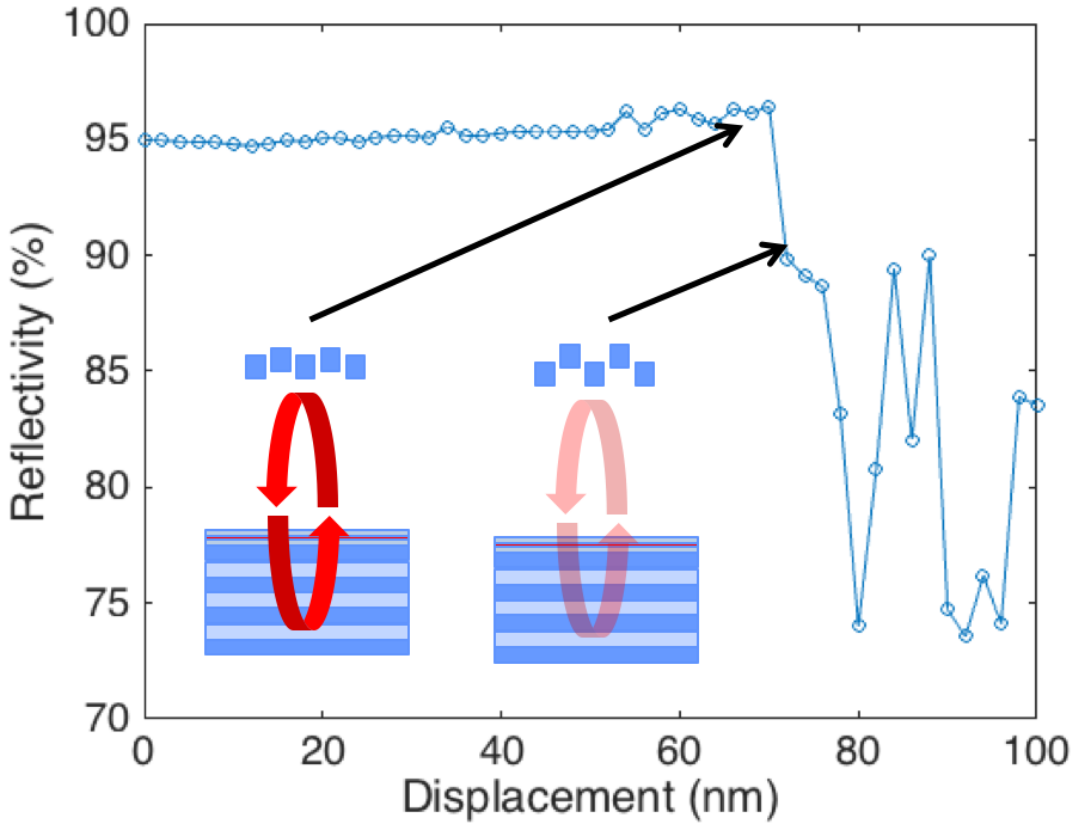

Figure 5.2: Split grating reflectivity vs. displacement at fixed wavelength of 1530 nm, illustrating strong reflectivity dropoff in 2 nm of displacement.

Analyzing reflectivity at constant wavelength vs. displacement shows that the HCG's reflectivity collapses from 95% to 90%, enough to go from lasing to nonlasing, in just 2 nm of displacement. While FDTD measurements of HCG reflectivity tend towards underestimates in high-reflectivity regions, the reflectivity of this design could also be enhanced with compound DBR's below the air gap and HCG, as is common in 1550 nm HCG VCSELs currently. Without taking optomechanical effects into the picture, this raises an interesting possibility of MEMS-actuated Q-switched lasers, though such MEMS frequencies would likely be far slower than typical VCSEL modulation frequencies. With optomechanical effects, the extremely high $\frac{dR}{dx}$ would provide an incredibly high radiation pressure spring constant, k_{opt} and optomechanical anti-damping b_{OM}. For estimates, an ability to fully shut off a typical VCSEL's radiation pressure of 2 nN over 2 nm would provide an k_{opt} on the order of 1 N/m. With a typical delay of 600 ps, this would result in an optomechanical antidamping of 600 ng/s. Using $b = \frac{m\omega}{Q}$, this could provide enough antidamping for a standard 130 pg HCG with resonance at 125 kHz with a quality factor of 200, obtainable through a far more manageable 10 Torr-scale

vacuum. Lastly, by maximizing $\frac{dR}{dx}$, this mechanical design provides a step towards fully self-amplitude-modulated light, minimizing the self-wavelength-modulated component. If MEMS frequencies could be increased through stiffer materials, fully amplitude-modulated light would prove useful in clocking and all-optical signal processing applications, potentially including locking to GHz-scale atomic transitions for atomic clocks.

5.4 Heterogeneous Integration through Bonding

Many of the applications of HCG VCSEL optomechanics share a need for increased mechanical frequency and decreased damping, *b*. Realizing these qualities, in the lab and especially in field applications, will benefit substantially from packaging advances to enable consistent vacuum in the device and the use of stiffer materials for the HCG MEMS. Unfortunately, there is only small stiffness variation within the materials that can be epitaxially grown with the compound semiconductor substrates typically used for VCSELs (InP and GaAs), and sputtered or evaporated dielectric materials often have too unpredictable granularity and refractive index to produce reliable HCG VCSEL mirrors. Therefore, chip bonding presents a way to achieve both heterogeneous integration of non-epitaxial HCGs onto VCSELs and hermetic sealing of a vacuum cavity, achieving both of the stated goals. While epoxy bonding has been used to seal high vacuum inside a MEMS device and to couple the light from a VCSEL cavity to a waveguide, only metal bonding provides the accuracy and stability needed to bond a VCSEL mirror to the cavity.

Fortunately, bonding VCSELs has been a focus in our group since well before the discovery of optomechanics, with a goal of integrating VCSELs with high-efficiency coupling into silicon photonics waveguides and integrating VCSELs with HCGs fabricated out of non-epitaxial materials. These goals have also been joined in efforts to fabricate VCSELs with HCG reflectors that exhibit both sufficiently high reflectivity for lasing, but also couple light into an on-chip waveguide. Substantial research has been undertaken outside the group as well, with both HCG and non-HCG VCSELs, with the goal of coupling VCSEL light into the waveguide (bond-outside-cavity) or enabling non-epitaxial mirrors (bond-in-cavity). Bond-outside-cavity (BoC) technologies include bonding VCSELs to indium bumps with SU-8 prisms to direct light into grating couplers [43]. Bond-inside-cavity (BiC) technologies are particularly common in MEMS-tunable DBR VCSELs [44], in contrast to previous monolithic MEMS-tunable VCSELs. Bonding media in such efforts have included indium solders and epoxy for BoC technologies, while the strict requirements of bond thickness imposed by BiC VCSELs, since any nanometer-scale change of bond thickness changes cavity length and thus lasing wavelength, require more precisely-controlled bond thickness and uniformity.

In this group, we have pursued bonding of VCSELs using both approaches: BoC to electrically and optically connect completed, tested VCSELs onto silicon photonics chips,

and BiC to use non-epitaxial HCGs. The former seeks to address a major problem in silicon photonics—the difficulty of integrating large numbers of high-speed lasers onto a silicon photonics chip. The latter goal seeks to use HCGs fabricated by optical lithography on silicon-on-insulator wafers to alleviate the use of electron-beam lithography to write the HCGs, one of the major pain points in large-scale production of HCG VCSELs. Of the two applications, both require lateral position accuracy that can alight the VCSEL as close to the center of an HCG as possible, or practically < 5 μm. Lateral thickness accuracy is particularly critical for HCG VCSEL BiCs, as thickness variation converts into wavelength variation using the same tuning ratio as electrostatic tuning, typically about 10:1. While electrostatic tuning can compensate for such changes, this introduces device performance degradation for thickness variations of ±20 nm or more. Furthermore, the required bond medium should ideally be thermally and electrically conductive to enable electrical driving of the VCSEL from the chip and prevent power limitations and wavelength drift induced by self-heating. Altogether, these factors made metal bonding, particularly gold-tin eutectic bonding, the ideal choice for this group's applications. To provide this lateral accuracy, as well as capability to bond interfaces from the single-VCSEL scale to 6" wafer scale, we used a Finetech Fineplacer Lambda system.

Our group first demonstrated a successful BiC VCSEL in 2014, integrating a 1.55 μm VCSEL with a Si HCG fabricated using optical lithography [45]. In that work, HCGs designed as simultaneous reflector-couplers were fabricated on 6" SOI wafers, with lithography performed by an ASML 5500/300 DUV stepper in the Berkeley Nanolab. The remaining layers of the VCSEL structure—multiple-quantum-well (MQW) active region and bottom DBR—were bonded to this HCG substrate at the chip scale. The bond medium was layers of gold and tin deposited onto both sides. Individual devices were defined by aligning the HCGs, the proton implant, and a mesa etch performed after bonding. The lasers showed single-mode operation confirmed by spectrum analysis, and good thermal conductivity enabling 1 mW output power at 20° C. The thermal performance noted an improvement in thermal conductivity compared to equivalent unbonded HCG VCSELs.

Continuing such work and demonstrating coupling from BiC or BoC-bonded VCSELs into SiPh waveguides has been an ongoing goal in the group. Unfortunately, efforts to extend the BiC process shown in [45] to demonstrate waveguide coupling have not yet succeeded, for reasons discussed below. Recently, we have bonded Bandwidth10 HCG VCSELs, diced to single-device scale, onto SiPh chips and shown electrical and optical coupling between the VCSEL and the substrate system. In this work, we evaporated thick AuSn bond pads onto silicon photonics chips fabricated by Sandia National Labs, and attached single BW10 VCSELs to these pads. Low-resistance contact through the patterned bond pads allowed the VCSEL to be electrically connected through the substrate, while a microscope with a 1.55μm-sensitive Xenics IR camera confirmed coupling of light from that VCSEL into on-chip waveguides though second-order grating couplers.

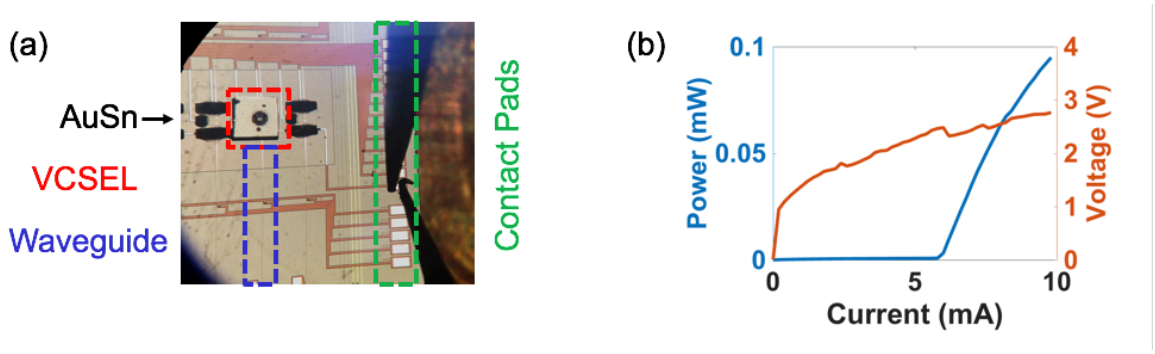

Figure 5.3: (a) Visible-light microscope (10x) image of single-diced VCSEL bonded to SiPh chip. Chip contains Si waveguides (blue) and electrical lines to contact/wirebonding pads (green). (b) VCSEL LIV driven through the bond. Emission captured by a large-area photodetector from topside emission, not counting emission in the direction of the substrate and SiPh waveguide.

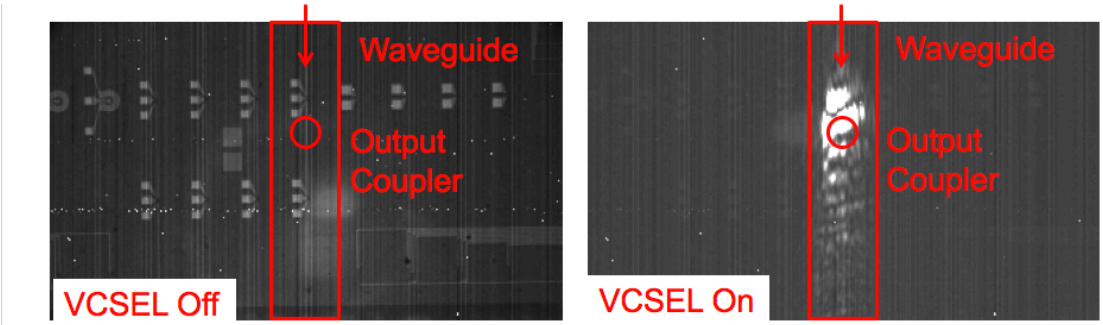

Figure 5.4: Infrared microscope (Xenics XEVA 3643) qualitatively confirming coupling from bonded VCSEL into the on-chip Si waveguide and out through the output coupler. To avoid contamination from light emitted by the VCSEL through its top facet, the VCSEL is far from the field of view of the

Unfortunately, current-generation AuSn thin films evaporated in the Berkeley Nanolab have exhibited too large of a grain size to act as hermetic sealing. As shown in Though AuSn is frequently used to produce hermetic seals, it is typically using thicker films deposited by electroplating. Such films have higher compositional accuracy and thus smaller grain size after reflow, but cannot be grown in layers with the thickness and thickness accuracy constraints needed for BiC VCSELs. As a result, best progress towards hermetically sealed VCSELs will require BoC eutectic bonding of the VCSEL to a nonreflective substrate in vacuum ambient conditions, or vacuum packaging at the TO-can scale.

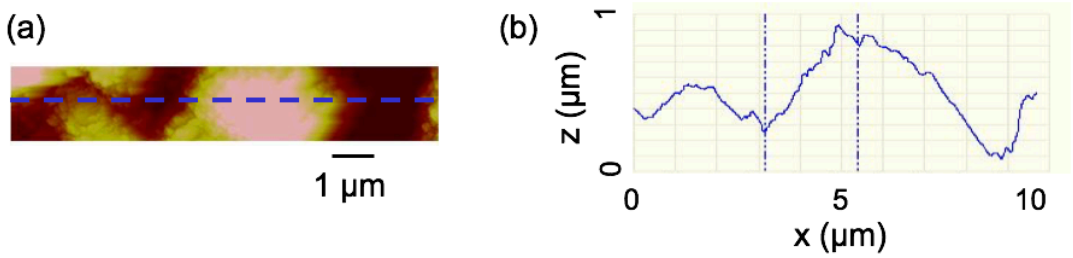

Figure 5.5: Atomic-force microscopy (AFM) scan of eutectic AuSn thin film after reflow (2 µm average thickness) showing 600 nm vertical features, sufficient to prevent hermetic bonding

Whether or not VCSELs can be integrated with individual hermetic sealing though bonding, heterogeneous integration brings opportunities for VCSELs by expanding VCSEL MEMS to include materials outside the epitaxial system. This is already common practice in tunable DBR VCSELs, which can require highly flexible membranes or materials with higher refractive index contrast in order to achieve broadband reflectivity. Within HCG VCSELs, the success of Kemiktarak *et al.* in creating highly reflective telecom-band HCGs from SiN present an important possibility for optomechanical VCSELs. Offering a Young's modulus of 310 GPa, twice that of silicon at 165 GPa and five times that of InP, SiN presents an opportunity to pursue stiffer, higher-frequency MEMS, expanding VCSEL optomechanics towards high-frequency RF applications.

6 Compact Modeling of VCSELs

6.1 Background and Motivation

Efforts to model and simulate the dynamics of semiconductor lasers have existed since the advent of these devices. Given the complex interaction of optics, semiconductors, and thermodynamics that occur in a semiconductor laser, no model can claim to be comprehensive across all behaviors categories of semiconductor laser (or even all kinds of VCSEL). Rather, laser models or must clearly specify the range of devices, behaviors, and design use cases the model is intended to cover.

Most laser behavior models are built upon a system of differential equations describing the rates of transfer by various mechanisms between the carrier population and cavity photon population, commonly termed the laser rate equations. To capture the minimum of fundamental effects of laser threshold, such models must describe the rates of nonradiative carrier recombination, spontaneous emission into the laser mode, stimulated emission, and photon escape from the lasing cavity. That nonlinear system of ODEs lends itself well to manual DC analysis to determine important quantities such as the laser threshold, and to small-signal linearized analysis to determine the current-to-light transfer function describing direct modulation response. Numerical analysis with ODE system methods, including Runge-Kutta, also produces useful approximation of laser time-domain behaviors from such an equation system. On this foundation, a substantial body of work has sought to describe further behaviors, particularly gain compression and self-heating, in ways that are sufficiently general to incorporate with these rate equations. Inevitably, such models rely on a large number of difficult-to-measure internal parameters of the laser, necessitating parameter extraction via fitting to real data. The large majority of laser modeling efforts have sought to only describe the laser in isolation, and have used ad-hoc numerical tools to fit and simulate the model.

By contrast, the field of semiconductor electronics has developed a full-fledged field, called compact modeling, to develop models that can verifiably predict device behavior, describe to a well-defined range of devices, and enable simultaneous system-level simulation with other devices using standard circuit simulation tools. Fulfilling this need requires simplifying the relevant physics of the devices to a form that can be simulated by the limited numerical methods available within circuit simulators while also applying across the range of relevant devices and behaviors. For example, a complete device simulation for a transistor would entail solving for electric potential, drift, and diffusion across a 3-D mesh of the device; a compact model would use insights derived from device simulations to describe a system of differential equations unto which circuit simulators can apply DC, AC, and transient analyses. The former would be of use in device and process development, while the simplified latter enables system-level design. Since the release of the first version of the Berkeley Short-Channel IGFET Model (BSIM) in 1987, several main families of compact models have served successive technology nodes in semiconductor development in recent decades, adapting to an era of substantial changes in transistor design to maintain the progress of Moore's Law. The most common

model family in industry usage, BSIM developed from ongoing work at UC Berkeley in the groups of Profs. Chenming Hu and P. K. Ko. Other families of compact model, using different physical underpinnings than BSIM, have also gained traction within RF circuit design, including the Penn State-Phillips (PSP) model. An industry consortium, the Compact Model Council, provides standardization and best practices across several of the most common families of compact model.

Accordingly, co-design of lasers, particularly VCSELs, with cutting-edge circuits has proven a difficult but fruitful field of research. Recent speed advances in direct-modulated VCSEL interconnects have been enabled by feed-forward equalization (FFE) [46], multi-level modulation [47], and other modulation techniques that require detailed models of laser behavior. Without compact models enabling simultaneous simulation of the electronic and optical components, system simulation has traditionally been accomplished through two approaches: electrical simulation in circuit simulation tools followed by separate optical simulation in MATLAB or other numerical analysis package [48], or through "black box" device models extrapolated from device test data without any physical insight. The first approach, using separate simulation tools, limits the designer to trial-and-error design without taking advantage of many of the automatic design optimization features of circuit simulation tools. Furthermore, it treats the interaction between electronics and optics as one-way, failing to simulate optical effects that change the electrical behavior of the VCSEL, such as the pinning of $\frac{dI}{dV}$ above lasing threshold. The second approach, phenomenological modeling, can only describe behaviors the narrow range of test conditions; while this approach succeeds for strongly linear devices like filters and amplifiers, modeling nonlinear VCSEL behaviors through extrapolation can lead to inaccuracies. Furthermore, lacking any physical insight, the model cannot allow designers to perform standard parameter sensitivity analysis to simulate the robustness of their design to process variations in device parameters, a major concern given the less-stringent process controls in VCSELs, or any III-V process, compared to industrial CMOS.

For these reasons, we and collaborators Nikola Nedovic and William Walker at Fujitsu Laboratories of America concluded that developing the first compact model for a VCSEL would be the ideal approach to address the industry's difficulties in electronics-optics co-design in VCSEL interconnects. With further support and standardization provided by the Nano-Engineered Electronic Device Simulation (NEEDS) node of the NSF's Network for Computational Nanotechnology, we released the Berkeley VCSEL Compact Model (BVCM) through Nanohub. The initial model release, as described below, provides a physics-based compact model of VCSEL direct modulation behavior using readily-extractable parameters. The key advances of the model include its systems to avoid spurious solutions and its treatment of self-heating. Implemented in Verilog-A and tested with major circuit simulation tools (Synopsys HSPICE, Cadence Spectre, and Keysight ADS), the model currently has 450 users as reported by Nanohub and has been used in designs in academia and industry[49].

The following sections will overview the underlying theory, modeling advances, and use of the current model version, followed by a discussion of extensions in progress of relevance to other aspects of this thesis.

6.2 Qualitative Overview of Model Physics

Next, we overview the physics needed to accurately capture the laser dynamics that affects VCSELs under high-speed direct modulation in schemes such as pulse-amplitude-modulation (PAM) with 2 or 4 levels, orthogonal frequency division multiplexing (OFDM)[50], or quadrature amplitude modulation. Designers of such systems need to model the VCSEL's ability to make large, high-speed changes in power. Beyond the standard rate equation, several key VCSEL effects limit this performance: electrical parasitics, optical gain saturation, and device self-heating. Of those, self-heating has been addressed the least successfully in the literature so far, and represents much of the advances of the model shown. These model components interact as shown schematically in Figure 6.1.

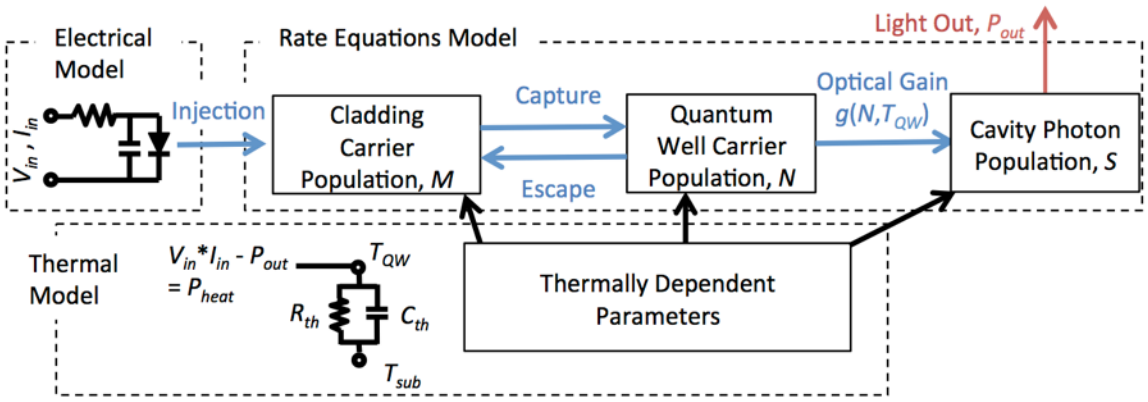

Figure 6.1 Schematic of key model processes and variables: cladding carrier population M, quantum well carrier population N, optical cavity photon population S, and self-heating-induced quantum well temperature T_{QW}.

6.3 Terminals

The terminals of the model represent the electrical nodes from which circuit simulators access model inputs and outputs. The present version of the model (1.0.0) is prototyped as follows:

module vcsel(cathode,anode,refnode,P,L,tsink,tqw)

This includes two electrical nodes for the cathode and anode of the laser diode. To allow compatibility with all standard circuit simulators, the device output power, wavelength, and thermal behavior are recorded as pseudo-electrical nodes rather than relying on proprietary treatments of light and thermal behavior. The following nodes represent non-electrical quantities as electrical nodes, with useful information recorded as a voltage with respect to a reference node (refnode).

Table 6.1: Compact model pseudo-electrical nodes

Node Name	Voltage Quantity	Usage
P	Light Power Out (mW)	Connect to refnode w/ GMIN
L	Light Wavelength (μm)	Connect to refnode w/ GMIN
tsink	Heat sink temperature (K)	Apply voltage source from refnode
tqw	Quantum well temperature (K)	Connect to refnode w/ GMIN

6.4 Parameters

To be both physically justifiable and practically useful, a model must only use parameters that can be calculated from materials or structural properties or extracted from standard device testing experiments. The default parameters provided with the model describe a generic 850 nm DBR VCSEL, providing a starting point for parameter extraction for this most numerous category of VCSEL lasers. Showing the extensibility of the model, parameter sets have also been developed for 1550 nm HCG VCSELs using proprietary data that cannot be shared in this dissertation.

Table 6.2: Compact model electrical parameters

Name	Default	Units	Description
is	1e-15	A	Saturation current
rp	90	Ohm	pad resistance
cp	50e-15	F	pad capacitance
cjt	500e-15	F	Junction capacitance
rdbr1	30	Ohm	DBR resistance
rdbr2	30	Ohm	DBR resistance
ideality	2	#	Ideality factor of diode

Table 6.3: Compact model geometrical parameters known a priori from device design

Name	**Default**	**Units**	**Description**
rapt	4.5e-4	cm	radius of aperture
dqw	8e-7	cm	thickness of quantum wells
nqw	3	#	number of quantum wells
Gammaq	0.1	#	Ratio of quantum well volume to SCH volume.

Table 6.4: Compact model optical parameters

Name	Default	Units	Description
Gamma	0.025	#	Mode overlap factor from quantum well; fit or use optical simulations to calculate
Beta	1.69e-4	s	spontaneous emission coefficient
vg	9E9	cm/s	Mode group velocity
alphai0	12	cm^-1	Internal modal loss
alphatm	18	cm^-1	Top mirror modal loss
alphabm	1.6	cm^-1	Bottom mirror modal loss
etai0	0.849	#	injection efficiency at 0C (273.15 K)
Epsicm	3.8E-17	#	Photon dependence of gain compression (see Kern)
amfracK	1e-3	K^-1	Mirror reflectivity changes with temp (see Westbergh)

EpsicmK	1e-18	cm^3/K	Gain compression change with temp

Table 6.5: Compact model carrier dynamics parameters

Name	Default	Units	Description
tcap	1e-12	s	capture time to quantum well from clad
tesc	60e-12	s	escape time from quantum well to clad

Table 6.6: Gain model parameters (vs. quantum well carrier concentration):

Name	Default	Units	Description
Ntrlog	1.5e18	cm^{-3}	transparency density
Nslog	2e17	cm^{-3}	Wuantum well gain parameter
gnperK	-3.4e-3	1/K	Gain rolloff vs temperature
gain0	4000	cm^{-1}	gain at Tgainfit
Tgainfit	300	K	temperature of unperturbed gain model

Table 6.7: Compact model thermo-optical parameters

Name	Default	Units	Description
dlcavdt	0.062	nm/K	cavity wavelength change vs tempreature
dlgdt	0.3	nm/K	gain peak change vs temperature
lambda0	0.850	um	wavelength at Tfit

Arec0	1e8	s^{-1}	NR recombination coefficient
Brec0	1.5e-10	s^{-1} cm^{-3}	Radiative recombination coefficient
Crec0	4e-30	$s^{-1}cm^{-6}$	SRH recombination coefficient
TrefK	300	K	Temp at which thermally-dependent parameters are measured
Rtherm0	1.9e3	K/W	Thermal resistance to heat sink
Ttherm	1e-6	sec	Thermal time constant

Table 6.8: Compact model thermal dependence parameters:

alphaiK	0.035	cm^{-1} K^{-1}	Temperature change of alphai
etaiK1	0.0022	K^{-1}	Quantum well capture vs. temperature 1st deriv
etaiK2	-3.3e-5	K^{-2}	Quantum well capture vs. temperature 1st deriv
RthermK	0	W^{-1}	Change in Rtherm vs temp = 5
BrecK1	-7.5e-13	1/s*cm^3/K	thermal fit of Brec
BrecK2	3.125e-15	1/s*cm^3/K^2	thermal fit of Brec

Scaling parameters are necessary to make the currents and voltages of pseudoelectrical nodes reasonable magnitudes. This improves convergence, but does not change model equations.

Table 6.9: Compact model scaling parameters

No	1e18	#	scaling for N
Mo	1e16	#	scaling for M
Po	1e15	#	scaling for P
delta	5e-8	#	offset for transformation P = $(Y+delta)^2$

6.5 Equations

In order to successfully perform simulations in circuit simulators, a compact model's equations must abide by strict requirements. Since the equations will be subjected to Newton-Raphson-like methods for DC analysis, models must guarantee that the functions are defined and differentiable throughout all possible values of model equations (including nonphysical values), and that only one solution uniquely exists. This is notably not the case for the traditional rate equations, which have long been observed to produce spurious solutions[51]. For this reason, we apply transformations to the rate equations as described below.

The core of the model is three equations describing the time-domain dynamics of electrons in the separate confinement heterostructure, electrons in the quantum well, and photons in the optical cavity, represented by variables M, N, and S. Rate terms describe different mechanisms of transfer between these populations, eventually leading to light power out (Pout). These rate equations rest upon several material and structural parameters, many of which depend on internal operating temperature, or on internal populations (M, N, and S). The model begins by calculating those condition-dependent parameters.

One of the main accomplishments of the model is the physical treatment of self-heating in VCSELs. Many past modeling efforts treat self-heating phenomenologically as a temperature-dependent threshold current offset. While this approach can accurately reproduce DC rolloff behavior, it requires device-by-device extraction and fails to model the time-dependent aspect of self-heating. Based on theoretical studies of self-heating in the literature, we chose several model parameters to be on thermally dependent on the quantum well temperature, TempQW[52]. These fittings use Tfit = TempQW - TrefK, while one uses the temperature in Celsius, Tc. These include the absorption, quantum well capture coefficient, thermal resistance, recombination, total modal light loss out the mirrors, and gain compression factor per photon concentration. The physical effects described by these parameters are the temperature-dependence of internal optical absorption, thermal escape of carriers from the quantum well into the SCH,

The volume of the active region is calculated as a cylinder:

$$volcm = \pi * rapt^2 * dqw * nqw \tag{6.1}$$

$$alphai = alphai0 \; + \; alphaiK * Tfit \tag{6.2}$$

$$etai = etai0 \; + \; etaiK1 * Tc \; + \; etaiK2 * Tc^2 \tag{6.3}$$

$$Rtherm = Rtherm0 \; + \; RthermK * Tfit \tag{6.4}$$

$$Brec \; = \; Brec0 + BrecK1 * Tfit \; + \; BrecK2 * Tfit^2 \tag{6.5}$$

$$alpham = (alphatm + alphabm) * (1.0 + amfracK * Tfit) \quad 6.6$$

$$EpsicmF = Epsicm + EpsicmK * Tfit \quad 6.7$$

The photon lifetime is calculated from the mirror loss:

$$tp = \frac{1}{vg * (alphai + alpham)} \quad 6.8$$

and the quantum well carrier lifetime from the three recombination processes: nonradiative, radiative, and Auger:

$$tn = \frac{1}{Arec0 + Brec * N + Crec0 * N^2} \quad 6.9$$

The fraction of recombination that is radiative, frec, can be calculated from the above equation, but for reasons of convergence must not be allowed to become negative. For this reason, a small value is added.

$$frec = Brec * N * tn + 0.0001 \quad 6.10$$

The wavelength is calculated from linear thermal tuning:

$$lambdaum = lambda0 + lambdaK * Tfit \quad 6.11$$

The output coupling factor theta, defined as S/theta = Pout, is the rate of mirror loss through the top mirror divided by the photon energy, such that 1/theta gives the power output per photon concentration in the cavity.

$$theta = \frac{lambdaum * 1e-6 * Gamma}{h * c * Volcm * vg * alphatm} \quad 6.12$$

The photon concentration S, one of the main variables in the rate equations, is related to the simulation variable Y as:

$$S = theta * (Y + delta)^2 \quad 6.13$$

The above equation represents one of the key steps in avoiding false solutions.

The gain compression factor term:

$$gcf = \frac{1}{1 + EpsicmF * S} \quad 6.14$$

while the complete gain model, with thermal rollover:

$$gain = gain0 * gcf * \frac{ln(N+Nslog)}{Ntrlog + Nslog} + \text{gnperK} * \text{Tfit} \quad (6.15)$$

follows a logarithmic dependence on the carrier concentration N, with a transparency (gain=0) carrier concentration of Ntrlog and a term to avoid overflow, Nslog. The thermal dependence has been added to implement the gain-cavity detuning effects that lead to thermal rollover.

Self-heating is implemented by assuming that any power burned in the device electrically (I*V) that does not exit as light power (Pout) results in heat that must be removed through the thermal resistor, Rth. The heat generated is:

$$heatgen = I_{active} * V_{active} + I_{DBR1} * V_{DBR1} + I_{DBR2} * V_{DBR2} - Pout \quad (6.16)$$

while the resulting DC self-heating temperature is:

$$Tdc = V(tsink) + heatgen * Rtherm * 0.5 * (1.0 + tanh(1e4 * heatgen)) \quad (6.17)$$

with the final factor included to prevent negative heat flow, which leads to model instability.

Finally, the core rate equations describe the populations of carriers in the separate confinement heterostructure surrounding the quantum well (M), the carriers in the quantum well (N), and the photons in the optical cavity (S). In this implementation of the rate equations, the equation describing S is instead replaced through variable transformation to the variable Y, as described above. The first equation, for M,

$$\frac{dM}{dt} = \frac{I_{active} * Gamma1 * etai}{q * Volcm} - \frac{M}{tcap} + \frac{N * Gammaq}{tesc} \quad (6.18)$$

describes electrons entering the SCH and being captured into the quantum well, as well as escaping back from the quantum well. The equation for N,

$$\frac{dN}{dt} = \frac{M}{Gammaq * tcap} - \frac{N}{tn} - \frac{N}{tesc} - gain * vg * S + (e^{N*100000/N_o}) \quad (6.19)$$

describes the electrons entering from the SCH, recombining, escaping to the SCH, or recombining under stimulated emission as laser gain. The final term prevents Newton-Raphson steps from exploring negative N values, which are nonphysical and cause numerical overflow (log of negative). Lastly, the equation for Y,

$$2\frac{dY}{dt} = Gamma * gain * vg * (Y + delta) + \frac{Gamma * Beta * N * frec}{theta * tn * (Y + delta)} - \frac{(Y + delta)}{tp} \quad (6.20)$$

includes terms representing the generation of photons through stimulated emission and spontaneous emission into the mode, and photon absorption and escape. The factor of 2 at

left results from the variable transformation, from an equation originally describing dS/dt.

6.6 Parameter Extraction from Literature Data

Parameter extraction represents a critical phase of compact model use and an important feature separating compact models from ad-hoc models. To apply to the full range of devices available in academia and industry for the desired device category, parameters must be either derived from known material or device design quantities or able to be fitted from a well-defined list of experiments. Once data are captured, parameters are first tested through manual tuning within model-supplied ranges then optimized via Levenberger-Marquadt or other optimization methods. Automated parameter extraction places further requirements on the runtime efficiency, stability, and smoothness of the model, since non-smooth model behavior with respect to parameter values will foil gradient-based methods.

BVCM parameters not immediately available from device design can be extracted from data readily measurable in most optoelectronics labs: DC characteristics (LIV curve), small-signal AC response (electro-optical S_{21}), parasitic response (electrical S_{11}), and lasing wavelength (optical spectra), all taken at a range of ambient temperatures. All experimental data needed a complete parameter extraction were obtained from the recently published characterization of an 850 nm GaAs VCSEL[53]. Fitting the model to DC slope efficiency and rollover gives parameters relating to the optical cavity and quantum well electron capture, as well as the temperature dependence of those parameters. The resonant frequencies and damping factors versus bias current in the RF S_{21} determine optical dynamic parameters such as gain compression factor and photon lifetime. As shown in Figure 6.2, the model provides an excellent fit to the laser power vs. current DC characteristic across a wide temperature range, validating the numerous thermal effects in the model. The DC fit illustrates the importance of thermal roll-over modeling for a directly modulated VCSEL, as this effect limits the peak power available and thus the maximum modulation extinction ratio possible. Furthermore, the DC fit at different temperatures allows use of the model for high-temperature environments such as datacenters.

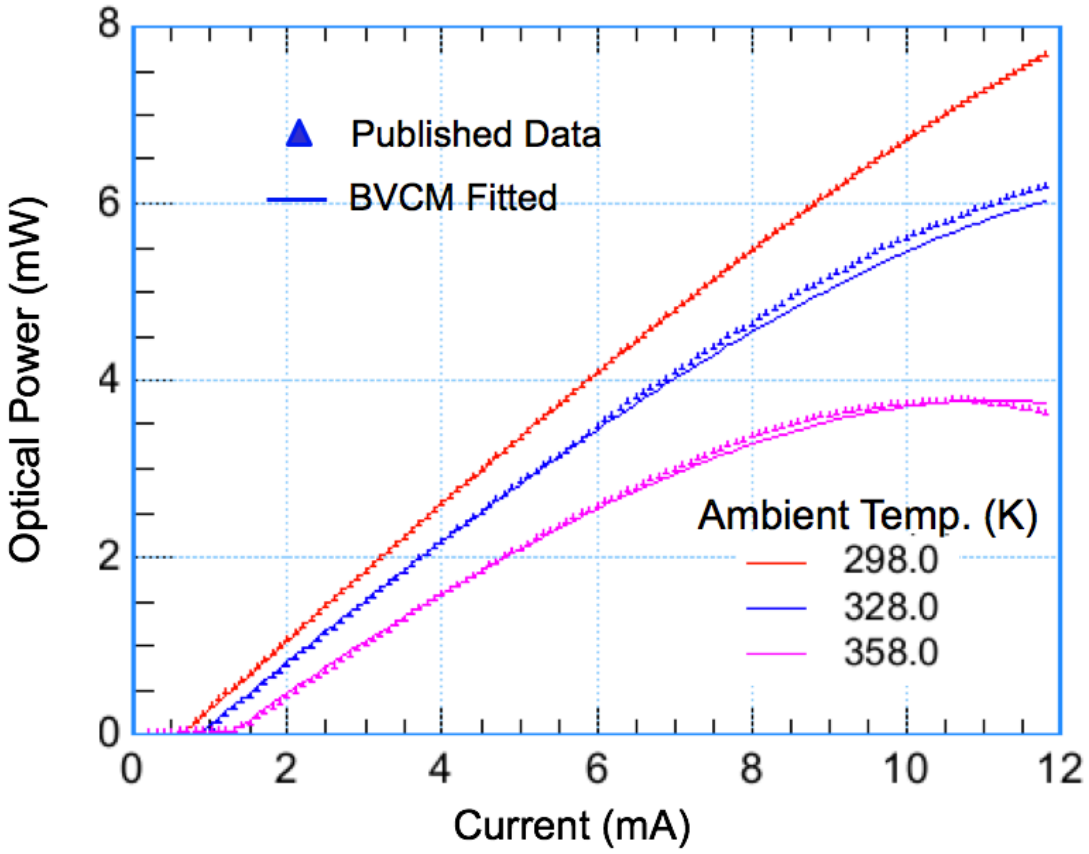

Figure 6.2: Results of parameter extraction using published temperature-dependent power vs. current (LIV) data from Chalmers 850 nm VCSELs. Accuracy in threshold vs. temperature and self-heating rolloff curve shape illustrates success of thermal physics in BVCM, particularly including self-heating.

While the DC LIV provides the best glimpse at the function of model physics and underpins all uses of VCSELs, most applications of cutting-edge VCSELs rely in the high-speed modulation behavior of the device. Many parameters, including capacitances and the gain-compression factor, do not affect model results during DC operation and thus require extraction from RF S-parameter data. Though users without access to high-speed S-parameter measurement capabilities could obtain many of these parameters from device simulations such as FEM, FDTD, or modal analysis, the recommended approach is simultaneous fitting to both LIV, S_{21} vs. current, and S_{11} vs. current. The fitting results in Figure 6.2 were simultaneously fit to S-parameter data published in the same paper, also provided by the authors. In the simultaneous fitting, priority was given to accurate LIV, and DC-irrelevant parameters optimized for fitting to S-parameter data.

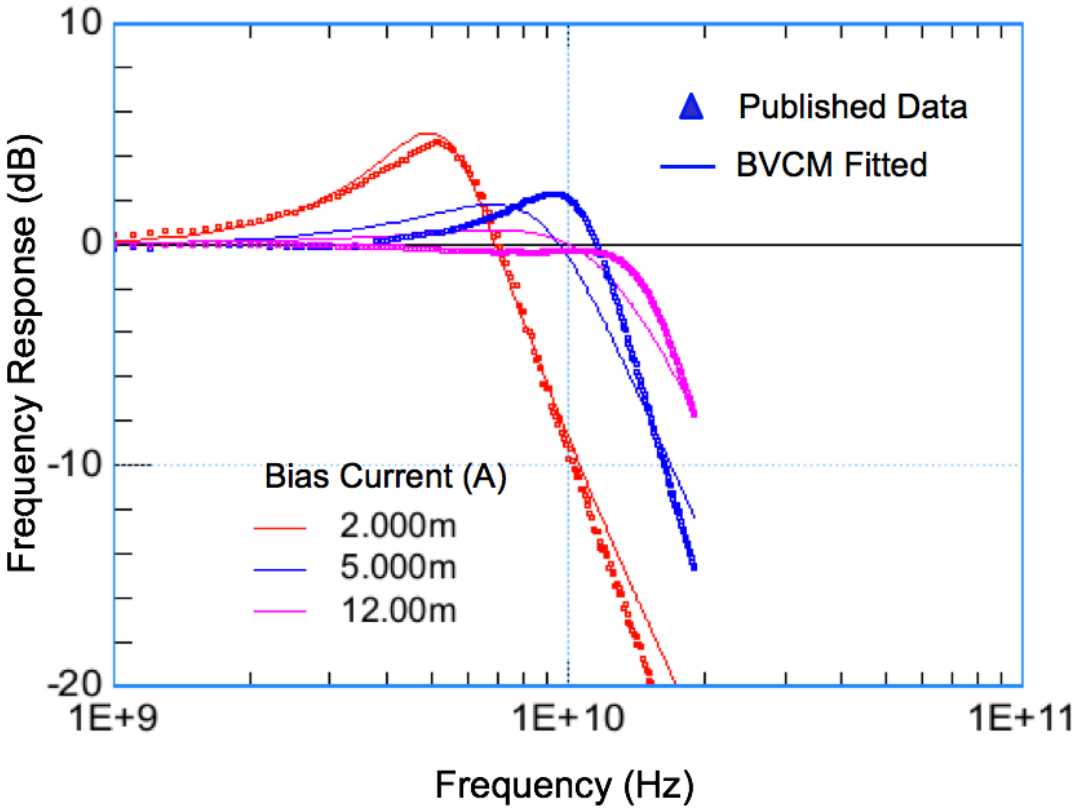

Figure 6.3 S_{21} modulation response at varying DC bias current I_d, results of parameter extraction from literature data performed simultaneously with previous LIV-vs.-temperature figure. Fitting at high I_d confounded by thermal physics not included in the model, as described in the source of the data.

As shown in Figure 6.3, results of BVCM $|S_{21}|$ simulation from parameters extracted simultaneously from 850 nm literature VCSEL data show the model's high-speed effects, including the increase of laser relaxation frequency f_r with I_d due to increasing stimulated emission rates and increased damping γ due to gain compression factor. These relationships are quantified in VCSEL literature and industrial VCSEL specifications as the D-factor and MCEF. The model's difficulty in fitting high-I_d response data results from the observed non-standard relationship of $\gamma(I_d)$ discussed in the source paper, indicating further thermally-dependent effects needed to be added to the model. Such effects are particularly visible in small-aperture edge high-speed single-mode VCSELs such as those described here. Nonetheless, the model as fitted provides sufficient accuracy for the normal range of VCSEL operation to enable system design.

6.7 Example System Design at 25 Gbps using BVCM

Using the model parameters extracted above with no further fitting, we performed transient simulations in HSPICE to analyze VCSEL performance under 25 Gbps directly modulated on-off keying with a PRBS7 data source. As a test of model quality in transient simulations, we drove the VCSEL model with the same conditions as the

original experimental paper: 7 mA DC bias current with 0 dBm modulation at 25°C ambient temperature. The simulated eye diagram in Fig. 3 (a) shows an eye height of 4.8 dB, close to the experimentally measured 4.4 dB[53]. To demonstrate the use of the compact model for system-level design, we implemented a simple one-tap digital pre-emphasis as a separate Verilog-A behavioral model and included this representative driver circuit together in HSPICE transient simulations. At 25 Gbps and 25°C, this simple pre-emphasis increased the eye height 4.8 dB to 5.4 dB, as shown in Fig. 3 (b). This serves as an example of the design of electronic compensation systems for VCSEL dynamics using BVCM.

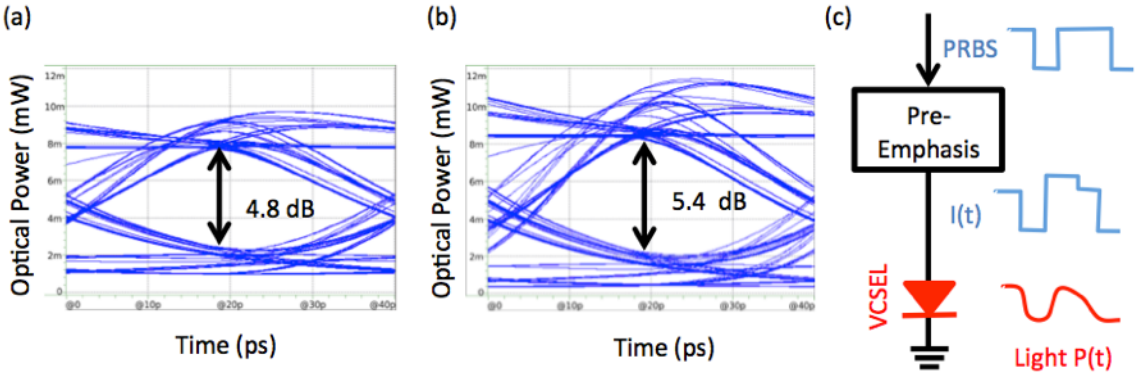

Figure 6.4 (a) Simulated 25 Gbps VCSEL eye diagram without pre-emphasis, eye height = 4.8 dB (b) Simulated 25 Gbps VCSEL eye diagram with digital pre-emphasis implemented in HSPICE, eye height = 5.4 dB (c) Illustration of pre-emphasis block.

6.8 Further work

Though focused initially on high-speed VCSEL modulation, the core rate equations of BVCM are extensible to a broader range of laser designs and behaviors. Particularly relevant to this thesis, mechanical tunability and radiation-pressure forces have been incorporated into unreleased versions of the model, pointing a way towards simulation of induced or self-oscillation optomechanical effects in VCSELs. The damped harmonic oscillator equations of motion lend themselves well to compact modeling, given the widespread use of compact modeling in the MEMS literature. Compact modeling of such optomechanical effects enables both application of circuit simulator tools to understand these phenomena and circuits to enhance or prevent these behaviors. Periodic steady-state methods used to design oscillators, such as shooting and harmonic balance, can provide greater insight into self-oscillation than the simple sinusoidal ansatz used previously to simulate self-oscillation in this thesis. Examples of circuit co-design with optomechanical VCSELs could include feedback mechanisms to stabilize self-oscillation or precise tuning modulation circuits that accommodate for the unwanted chirp effect of radiation pressure.

7 Conclusions

Through experimental characterization of VCSELs, we have demonstrated a new category of behaviors in VCSEL lasers using the forces of radiation pressure inside the

lasing cavity. These phenomena include the ability to drive the mirror mechanically using current modulation via radiation pressure and the tendency of VCSELs in vacuum to mechanically self-oscillate. From the perspective of the field of cavity optomechanics, electrically-pumped lasing cavities provide both a simple, integrated means to implement a cavity optomechanical system and a pathway to separate the ingredients that create optomechanical damping: force gradient and response delay. From the perspective of VCSEL systems, we have developed a means to create large-bandwidth swept light for ranging and imaging applications. And from the perspective of the MEMS community, we have shown an integrated mechanism to actuate mechanical modes only weakly excitable with capacitative actuation.

Suggesting an explanation for a novel effect requires a high bar of experimental evidence and careful consideration of both the proposed mechanism and possible competing effects. In this case, we assemble a complete picture of optomechanical effects in VCSELs through optical characterization of the light produced by self-oscillating VCSELs, direct observation through stroboscopic SEM techniques, and electrical measurements of self-voltage modulation. We characterize the device's mechanical damping using laser Doppler velocimetry (LDV) and use laser rate equation analysis to show that radiation pressure can provide sufficient anti-damping to produce self-oscillation. The only plausible competing explanation, photothermal optomechanical effects, is shown to be unlikely through simulations of optical absorption, thermal expansion, and the thermal time constant in HCG VCSELs. Altogether, these data and simulations confirm the radiation-pressure-based explanation of the new effects observed in this work.

References

[1] H. Soda, K. Iga, C. Kitahara, and Y. Suematsu, "GaInAsP/InP Surface Emitting Injection Lasers," *Jpn. J. Appl. Phys.*, vol. 18, no. 12, pp. 2329–2330, Dec. 1979.

[2] C. J. Chang-Hasnain, "Tunable VCSEL," *IEEE J. Sel. Top. Quantum Electron.*, vol. 6, no. 6, pp. 978–987, 2000.

[3] C. F. R. Mateus, M. C. Y. Huang, Y. Deng, A. R. Neureuther, and C. J. Chang-Hasnain, "Ultrabroadband Mirror Using Low-Index Cladded Subwavelength Grating," *IEEE Photonics Technol. Lett.*, vol. 16, no. 2, pp. 518–520, 2004.

[4] M. C. Y. Huang, Y. Zhou, and C. J. Chang-Hasnain, "A nanoelectromechanical tunable laser," *Nat. Photonics*, vol. 2, no. 3, pp. 180–184, 2008.

[5] Y. Rao, W. Yang, C. Chase, M. C. Y. Huang, D. P. Worland, S. Khaleghi, M. R. Chitgarha, M. Ziyadi, A. E. Willner, and C. J. Chang-hasnain, "Long-Wavelength VCSEL Using High-Contrast Grating," vol. 19, no. 4, 2013.

[6] D. Fattal, J. Li, Z. Peng, M. Fiorentino, and R. G. Beausoleil, "Flat dielectric grating reflectors with focusing abilities," *Nat. Photonics*, vol. 4, no. July, pp. 466–470, 2010.

[7] F. Lu, F. G. Sedgwick, V. Karagodsky, C. Chase, and C. J. Chang-Hasnain, "Planar high-numerical-aperture low-loss focusing reflectors and lenses using subwavelength high contrast gratings.," *Opt. Express*, vol. 18, no. 12, pp. 12606–14, 2010.

[8] L. Zhu, J. Kapraun, J. Ferrara, and C. J. Chang-Hasnain, "Flexible photonic metastructures for tunable coloration," *Optica*, vol. 2, no. 3, pp. 255–258, 2015.

[9] C. J. Chang-Hasnain and W. Yang, "High-contrast gratings for integrated optoelectronics," *Adv. Opt. Photonics*, vol. 4, no. 3, p. 379, Sep. 2012.

[10] J. Kepler, *De cometis libelli tres*. Andrea Apergiri, 1619.

[11] E. F. Nichols and G. F. Hull, "The Application of Radiation Pressure to Cometary Theory," *Astrophys. J.*, vol. 17, p. 352, Jun. 1903.

[12] V. B. Braginsky and A. B. Manukin, "Ponderomotive effects of electromagnetic radiation," *Sov. Phys. JETP*, vol. 25, no. 4, pp. 653–655, 1967.

[13] V. B. Braginsky, A. B. Manukin, and M. Y. Tikhonov, "Investigation of Dissiptive Ponderomotive Effects of Electromagnetic Radiation," *Sov. Phys. JETP*, vol. 31, no. 5, p. 829+, 1970.

[14] J. D. Teufel, T. Donner, D. Li, J. W. Harlow, M. S. Allman, K. Cicak, a J. Sirois, J. D. Whittaker, K. W. Lehnert, and R. W. Simmonds, "Supplementary Sideband cooling of micromechanical motion to the quantum ground state.," *Nature*, vol. 475, no. 7356, pp. 359–363, 2011.

[15] D. F. Pace, A.F., Collett, M.J, and Walls, "Quantum limits in interferometric

detection of gravitational radiation," *Phys. Rev. A*, vol. 47, no. 4, pp. 3173–3189, 1993.

[16] A. Dorsel, J. D. McCullen, P. Meystre, E. Vignes, and H. Walther, "Optical bistability and mirror confinement induced by radiation pressure," *Phys. Rev. Lett.*, vol. 51, no. 17, pp. 1550–1553, 1983.

[17] S. Bose, K. Jacobs, and P. L. Knight, "Scheme to probe the decoherence of a macroscopic object," *Phys. Rev. A*, vol. 59, no. 5, pp. 3204–3210, May 1999.

[18] S. Mancini, D. Vitali, P. Tombesi, U. Camerino, and I.- Camerino, "Optomechanical Cooling of a Macroscopic Oscillator by Homodyne Feedback," *Phys. Rev. Lett.*, vol. 80, no. 4, pp. 688–691, 1998.

[19] D. Kleckner and D. Bouwmeester, "Sub-kelvin optical cooling of a micromechanical resonator," vol. 444, no. November, pp. 75–78, 2006.

[20] T. Carmon, H. Rokhsari, L. Yang, T. J. Kippenberg, and K. J. Vahala, "Temporal Behavior of Radiation-Pressure-Induced Vibrations of an Optical Microcavity Phonon Mode," *Phys. Rev. Lett.*, vol. 94, no. 22, p. 223902, Jun. 2005.

[21] K. E. Grutter, M. Davanco, K. Srinivasan, M. Davanço, J. Chan, A. H. Safavi-naeini, and O. Painter, "Si 3 N 4 nanobeam optomechanical crystals," *IEEE J. Sel. Top. Quantum Electron.*, vol. 21, no. c, pp. 3–4, Jul. 2013.

[22] M. Aspelmeyer, T. J. Kippenberg, and F. Marquardt, "Cavity optomechanics," *Rev. Mod. Phys.*, vol. 86, no. 4, pp. 1391–1452, 2014.

[23] U. Kemiktarak, M. Metcalfe, M. Durand, J. Lawall, U. Kemiktarak, M. Metcalfe, M. Durand, and J. Lawall, "Mechanically compliant grating reflectors for optomechanics," *Appl. Phys. Lett.*, vol. 100, no. 2012, p. 61124, 2012.

[24] U. Kemiktarak, M. Durand, M. Metcalfe, and J. Lawall, "Cavity optomechanics with sub-wavelength grating mirrors," *New J. Phys.*, 2012.

[25] R. S. Tucker, D. M. Baney, W. V Sorin, and C. A. Flory, "Thermal Noise and Radiation Pressure in MEMS Fabry – Pérot Tunable Filters and Lasers," *IEEE J. Sel. Top. Quantum Electron.*, vol. 8, no. 1, pp. 88–97, 2002.

[26] H. Halbritter, C. Sydlo, K. Benjamin, F. Riemenschneider, H. L. Hartnagel, L. Fellow, and P. Meissner, "Impact of Micromechanics on the Linewidth and Chirp Performance of MEMS-VCSELs," *IEEE J. Sel. Top. Quantum Electron.*, vol. 13, no. 2, pp. 367–373, 2007.

[27] A. Hangauer, J. Chen, R. Strzoda, and M.-C. Amann, "The Frequency Modulation Response of Vertical-Cavity Surface-Emitting Lasers: Experiment and Theory," *IEEE J. Sel. Top. Quantum Electron.*, vol. 17, no. 6, pp. 1584–1593, 2011.

[28] M. G. Moharam, E. B. Grann, and D. A. Pommet, "Formulation for stable and efficient implementation of the rigorous coupled-wave analysis of binary gratings," vol. 12, no. 5, pp. 1068–1076, 1995.

[29] V. Karagodsky, F. G. Sedgwick, and C. J. Chang-hasnain, “Theoretical analysis of subwavelength high contrast grating reflectors,” vol. 18, no. 16, 2010.

[30] W. Yang, S. A. Gerke, K. W. Ng, Y. Rao, C. Chase, and C. J. Chang-hasnain, “Laser optomechanics,” *Sci. Rep.*, vol. 5, pp. 1–8, Sep. 2015.

[31] L. Coldren, S. W. Corzine, and M. Masanovic, *Diode Lasers and Photonic Integrated Circuits*. John Wiley and Sons, 2012.

[32] C. F. R. Mateus, M. C. Y. Huang, and C. J. Chang-Hasnain, “Micromechanical tunable optical filters: general design rules for wavelengths from near-IR up to 10μm,” *Sensors Actuators A Phys.*, vol. 119, no. 1, pp. 57–62, Mar. 2005.

[33] C. Zener, “Internal Friction in Solids,” *Phys. Rev.*, vol. 230, no. 1937, 1938.

[34] F. Marquardt, J. G. E. Harris, and S. M. Girvin, “Dynamical Multistability Induced by Radiation Pressure in High-Finesse Micromechanical Optical Cavities,” *Phys. Rev. Lett.*, vol. 96, no. 10, p. 103901, Mar. 2006.

[35] S. A. Gerke, W. Yang, K. W. Ng, C. Chase, Y. Rao, and C. Chang-hasnain, “Broadband Self-Swept High Contrast Grating VCSEL,” pp. 2–3, 2015.

[36] P. Qiao, G. Su, Y. Rao, M. C. Wu, C. J. Chang-hasnain, and S. L. Chuang, “Comprehensive model of 1550 nm,” *Opt. Express*, vol. 22, no. 7, pp. 8541–8555, 2014.

[37] O. Arcizet, P.-F. Cohadon, T. Briant, M. Pinard, and a Heidmann, “Radiation-pressure cooling and optomechanical instability of a micromirror.,” *Nature*, vol. 444, no. 7115, pp. 71–4, Nov. 2006.

[38] M. Metcalfe, “Applications of cavity optomechanics,” *Appl. Phys. Rev.*, vol. 1, no. 3, p. 31105, Sep. 2014.

[39] A. G. Krause, M. Winger, T. D. Blasius, Q. Lin, and O. Painter, “A high-resolution microchip optomechanical accelerometer,” *Nat. Photonics*, vol. 6, no. 11, pp. 768–772, Oct. 2012.

[40] M. Hossein-Zadeh and K. J. Vahala, “An Optomechanical Oscillator on a Silicon Chip,” *IEEE J. Sel. Top. Quantum Electron.*, vol. 16, no. 1, pp. 276–287, 2010.

[41] S. Tallur, S. Sridaran, and S. a. Bhave, “A monolithic radiation-pressure driven, low phase noise silicon nitride opto-mechanical oscillator,” *Opt. Express*, vol. 19, no. 24, pp. 24522–24529, 2011.

[42] J. C. A. Hangauer and R. S. M. Amann, “Tunable diode laser spectroscopy with optimum wavelength scanning,” pp. 331–339, 2010.

[43] K. S. Kaur, A. Z. Subramanian, P. Cardile, R. Verplancke, J. Van Kerrebrouck, S. Spiga, R. Meyer, J. Bauwelinck, R. Baets, and G. Van Steenberge, “Flip-chip assembly of VCSELs to silicon grating couplers via laser fabricated SU8 prisms,” *Opt. Express*, vol. 23, no. 22, p. 28264, 2015.

[44] V. Jayaraman, G. D. Cole, M. Robertson, a. Uddin, and a. Cable, “High-sweep-

rate 1310 nm MEMS-VCSEL with 150 nm continuous tuning range," *Electron. Lett.*, vol. 48, no. 14, p. 867, 2012.

[45] J. Ferrara, W. Yang, L. Zhu, P. Qiao, and C. J. Chang-Hasnain, "Heterogeneously integrated long-wavelength VCSEL using silicon high contrast grating on an SOI substrate," *Opt. Express*, vol. 23, no. 3, pp. 27–29, 2015.

[46] D. M. Kuchta, C. L. Schow, A. V Rylyakov, J. E. Proesel, F. E. Doany, and C. Baks, "A 56.1Gb/s NRZ Modulated 850nm VCSEL-Based Optical Link," in *OFC/NFOEC Technical Digest*, 2013, pp. 56–58.

[47] F. Karinou, C. Prodaniuc, N. Stojanovic, M. Ortsiefer, A. Daly, R. Hohenleitner, B. Koegel, and C. Neumeyr, "Directly PAM-4 Modulated 1530-nm VCSEL Enabling 56 Gb/s Data-Center Interconnects," *IEEE Photonics Technol. Lett.*, vol. 1135, no. c, pp. 1–1, 2015.

[48] A. M. Kern, *CMOS Circuits for VCSEL-Based Optical IO*. Dissertation, Massachusetts Institute of Technology, 2007.

[49] S. A. Gerke and C. Chang-Hasnain, "Berkeley VCSEL Compact Model." .

[50] E. Hugues-Salas, X. Q. Jin, R. P. Giddings, Y. Hong, S. Mansoor, A. Villafranca, and J. M. Tang, "Directly modulated VCSEL-based real-time 11.25-Gb/s optical OFDM transmission over 2000-m legacy MMFs," *IEEE Photonics J.*, vol. 4, no. 1, pp. 143–154, 2012.

[51] S. A. Javro and S. M. Kang, "Transforming Tucker's linearization laser rate equations to a form that has a single solution regime," *J. Light. Technol.*, vol. 13, no. 9, pp. 1899–1904, 1995.

[52] P. P. Baveja, B. Kögel, P. Westbergh, J. S. Gustavsson, Å. Haglund, D. N. Maywar, G. P. Agrawal, and A. Larsson, "Assessment of VCSEL thermal rollover mechanisms from measurements and empirical modeling.," *Opt. Express*, vol. 19, no. 16, pp. 15490–505, Aug. 2011.

[53] P. Westbergh, R. Safaisini, E. Haglund, J. S. Gustavsson, A. Larsson, M. Geen, R. Lawrence, and A. Joel, "High-Speed Oxide Confined 850-nm VCSELs Operating Error-Free at 40 Gb / s up to 85 ° C," *IEEE Photonics Technol. Lett.*, vol. 25, no. 8, pp. 768–771, 2013.